A Spectral Element Formulation for Fluid-Structure Interactions: Application to Flow Through Collapsible Channels

by

James Jang-Sik Shin

Bachelor of Science in Aerospace Engineering
(University of Southern California, 1990)

Masters of Science in Aeronautics and Astronautics
(Massachusetts Institute of Technology, 1992)

Submitted to the Department of Mechanical Engineering
in partial fulfillment of the requirements for the degree of

Doctor of Philosophy in Mechanical Engineering

at the

MASSACHUSETTS INSTITUTE OF TECHNOLOGY

September 1996

Author..... .....
/ / / Department of Mechanical Engineering
June 1996

Certified by..... .....
Roger D. Kamm, Professor
Thesis Supervisor

Accepted by.. .....
Ain A. Sonin
Chairman, Departmental Committee on Graduate Studies

A Spectral Element Formulation for Fluid-Structure Interactions: Application to Flow Through Collapsible Channels

by

James Jang-Sik Shin

Submitted to the Department of Mechanical Engineering in September 1996
in partial fulfillment of the requirements for the degree of

Doctor of Philosophy in Mechanical Engineering

Abstract

Vessels in the body are elastic and collapse when the transmural pressure becomes sufficiently negative. Once collapse and subsequent flow limitation occur, these vessels often exhibit self-excited, flow-induced oscillations, commonly referred to as flutter. The exact mechanism behind this phenomenon is not well understood.

Solid mechanics capability was added to the computational fluid dynamics package NEKTON, making possible simulation of general fluid-structure interactions. Continuum spectral elements were used for the solid; the capability of Arbitrary-Eulerian-Lagrangian (ALE) Formulation in NEKTON was used to track both fluid and solid elements. Using the segregated approach to couple the two domains, the completed code was able to simulate two-dimensional fluid-structure interactions by solving the full Navier-Stokes equation coupled with full structural equations for the solid wall with geometric nonlinearities taken into account. This is a significant improvement over other models which rely on several simplifying assumptions concerning the fluid dynamics (e.g., one-dimensional flow or lubrication theory) and/or the structural mechanics (e.g., tube law, membrane or thin plate theory), leaving uncertainty as to the realism of their predictions.

The results are presented for both steady and unsteady flow in a two-dimensional channel with a compliant segment on one wall, similar to the geometry recently used by Pedley and colleagues. The results reproduce the membrane solutions of Luo and Pedley. The flow limitation simulations suggest that wave speed limitation can be established for both tension-dominant and bending-dominant regimes. The dispersion relations predict the limiting flow rate well when the wavelength is taken to be the length of the collapsible

segment. The unsteady results suggest that this segregated approach, in which the solution is alternately obtained for the fluid and solid, may not be capable of simulating unsteady flows in which the boundary motions arise from interactions with the fluid. The approach works well, however, for situations in which the fluid is responding to motion of the boundary. For the case of flow-induced wall motions, it may be necessary to resort to solution of the fully-coupled equations. There appear to be no such constraint, however, on the solution of steady flows.

Thesis Committee:

Prof. Roger D. Kamm, Chairman
Prof. David M. Parks
Dr. Lee W. Ho

Acknowledgments

Looking back at the last six years of my life at MIT, I have learned a lot about "life". I managed to pick up two degrees, one son, and the game of golf, so I guess it was a productive period. It's time for me to move on and face the new challenges that lie ahead. Before doing so, I want to thank the people who influenced me in many ways.

Let me start with my wife, who was beside me from the beginning. We were very naive back then but we grew together over the years. Her sacrifice, love, and understanding have sustained me thus far. I look forward to making her happy when I start to make some serious money.

Academically, Professor Roger Kamm, who guided me for a full six years, deserves my utmost gratitude. He was always supportive and his guidance made my life less painful. I thank him for not making my life a living hell. Dr. Lee Ho of Nektonics deserves a lot of credit of making this thesis possible. He guided me through the coding stage and often helped me with the debugging process. His knowledge of CFD and FEM was simply amazing. I would also like to thank Professor Parks for the "real" solid mechanics perspective of my work.

Socially, my colleagues at FML deserves lots of credit for who I am. Too many people touched my life so instead of listing them one by one, I just want to acknowledge that I have many memories here. I hope I have influenced them in a positive way. The title of "Godfather" was always flattering and I would never forget "Eddies 95". I would also like to mention my KGSA brothers. I am confident that they will all go far in life.

Lastly, I want to thank my family members and friends who believed in me. It wasn't easy but guess what? I made it!

Contents

List of Figures

List of Tables

Chapter 1

Introduction

Virtually all of the vessels in the body are elastic and collapse when the transmural (internal minus external) pressure becomes sufficiently negative. Figure 1.1 shows the behavior of flow rate in a typical collapsible tube setting. With the upstream transmural pressure fixed, the reduction in the downstream pressure produces the initial increase in the flow rate. During this process, the tube continues to collapse into an elliptic shape. As the downstream pressure continues to decrease, there exists a critical pressure at which the flow rate ceases to increase. This phenomenon is referred to as flow limitation. Once flow limitation occurs, these vessels often exhibit self-excited, flow-induced oscillations (referred to as flutter) which are manifested as audible sounds, medically referred to as Korotkoff sounds in blood flow or wheezing in the lungs [49, 63]. Physiologically, examples of these phenomena include blood flow in arteries and veins, air flow in the lungs during a forced expiration and coughing, and uretheral flow dynamics [28, 49, 70].

This phenomenon has been realized in many different experimental settings. A typical laboratory experimental setup is referred to as Starling Resistor and shown in Figure 1.2. The collapsible tubing is surrounded by a sealed chamber in which the external pressure can be independently adjusted. Incompressible fluid flows along the tube from a constant-head reservoir, and the flow rate can be controlled by adjusting the resistances of the rigid parts of the system upstream and downstream of the collapsible segment. Bertram

[8, 9, 10, 11, 12] , in particular, has revealed many different types of oscillations (both periodic and chaotic) and has demonstrated that the oscillations are characteristic of a highly nonlinear system of great complexity. Many experiments are performed with variety of parameter settings to mimic the actual physiological situations. The general observation is that there are at least two types of oscillation. One is of a relatively large amplitude with low frequency (milking) and is dependent on external conditions (both upstream and downstream of the collapsed region). The choke point (the narrowest portion of the tube) tends to move upstream, opens, and then reforms downstream of the tube. The other, flutter, is localized (choke point does not move upstream) and generally of a much higher frequency. Gavriely et al. [30] observed that flutter only occurred in the presence of flow limitation. This observation suggests that two phenomena are intrinsically related and better examinations are required to understand the physics behind these phenomena.

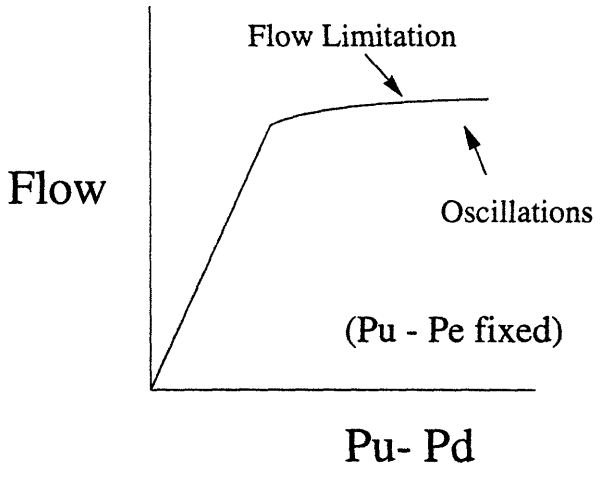

Figure 1.1 The behavior of a collapsible tube when downstream pressure is continuously decreased while flow and pressure drop are monitored. Both flow limitation and oscillations are witnessed.

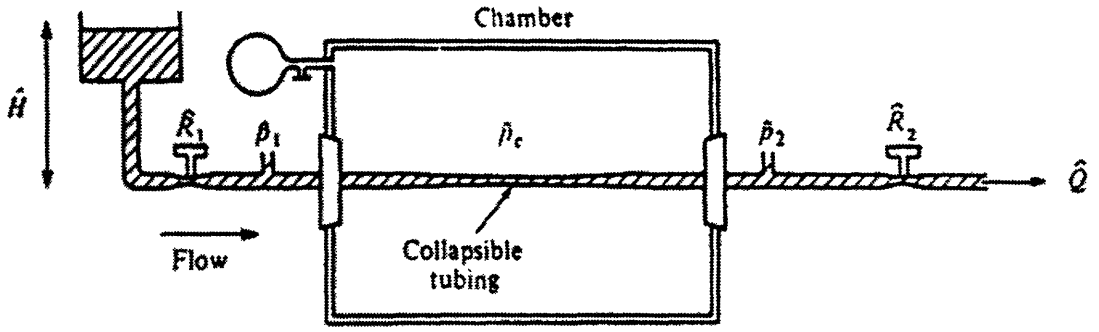

Figure 1.2 Experimental arrangement for studying flow through a collapsible tube (from Pedley [63]). This setup is often referred to as a Starling Resistor.

1.1 Theoretical Models

Numerous theoretical models have been developed to better understand both flow limitation and the flutter mechanism, but no model is free of approximations. Many earlier theoretical models can be categorized as either lumped-parameter or one-dimensional models. In lumped-parameter models [9, 21, 47], the parameters of interest are represented by simple time-dependent variables. These models are composed of nonlinear ordinary differential equations which can be easily integrated, but they are severely limited due to their simplicity. Many real effects are missing, including the inability to incorporate wave propagation, and the flutter phenomenon cannot be modeled. Nevertheless they contributed to the basic understanding of the intrinsic coupling between the behavior of the collapsible segment and the conditions elsewhere in the system, especially during unsteady flow [15, 49].

In contrast, the contribution from one-dimensional models has been more significant. In these models, the flow variables (the fluid pressure, the cross-sectional area, and the cross-sectionally averaged velocity) are taken to be functions of time and

longitudinal distance. The flow variables are determined through equations of continuity, momentum, and the tube law. The last equation relates the transmural pressure to the local cross-sectional area, neglecting the effects of wall mass, axial bending stiffness, membrane tension, and viscoelasticity. The most notable work was done by Shapiro [48, 70] , who was able to characterize collapsible flow phenomena for both steady and unsteady cases. He and others [14, 22, 23, 24, 25, 60, 71, 72] have contributed to the understanding of flow limitation, which occurs when the flow reaches the speed of propagation of small-amplitude pressure waves. The wave speed is given by:

$$c^2 = \frac{A_c}{\rho_f}\frac{d(p - p_e)}{dA} \tag{1.1}$$

where A_c is the cross-sectional area of the tube, and ρ_f signifies the fluid density, and the derivative is the slope of the tube law relationship. When the local wave speed (c) reaches the flow velocity (U), waves can no longer propagate upstream to further accelerate the flow, and therefore upstream flow condition cannot be altered. Thus flow is "choked" when S = U/c = 1. This criterion is analogous to the Mach number in compressible flow or the Froude number in open channel flow approaching unity. This explanation is the foundation of "traditional" theory for flow limitation.

These preliminary works also demonstrated the possibility of supercritical flows and spontaneous deceleration to a subcritical speed some distance downstream [43, 50, 59]. This transition is termed the "elastic jump", which is analogous to a shock wave in gas dynamics or a hydraulic jump in free surface flows.

Despite contributions to the understanding of flow limitation, these one-dimensional models with simplified wall mechanics cannot simulate subsequent oscillations realistically. Most notable among the deficiencies of these models are: the assumption of one-dimensional flow which fails to account for such phenomena as flow separation; and

neglect of longitudinal tension, bending stiffness, wall inertia, and viscoelasticity in the equation describing wall motion. The importance of these effects has already been demonstrated by a number of previous studies [30, 34, 35, 37]. Hence it is essential that the theoretical models be multi-dimensional and incorporate realistic wall characteristics even though such models require substantial computational effort.

An effort has been made to overcome the limitations of the above models by incorporating important features of the real system such as viscous energy loss and longitudinal tension in the wall [15, 44, 64]. These studies emphasized understanding of the actual oscillations and they showed that the dynamics of oscillations are dominated by longitudinal movement of the point of flow separation [15]. Specifically, energy loss and pressure recovery downstream of the choke point are required to sustain oscillations. While these models are capable of reproducing the experimental observations qualitatively, they still rely on several simplifying assumptions [15] and contain ad-hoc formulations that are subject to uncertainty [44, 45, 46].

A notable set of theoretical works was developed by Grotberg et al. [32, 33, 34, 35, 36, 37] who combined 2-D fluid flow with the one-dimensional Von Karman plate theory for the solid [52]. Their analysis was limited initially to small amplitude (small perturbation from the undeformed state) wall deflection since linear stability analysis was performed, but their works contributed to the understanding of flutter by identifying the key parameters (ratio of fluid to wall damping, mass ratio, and ratio of bending stiffness to elastance) associated with the critical flutter speed. Their initial work is characterized by potential flow theory, but they later used Darcy's law to represent the resistance of the fluid. One of the key findings was that flow limitation can occur without flow being choked ($S = 0.3$ instead of $S = 1$). This is shown experimentally by Gavriely et al. [29, 30] and later predicted theoretically by Grotberg and Reiss [33, 34]. This raises the key question of whether the steady wave limitation theory is appropriate in predicting flow

limitation when unsteadiness and wall inertia are involved. Equation 1.1 is based on the tube law and therefore wall density is completely ignored. The tube law may be inadequate to account for the actual elastic wave speed in the highly unsteady flow situation. Another key finding by Grotberg and Reiss [34] is that fluid viscous damping is required to predict flutter. Otherwise, only static divergence instability (continuous decrease of the cross-sectional area), similar to theoretical analysis of Weaver & Paidoussis [74] and Matsuzaki et al. [57, 58], is predicted. This finding settled the ongoing contradiction between the theoretical prediction (which takes into account of solid damping only) and the experimental observation in which flutter was witnessed.

More recently, Grotberg and Shee [35] showed that having Darcy friction is equivalent to solving the Orr-Sommerfeld system and the same conclusion about fluid damping requirement was reached. Currently, there is no complete theoretical study involving the full Orr-Sommerfeld system pertaining to the flow in flexible channels. More careful analysis, similar to studies in panel flutter aeroelasticity [7, 18, 19, 20, 51, 54], is required for better understanding of the complex coupling behavior of the two domains.

1.2 Recent Developments

In recent years, the trend has been to abandon the use of tube law and model the compliant wall as a thin elastic membrane [53, 55, 56, 67, 73]. Pedley [64] examined low Reynolds number flow using lubrication theory. However, as the longitudinal tension in the wall became small, the slope at the downstream end became ever steeper, resulting in an inconsistency in the approximation used. This is the same limitation of Heil [38, 39] , who also examined steady lubrication theory with three-dimensional shell equations for the solid. Using the full Navier-Stokes solver for the fluid, Luo and Pedley [55, 56] solved for steady and unsteady cases but kept the wall as an elastic membrane. Since the bending

stiffness plays an important role during large deformation, more exact models of the compliant boundary (preferably a two-dimensional beam or in three dimensions as a shell) would give more insight into flutter phenomena.

In summary, full understanding of flow through a collapsible tube is not available despite the existence of many different theoretical models. The understanding of flow limitation based on the steady wave speed theory may not be adequate. Flow-induced flutter involves a complex interaction between the fluid and solid, and a coupling of the two domains is essential to the understanding of the phenomena. The need for a better model, which can simulate the coupling effect in the absence of these assumptions and simplifications is clearly evident.

1.3 Overview of Fluid-Structure Interactions

Problems involving fluid-structure interactions occur in a wide variety of engineering problems and therefore have attracted the interest of many investigators from different engineering disciplines. As a result, much effort has gone into the development of general computational methods for fluid-structure systems. It is important to realize that our computational approach is yet another attempt to understand this complex coupled system.

The fluid-structure interaction involves two physically different domains in relative motion and can be broadly classified into three Categories as shown in Figure 1.3. Category (A) includes problems with large relative motion such as in flutter of aircraft wings or oscillations of a suspension bridge. Compressibility effects are usually not important in these situations. Category (B) includes problems with limited flow displacement for short duration. The examples are explosion or impact; compressibility plays an important role. Category (C) includes problems with limited flow displacement

but of long duration. Here, such phenomenon as periodic response of offshore structures to waves, acoustic vibrations or ship motions are considered [61, 76].

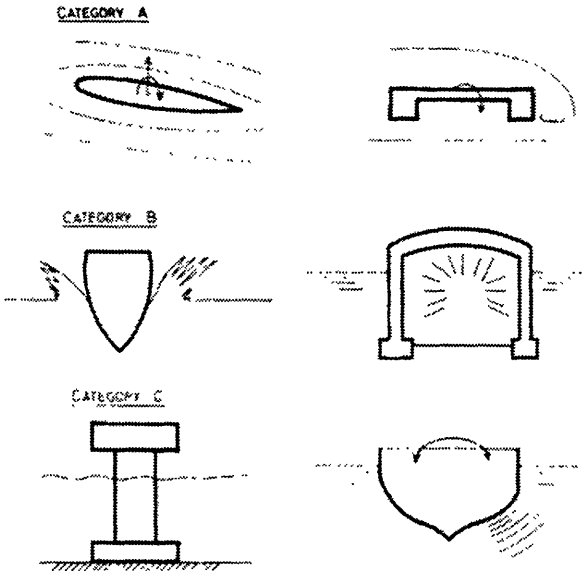

Figure 1.3 Three category classifications for problems in fluid-structure interactions (from Zienkiewicz and Bettess [76]).

The key distinction in above classifications is the fluid behavior. Traditional computational methods have concentrated (with great success) on Categories (B) and (C) in which fluid motion remains small while substantial interaction occurs. These are easier to deal with since considerable simplifications are possible in analyzing the fluid motion. In this limit, velocities are small enough for the convective term to be omitted. Hence fluid can be treated as an elastic solid with a negligible shear modulus. Some investigators introduced the pressure as primary unknowns (field variables) in the fluid and displacements in the solid [4, 6]. There are other variations as primary fluid unknowns (such as fluid potential, hydrostatic pressure etc.) exist in the literature and the results are

quite satisfactory in the simulations involving these categories. (see Olson [61] for more detail).

Only recently have Category (A) cases been pursued extensively. Some of the models are already explained in the previous section. In all cases, there are self-imposed limitations (an either the fluid and/or solid modeling) to ensure feasibility in computational analysis. To the best of our knowledge, there is no computational code robust enough to handle general situations in Category (A). The current model attempts to remove many of the assumptions of other models. The scope is limited to flow through a collapsible channel for now since this problem provided the motivation for our current research. Due to the generality of our approach, however, this model is also capable of simulating many other types of fluid-structure interaction problems included in Categories (A), (B), and (C).

1.4 Problem Statement

The main objective of this thesis is to develop a computational approach to simulate flows through compliant structures. This will be accomplished by developing the numerical tools necessary for analyzing the two-dimensional fluid-structure interactions between a viscous fluid and a solid elastic wall. Once these are completed, emphasis shifts to understanding flow limitation and the mechanism of flutter using a new model which eliminates many assumptions and simplifications of previous models. As a consequence, the most accurate model, compared to other currently existing models, will be operational. Validation of this computational code is accomplished through the analysis of simple two-dimensional flows past compliant boundaries for which analytical or numerical results currently exist in the literature [3, 55, 56]. Once the validation is completed, the conditions which give rise to flow limitation in a two-dimensional channel with a collapsible segment are then sought. This allows one to examine the wave speed flow limitation hypothesis (see section 4.1) in

both tension-dominant and bending-dominant regimes. While it would be desirable to perform simulations in three-dimensions, due to the severe computational requirements, this is an unrealistic goal at present, and we limit the present simulations to the case of a two-dimensional channel with a collapsible segment, similar to Luo and Pedley [55, 56].

The ultimate goal of this work is to better understand the behavior of flow-induced oscillations in collapsible tubes by identifying the physical mechanisms responsible for flutter and the conditions under which it occurs. The more immediate objective is to develop a time-dependent solver for simulating transient fluid-structure interactions. This thesis develops one such approach in which the fluid and solid domains are computed iteratively. While the applicability of this approach to the simulation of flutter is found to be somewhat limited, the method is adequate for a variety of other fluid-structure interaction problems. For example, a wide variety of biological systems which undergo large wall deformations are ideal candidates for solution using the methods proposed here. The success and limitation are described in detail.

Chapter 2

Analysis

The fluid dynamic simulation used, NEKTON, is an advanced computational fluid dynamics package based on the spectral element method. In its current form, NEKTON lacks the capability of incorporating the mechanisms associated with elastic boundaries and therefore cannot address questions concerning fluid-structure interactions. The numerical code will be modified by the addition of a solid solver to match the fluid elements in the current code. This process occurred in steps to make coding manageable, beginning with the case of linear geometry and linearly elastic material, then proceeding to eliminate several of these assumptions one at a time. In this chapter, the steps involved in this enhancement are described in detail.

2.1 Numerical Strategy

The first stage involved analyzing the requirements and tools necessary to achieve our goal. In this section, the initial survey of requirements, along with possible alternatives, is discussed.

The first option was to utilize the existing capability of free surface simulation in NEKTON as a crude approximation of the real wall. Free surface analysis turns out to be inadequate since the no-slip boundary condition at the fluid-structure interface cannot be

satisfied. Even with modification of the boundary condition, the result will miss the key behaviors of solid mechanics including bending stiffness and inertia effects.

NEKTON's "moving wall" capability was then examined. NEKTON can handle the active wall motion by a user-specified function of time and space. The motion determines the new boundary for the fluid domain and fluid solutions are obtained in the new configuration accordingly. We are interested in passive wall motion in which the motion either results from or is influenced by the fluid forces acting on the wall. Only by allowing for a real solid wall will the simulation of passive motion be possible. This step requires significant computational effort, but in exchange, it provides total control over the modeling of the wall. Alternatively, the solid wall can be approximated by system in which the key solid characteristics are represented by discrete masses, springs, and dampers. This method has been tried [9, 75], and repeating it would not likely yield any further insights. We desire a more dedicated solver to study the complex phenomenon of fluid-structure interaction.

The wall can also be modeled using a one-dimensional Von Karman plate theory [52] as many of previous researchers have done. If we do so, however, we are faced with the same constraints as others. First, the plate must be thin so that rotary inertia and shear deformations are neglected. Second, the wall is limited to small departure from equilibrium. This ensures constant thickness, and therefore only small deformations compared to the thickness can be considered. These requirements place restrictions on the general wall motions, and therefore we chose to avoid this approach completely.

The idea of linking with, or directly using, the already-existing solid mechanics solvers such as ABAQUS or ADINA was considered. This plan was abandoned since no commercial software is general enough to solve flutter (to best of our knowledge). Furthermore, the lack of access to source codes would inevitably limit the scope and flexibility of simulations. Numerically, the issue of compatibility must be considered when

coupling with NEKTON. This may lead to artificial modes that can be either numerical or physical in origin, and therefore interpretation of the obtained results will be extremely difficult to interpret.

The initial survey suggested that coding a new solid solver that is in accord with NEKTON is a key to accomplishing our goal. Along with this decision, additional issues had to be resolved. Computationally, the solid elements will be defined as continuum elements such that the rotational degree of freedom does not have to be introduced as is the case with structural elements (plate or shell elements). This is a reasonable approximation as long as the wall is thick enough such that numerical difficulties associated with an ill-conditioned stiffness matrix will not be encountered. Though finite elements are adequate to describe solid mechanics and will result in smaller bandwidth of the stiffness matrix, higher-order spectral elements are used for the wall. Since NEKTON will be used for fluid, there would be a boundary mismatch at the interface if finite elements were used for the solid. This would once again lead to artificial waves that are numerical in nature. Due to this compatibility issue, spectral elements that are consistent with existing fluid elements will be used.

The last issue considered was the complexity of the wall. We want to stay as simple as possible, yet complex enough to capture the real physics. To this end, complexity will be added on later. The solid solver was created with sufficient flexibility such that complexity can be added on easily when the need arises.

2.2 Fluid Solver

NEKTON is chosen as the means to solve the fluid domain, and an understanding of the fundamentals behind the spectral element method is required to increase the numerical efficiency. The general properties of NEKTON are summarized here without giving the

complete description; rather only the major differences with the traditional finite element formulation, which is well documented [5, 68, 77, 78], are emphasized. More complete description of NEKTON can be found in Ronquist [69].

2.2.1 Spectral Element Method (SEM)

There are many different computational techniques available to solve incompressible fluid flow. The methods can be generally classified into two distinct groups. The first group is based on discretizing the "strong" form (differential equations); methods such as finite difference method (FDM) and finite volume method (FVM) belongs to this group. These methods have long historical foundation and are still quite popular in aerospace applications, where high speed simulations with discontinuities (shocks) are of great interest [2, 26, 27].

The second group is based on method of weighed residuals. They start with the "weak" form of the differential equations (variational form); finite element methods (FEM) and spectral methods belong to this group. FEM started as a popular method for solid and structural mechanics analysis, but now its geometric flexibility advantages have promoted wide use in low speed fluid mechanics simulations [68]. What distinguishes the spectral method from the FEM is the use of the shape (also referred to as trial or basis) function. In spectral methods, shape functions are infinitely differentiable (such as Chebyshev or Legendre polynomials), and therefore exponential convergence is expected. But this method is very difficult to apply to any complex geometry of engineering interest since domain discretization is not involved [16]. On the other hand, traditional FEMs (linear or quadratic shape functions) are flexible in geometry since the computational domain is discretized first by dividing up to many small elements. In exchange, only the linear or quadratic convergence rate is expected.

There are many variations to the FEM. Deviating from traditional displacement-based FEMs, there are numerous mixed formulations in which the objective is to relax the conditions to be satisfied by the solution variables (i.e. compatibility conditions) and enlarge the number of solution variables (i.e. displacements, strains, and stresses) simultaneously. Hybrid types are also widely used. In these formulations, some field variables are eliminated on the element level prior to the assemblage process to increase computational efficiency. These variational formulations are effective for the special circumstances such as incompressible solid simulations, plates, shells, and fracture type problems (see [5] for more detail).

Spectral element methods are high-order weighed-residual techniques for the solution of partial differential equations. They combine high-order accuracy of p-type spectral techniques while maintaining the geometric flexibility associated with the low order (h-Type) Finite Element Methods [69]. For this reason, the convergence rate is exponential for the smooth solutions (such as incompressible fluid flow) instead of quadratic (or linear), as seen with the h-type finite element methods. In short, the SEM is the natural extension to take advantage of two different, but similar, methods. The SEM has been chosen for the present analysis largely for its rapid convergence rate, but also because the geometries of interest (e.g. a collapsible channel) are sufficiently simple that the large spectral elements are appropriate.

2.2.2 NEKTON Capability

NEKTON is capable of simulating both steady and unsteady incompressible fluid flow and heat transfer. This means the governing equations of interest are:

Mass conservation: $$\nabla \cdot \vec{u} = 0 \qquad (2.1)$$

Momentum: $$\rho\left(\partial_t \vec{u} + (\vec{u}\cdot\nabla)\vec{u}\right) = -\nabla p + \nabla\cdot\left[\mu\left(\nabla\vec{u} + (\nabla\vec{u})^T\right)\right] - \rho\overline{\beta}T\hat{g} + \rho\hat{f} \tag{2.2}$$

Energy: $$\rho c_p\left[\partial_t T + (\vec{u}\cdot\nabla)T\right] = \nabla\cdot(k\nabla T) + q_{vol} \tag{2.3}$$

subject to appropriate initial and boundary conditions. Note that $\vec{u}$ is the velocity vector, ρ is the density, μ is the dynamic viscosity, $\overline{\beta}$ is the effective thermal expansion coefficient, $\hat{g}$ is the unit vector in the direction of the acceleration of gravity, $\hat{f}$ is the body force per unit mass, ρc_p is the volumetric specific heat, k is the thermal conductivity, and q_{vol} is the volumetric heat generation. Depending on the problem of interest, the subsets of above equations are solved.

The computational domain is represented as a set of macro-elements with the solution and geometry being approximated by high-order tensor-product polynomial expansions (5th through 15th order) within each macro-element. Within each element, a local Cartesian mesh is constructed corresponding to N by N tensor-product Gauss-Lobatto-Legendre collocation points. They are clustered near boundaries for accuracy, interpolation, and quadrature properties. Since the mesh points are unevenly spaced, all the quantities based on area (volume) must be calculated with care. This means weighting must be done when calculating quantities such as spatial norms. Once the collocation points are determined, Lagrangian interpolants are used to approximate dependent variables within each elements. The favorable properties of interpolant functions and the description of solution methods can be found in Ronquist [69].

This technique is very similar to p-type and h-p-type finite element methods used in solid mechanics. This means that variational projection operators and Gauss numerical quadrature are used to generate the discrete equations, which are efficiently solved by iterative procedures based on tensor-product sum-factorization techniques. Previous

studies have shown that SEMs are capable of accurate and efficient solution of a wide range of fluid flow and heat transfer problems [69].

2.2.3 Tensor-Product Form

The key difference with the traditional FEM is that NEKTON uses the tensor-product form of the interpolation function. This form reduces NEKTON's memory requirement; without it, the high-order interpolations functions are too costly due to the greater coupling with neighboring collocation points An example is shown here for illustrative purposes.

In two-dimensional analysis, the regular interpolation functions used in FEM are such that dependent variables (Φ) are expressed by:

$$\Phi(r,s) = h_{pq}(r,s)\Phi_{pq} \tag{2.4}$$

where (r, s) signifies the natural coordinate system and (p, q) represents the collocation points. When the derivative is required,

$$\begin{aligned} \frac{\partial \Phi}{\partial r}(r,s) &= \frac{\partial}{\partial r} h_{pq}(r,s)\Phi_{pq} \\ \left.\frac{\partial \Phi}{\partial r}\right|_{pq} &= \theta_{pq}\Phi_{pq} \end{aligned} \tag{2.5}$$

where the manipulation requires $\sim O(N^4)$ for 2D and $\sim O(N^6)$ for 3D analysis since the resulting matrix is full and the required matrix-vector multiplication is costly. The tensor-product form reduces the cost by splitting the interpolant dependence:

$$\Phi(r,s) = h_p(r)h_q(s)\Phi_{pq} \tag{2.6}$$

the differentiation is given by

$$\begin{aligned} \frac{\partial \Phi}{\partial r}(r,s) &= \frac{\partial}{\partial r} h_p(r) h_q(s) \Phi_{pq} \\ \left.\frac{\partial \Phi}{\partial r}\right|_{mn} &= D^r_{mp} \delta_{nq} \Phi_{pq} \\ &= D^r_{mp} \Phi_{pn} \end{aligned} \tag{2.7}$$

where D is the derivative matrix and (m, n) specify the location of derivative and (p, q) are neighboring collocation points. Differentiating in this way, the cost is $\sim O(N^3)$ for 2D and $\sim O(N^4)$ for 3D analysis. It is obvious that significant computational savings can be achieved especially in 3D analysis.

2.2.4 Arbitrary-Lagrangian-Eulerian (ALE) Method

One of the strengths of NEKTON is its capability to solve many different types of moving boundary problems including free surface analysis, multi-fluid layers, and phase boundaries [40]. The use of Arbitrary-Lagrangian-Eulerian (ALE) method allows for accurate representation of moving boundaries and a brief description is given here. More detailed description can be found in Ho [40].

Generally, the purely Lagrangian description suffers from excessive mesh distortion since mesh points are required to follow the motion of the corresponding fluid particles. Rezoning is often required to overcome the distortion of the mesh. The ALE method is based on the concept that the computational domain can deform independently of the fluid motion. Thus the mesh velocity is independent of the fluid velocity except at the moving boundaries where appropriate kinematic conditions must be satisfied [40]. Mesh velocity is defined at each collocation point to characterize the deformation, and once the

new boundary is determined, the elastostatic (elliptic) solver in NEKTON is used to solve the resulting boundary value problem. The new geometry is then computed by integrating the mesh velocity explicitly in time and updating the nodal coordinates of the collocation points. Note that geometry is updated using a Pth order (1,2, or 3) Adams-Bashforth multistep scheme.

With ALE capability already existing for the fluid solver, only the solid solver must adjust to the deformed geometry. Since the Lagrangian description is adequate and more natural for solids, ALE formulation was not required for the solid solver. With a boundary clearly identified, the same elastostatic solver is used to rearrange the collocation points in a new geometry.

2.3 Solid Solver

The creation of the solid solver was the central component of this thesis and the major coding effort. In this section, the different aspects of the solid solver, which had to be created entirely from scratch, are explained in detail.

In all of the equations, the summation convention of tensor notation is implied. In terms of notation, the left superscript represents the current configuration and left subscript represents the configuration for which the quantity is measured. If the left subscript is not given, it implies that quantities are measured in the current configuration. The notation follows Bathe [5] closely, and the main idea is borrowed from this reference.

2.3.1 Nonlinear Formulation

For linear analysis, the implicit assumption is that the displacements of the body are infinitesimally small and the material is linearly elastic. Consequently, the displacement is a linear function of the applied load. In nonlinear analysis, this is no longer valid. In this

section, the formulation of nonlinear analysis is described in detail to point out the difficulties associated with this type of analysis.

When the body undergoes large displacements and large strains, its volume, surface area, mass density, stresses and strains are changing continuously. This means that the equilibrium equation at t+Δt cannot be satisfied and the reference configuration must be considered. Note that this is a significant difference from the linear analysis in which small displacement assumption allows numerical integration to be performed over the original volume of the element.

The variational statement of equilibrium requires that

$$\int_{{}^{t+\Delta t}V} {}^{t+\Delta t}\tau_{ij}\delta_{t+\Delta t}e_{ij}\,{}^{t+\Delta t}dV = {}^{t+\Delta t}R \tag{2.8}$$

where the ${}^{t+\Delta t}\tau_{ij}$ are the Cartesian components of the Cauchy stress tensor and $\delta_{t+\Delta t}e_{ij}$ are variation in the Cartesian components of the strain tensor. Note that $\delta_{t+\Delta t}e_{ij}$ can be thought of as virtual strain, and therefore equation 2.8 represents the virtual work balance at time t+Δt. The corresponding external virtual work ${}^{t+\Delta t}R$ is given by

$${}^{t+\Delta t}R = \int_{{}^{t+\Delta t}S} {}^{t+\Delta t}f_i^s\,\delta u_i\,{}^{t+\Delta t}dA + \int_{{}^{t+\Delta t}V} {}^{t+\Delta t}\rho\,{}^{t+\Delta t}f_i^b\,\delta u_i\,{}^{t+\Delta t}dV \tag{2.9}$$

where ${}^{t+\Delta t}f_i^s$ and ${}^{t+\Delta t}f_i^b$ are the components of applied surface traction per unit area and body forces per unit mass, respectively, δu_i is a variation in the current displacement components ${}^{t+\Delta t}u_i$, and ${}^{t+\Delta t}\rho$ is the density. The surface forces are due to the viscous stresses and pressure on the sides of the control surface. They can be represented as:

$${}^{t+\Delta t}f_i^s = {}^{t+\Delta t}\tau_{ij}n_j \tag{2.10}$$

where n_j is the outward unit normal vector. For Newtonian fluid, the viscous stresses are proportional to the element strain rates and the coefficient of viscosity. Thus, the knowledge of the velocity components and pressure are enough to calculate the surface forces using equation 2.10. The actual components are shown in Appendix A.

It is important to keep in mind that the configuration of the body at time t+Δt is unknown. This is a very important difference compared to linear analysis, in which the displacements are infinitesimally small so that the original configuration does not change. For this reason, equation 2.8 cannot be solved directly and one must refer back to any one of the previously determined equilibrium configurations for an approximate solution. This solution can then be improved by iteration.

2.3.2 General Incremental Formulations

In practice, the most commonly used reference configurations are: initial configuration at time 0 of the body [Total Lagrangian (T.L.) formulation] or configuration at time t [Updated Lagrangian (U.L.) formulation]. Note that the only difference between the two formulations lies in the choice of the reference configurations for the kinematic and static variables. This means numerical efficiency will dictate the use of one over the other. Since our interest lies on small strain cases, the U.L. formulation is chosen for our analysis. Its advantage will become clear.

Referring back to time t, equation 2.8 is transformed to

$$\int_{{}^tV} {}^{t+\Delta t}_{t}S_{ij}\,\delta\,{}^{t+\Delta t}_{t}\varepsilon_{ij}\,{}^{t}dV = {}^{t+\Delta t}R \tag{2.11}$$

where ${}^{t+\Delta t}_{t}S_{ij}$ are Cartesian components of the 2nd Piola-Kirchhoff stress tensor and ${}^{t+\Delta t}_{t}\varepsilon_{ij}$ are Cartesian components of the Green-Lagrange strain tensor. These tensors are based on

the change from time t to time t + Δt and referred back to the configuration at time t. By definition, they are given by:

$$ {}_{t}^{t+\Delta t}S_{ij} = \frac{{}^{t}\rho}{{}^{t+\Delta t}\rho} {}_{t+\Delta t}^{t}x_{i,s} \, {}^{t+\Delta t}\tau_{sr} \, {}_{t+\Delta t}^{t}x_{j,r} \tag{2.12} $$

$$ {}_{t}^{t+\Delta t}\varepsilon_{ij} = \tfrac{1}{2}\left({}_{t}^{t+\Delta t}u_{i,j} + {}_{t}^{t+\Delta t}u_{j,i} + {}_{t}^{t+\Delta t}u_{k,i} \, {}_{t}^{t+\Delta t}u_{k,j} \right) \tag{2.13} $$

where ${}_{t+\Delta t}^{t}x_{i,s}$ are the components of the deformation gradient [5].

These quantities can be thought of as auxiliary stress and strain measures such that the incremental decomposition of the stresses and strains can be performed effectively. They are symmetric and objective (i.e. do not change in rigid body rotation). Note that the left-hand-side of equations 2.8 and 2.11 are equal but are defined with respect to the different configurations. Mathematically, they are energetically conjugate to each other. Performing the incremental decomposition, stresses and strains become

$$ {}_{t}^{t+\Delta t}S_{ij} = {}^{t}\tau_{ij} + {}_{t}S_{ij} \qquad \left({}_{t}^{t}S_{ij} = {}^{t}\tau_{ij} \right) \tag{2.14 ab} $$

$$ {}_{t}^{t+\Delta t}\varepsilon_{ij} = {}_{t}\varepsilon_{ij} = {}_{t}e_{ij} + {}_{t}\eta_{ij} \tag{2.15} $$

where the linear component of the increment strain is given by ${}_{t}e_{ij} = \tfrac{1}{2}\left({}_{t}u_{i,j} + {}_{t}u_{j,i} \right)$ and the nonlinear increment component is ${}_{t}\eta_{ij} = \tfrac{1}{2} {}_{t}u_{k,i} \, {}_{t}u_{k,j}$. The decomposition is allowed since all stresses and strains are referred to the same configuration at time t. Finally, the constitutive relationship between stress and strain increments is given as:

$$ {}_{t}S_{ij} = {}_{t}C_{ijrs} \, {}_{t}\varepsilon_{rs} \tag{2.16} $$

where ${}_tC_{ijrs}$ is the incremental material (elastic) property tensor at time t referred to the configuration at time t. Substituting equations 2.14 to 2.16 into equation 2.11 gives the new form of the equilibrium equation (variational statement):

$$\int_{{}^tV} {}_tC_{ijrs}\,{}_t\varepsilon_{rs}\delta_t\varepsilon_{ij}\,{}^tdV + \int_{{}^tV} {}^t\tau_{ij}\delta_t\eta_{ij}\,{}^tdV = {}^{t+\Delta t}R - \int_{{}^tV} {}^t\tau_{ij}\delta_t e_{ij}\,{}^tdV \qquad (2.17)$$

Note that no assumption has been made so far; equation 2.11 has merely been rewritten with respect to another configuration. The solutions of equation 2.17 cannot be calculated directly since they are nonlinear in the displacement increments. The nonlinearity comes

A Spectral Element Formulation for Fluid-Structure Interactions: Application to Flow Through Collapsible Channels

by

James Jang-Sik Shin

Bachelor of Science in Aerospace Engineering
(University of Southern California, 1990)

Masters of Science in Aeronautics and Astronautics
(Massachusetts Institute of Technology, 1992)

Submitted to the Department of Mechanical Engineering
in partial fulfillment of the requirements for the degree of

Doctor of Philosophy in Mechanical Engineering

at the

MASSACHUSETTS INSTITUTE OF TECHNOLOGY

September 1996

balance virtual work", the right-hand-side of equation 2.19, is zero. In reality, this means that iteration is continued until the equilibrium equation at time t+Δt is satisfied for a required tolerance. In terms of the increments, the resulting equation at iteration k is

$$\int_{{}^tV} {}_tC_{ijrs}\Delta_t e_{rs}^{(k)}\delta_t e_{ij}\,{}^tdV + \int_{{}^tV} {}^t\tau_{ij}\delta\Delta_t\eta_{ij}^{(k)}\,{}^tdV = {}^{t+\Delta t}R - \int_{{}^tV} {}^t\tau_{ij}^{(k-1)}\delta_t e_{ij}^{(k-1)}\,{}^tdV \qquad (2.20)$$

and the displacements are updated as

$${}^{t+\Delta t}u_i^{(k)} = {}^{t+\Delta t}u_i^{(k-1)} + \Delta u_i^{(k)} \qquad {}^{t+\Delta t}u_i^{(0)} = {}^tu_i \qquad (2.21\ ab)$$

In dynamic analysis, the inertia forces must be considered as the applied body forces. This means that in addition to the right-hand-side of equation 2.20, there exists an inertial term given as

$$\int_{{}^tV} {}^t\rho\,{}^{t+\Delta t}\ddot{u}_i\delta u_i\,{}^tdV \qquad (2.22)$$

Other than the introduction of the inertial term, nothing else changes in going from static to dynamic. In other words, dynamic analysis is in fact a static analysis including inertia effects.

2.3.3 Newmark Method

For time integration, the integration operators are broadly characterized as either explicit or implicit. Explicit schemes obtain values for quantities at t+Δt based entirely on available values at time t or before. The explicit methods require that the time step Δt be smaller than a critical Δt, and therefore they are conditionally stable. In contrast, implicit schemes solve for quantities at time t+Δt based not only on values at t, but also on these same quantities at

t+Δt . They are unconditionally stable such that the size of Δt is only limited by accuracy considerations, and therefore the values of Δt used for the implicit methods are generally much larger than their counterparts in explicit methods. Also, this implies that the convergence is always achieved provided Δt is small enough.

Among different implicit methods, the Newmark method is the most robust and does not require any special starting procedure. The Newmark integration scheme uses the assumption that:

$$^{t+\Delta t}\dot{U}={}^{t}\dot{U}+\left[(1-\delta)\,{}^{t}\ddot{U}+\delta\,{}^{t+\Delta t}\ddot{U}\right]\Delta t \tag{2.23}$$

$$^{t+\Delta t}U={}^{t}U+{}^{t}\dot{U}\Delta t+\left[\left(\tfrac{1}{2}-\alpha\right){}^{t}\ddot{U}+\alpha\,{}^{t+\Delta t}\ddot{U}\right]\Delta t^{2} \tag{2.24}$$

The Newmark integration method is based on the assumption that the acceleration varies linearly between two instants of time. The parameters α and δ indicate the relative weighting between the acceleration at the end of the interval and acceleration at the beginning, in terms of their influence on the velocity and displacement equations at the end of the interval Δt. For unconditional stability, δ = 1/2 and α = 1/4 (this particular choice is equivalent to the trapezoidal rule) leading to constant-average-acceleration method. Note that equations 2.23 and 2.24 can be rewritten as:

$$^{t+\Delta t}\ddot{U}=a_0\left({}^{t+\Delta t}U-{}^{t}U\right)-a_2\,{}^{t}\dot{U}-a_3\,{}^{t}\ddot{U} \tag{2.25}$$

$$^{t+\Delta t}\dot{U}={}^{t}\dot{U}+a_6\,{}^{t}\ddot{U}+a_7\,{}^{t+\Delta t}\ddot{U} \tag{2.26}$$

where $a_0=\frac{1}{\alpha\Delta t^2}$, $a_2=\frac{1}{\alpha\Delta t}$, $a_3=\frac{1}{2\alpha}-1$, $a_6=\Delta t(1-\delta)$, $a_7=\delta\Delta t$ are constants resulting from the time marching. At time t+Δt, we can solve for accelerations from

equation 2.25 and then velocities from equation 2.26 in terms of unknown displacements and known values at time t only.

It is important to note that unless δ is taken as 1/2, spurious damping is introduced proportional to (δ -1/2). If δ is taken as zero, negative damping results. Similarly, if δ is greater than 1/2, positive damping is introduced reducing the magnitude of the response even in the absence of real damping in the problem [66].

2.3.4 Equilibrium Equation

Section 2.3.2 explained the incremental formulation in terms of integrals and the importance of iteration is emphasized for the nonlinear analysis. The spectral element equations can be obtained when the variational principle is evoked at each collocation point. Once discretized, equation 2.20 results in the following matrix form.

$$M^{t+\Delta t}\ddot{U}^{(k)} + \left({}^{t+\Delta t}K_L + {}^{t+\Delta t}K_{NL}\right)\Delta U^{(k)} = {}^{t+\Delta t}R - {}^{t+\Delta t}F^{(k-1)} \tag{2.27}$$

and the displacements are updated by

$${}^{t+\Delta t}U^{(k)} = {}^{t+\Delta t}U^{(k-1)} + \Delta U^{(k)} \tag{2.28}$$

with the initial conditions

$${}^{t+\Delta t}U^{(0)} = {}^{t}U; \quad {}^{t+\Delta t}F^{(0)} = {}^{t}F \tag{2.29}$$

M is the mass matrix, K is the stiffness matrix, and ${}^{t+\Delta t}F^{(k-1)}$ gives the nodal point forces that correspond to the element stresses in this configuration. The object is to find the state of equilibrium of the body corresponding to the applied loads at time t + Δt by referring

back to the configuration at time t. It is emphasized here that the global coefficient matrices (M, K, etc.) are used as a convenient means to describe the governing equations. In reality, the global matrices are never assembled for the fast iterative solvers such as preconditioned conjugate gradient iteration (see section 2.3.5). Instead, the matrix-vector product is obtained at the element level.

Note that latest estimates for the nodal point displacements are used to evaluate the corresponding element stresses and nodal point forces ${}^{t+\Delta t}F^{(k-1)}$. This means that the right-hand-side of equation 2.27 represents the unbalanced load that still must be balanced by the element stresses. Incrementing the displacement continues until the unbalanced load is balanced and the increment in displacement effectively drops below required convergence. Only then, can we say that the new equilibrium position is determined.

When the actual motion of the solid is considered, our aim is to evaluate the equilibrium positions of the solid body at the discrete time points which will completely describe the solution path. Using equations 2.25 and 2.26, equation 2.27 transforms to

$$\begin{aligned}&\left(Ma_0+{}^{t+\Delta t}K_L+{}^{t+\Delta t}K_{NL}\right)\Delta U^{(k)} = \\ &{}^{t+\Delta t}R+Ma_0{}^{t}U+Ma_2{}^{t}\dot{U}+Ma_3{}^{t}\ddot{U}-\left({}^{t+\Delta t}F^{(k-1)}+Ma_0{}^{t+\Delta t}U^{(k-1)}\right)\end{aligned} \tag{2.30}$$

where $a_0=\frac{1}{\alpha\Delta t^2}, a_2=\frac{1}{\alpha\Delta t}, a_3=\frac{1}{2\alpha}-1$ are constants resulting from time marching.

In summary, note that the iteration loop is performed for each equilibrium time starting from time 0. At each time step, equation 2.30 is satisfied and then the solution is allowed to move to the next time step. The solution process described above is repeated for the next equilibrium position until the complete solution path has been solved. The importance of iteration is emphasized here again since any error admitted in the incremental solution at the particular time directly affects the solution at any subsequent time. This is more true for dynamic analysis in which path dependence may be an issue. In order to

minimize error accumulation, one minor adjustment was made in the calculations. Instead of using equation 2.28, the displacements are calculated by:

$$^{t+\Delta t}U^{(k)} = {}^{t}U + \sum_{q=1}^{k} \Delta U^{(q)} \tag{2.31}$$

Note that equation 2.28 and 2.31 are identical mathematically. Substituting equation 2.31 into equation 2.30, we obtain the following equilibrium equation. This is the actual form used in the simulation.

$$\begin{aligned} &\left(Ma_0 + {}^{t+\Delta t}K_L + {}^{t+\Delta t}K_{NL}\right)\Delta U^{(k)} = \\ &{}^{t+\Delta t}R + Ma_2\,{}^{t}\dot{U} + Ma_3\,{}^{t}\ddot{U} - \left({}^{t+\Delta t}F^{(k-1)} + \sum_{q=1}^{k-1} Ma_0 \Delta U^{(q)} \right) \end{aligned} \tag{2.32}$$

The mass matrix is geometry dependent and therefore must be included inside of the summation in equation 2.32. This would ensure a consistent mass matrix to be used in evaluating the summation term. Note that other global coefficient matrices and vectors are also geometry dependent since they are continuously updated during the iteration. For other simulations using direct solvers, the stiffness matrices are constructed at time t and used during the whole iteration process (or limited update) instead of being updated regularly at every iteration. This is necessary since the major computational cost comes from the construction of stiffness matrices and factorization. This approximation is often referred to as the "tangent stiffness" assumption in modified Newton method. In our solver, the stiffness matrices are never explicitly formed (see section 2.3.5), and therefore the cost is minimal to update during the iterations. This implies that our solution should converge faster due to the accurate representation of the stiffness.

Looking back at equation 2.20, note that we are involved with Cauchy stresses which are always referred to the configuration in which they occur. If the T.L. formulation was used, 2nd Piola-Kirchhoff stresses, which have no physical meaning, would have to be used. Thus equation 2.12 is required for physical interpretation at every step. In summary, any formulation based on continuum mechanics principle with nonlinear effects should give the same results if consistent material descriptions are used. For convenience and numerical effectiveness, U.L. formulation is used in our simulations.

2.3.5 Equation Solver

The preconditioned conjugate gradient method is chosen to solve the resulting system of equations. This method is well documented [31], and is often the method of choice for iterative solvers. For symmetric and positive-definite matrices, the preconditioned conjugate gradient iteration is efficient and robust and convergence is extremely fast with minimal storage requirements. However, this method has its own inherent drawbacks. It is important to note both the advantages and disadvantages involved in using this method compared to direct solvers such as Gaussian elimination.

The major disadvantage of direct methods is the memory requirement since a global coefficient (stiffness) matrix must be assembled. On the other hand, the iterative methods do not explicitly create a global coefficient (stiffness) matrix since the stiffness matrix is formed at the element level [69]. This ensures minimal storage requirements. Note that convergence is not guaranteed for the iterative solvers. Furthermore, the resulting matrix must be well-conditioned to expect rapid convergence. The issue of accuracy must also be dealt with. Direct solvers are accurate up to machine precision while indirect solvers are only accurate up to the specified tolerance. This means that care must be exercised in choosing the acceptable convergence requirement for solution accuracy when the iterative solver is used.

NEKTON is a higher order method which increases coupling of collocation values compared with low order methods. This means that the resulting matrices are usually asymmetric with significant memory requirements. In 3-D, the cost is even greater. We decided to pursue the preconditioned conjugate gradient solver since it is characterized by minimal memory requirement (order of number of collocation points in the mesh), but there exists a requirement that the resulting matrices must be well conditioned. If not, convergence problems may arise. In this particular instance, the iterative solver worked well in solving for solid displacement increments because the stiffness matrix is both symmetric and positive-definite. Convergence is often achieved in less than 10 iteration loops.

2.3.6 Convergence Criterion

At the end of each iteration, the solution must be checked to see whether it has converged within the user-specified tolerances or whether it is diverging. In order to obtain an accurate solution, the tolerance must be tight; numerical experimentation is needed to determine the required tolerance. It is noted here that if the tolerance is too tight, too much computational effort is required; if too loose, an erroneous solution can result.

The displacement convergence check is given by:

$$\frac{\left\|\Delta U^{(K)}\right\|_2}{\left\|{}^{t+\Delta t}U^{(k)}\right\|_2} < TOL = 0.0001 \tag{2.33}$$

This means we are comparing the increment in displacement to the approximated total displacement at time t + Δt. When this ratio falls below the required tolerance, we assume that the new equilibrium position is correctly determined (up to the convergence tolerance). This criterion was a logical choice since the incremental correction in displacement approaches zero near the new equilibrium configuration. Note that in some analyses (e.g.

elastic-plastic analysis), the actual solution may still be far from the value obtained when convergence is measured using equation 2.33. This is the case when the calculated displacements (i.e. denominator) change only slightly in each iteration. In reality, some researchers include the force (right-hand-side out-of-balance load vector) convergence along with internal energy convergence [5]. All three convergence requirements were monitored during simulations. In most of the runs performed, tolerance (TOL) of 0.0001 was sufficient using equation 2.33 to ensure an accurate solution.

2.3.7 Solver Capabilities

The incorporation of the solid solver to NEKTON was implemented in stages to ensure that the programming was correct and manageable. First, the capability to simulate a steady, linear solid was incorporated. This step set the groundwork for further complexities. Secondly, the dynamic simulation capabilities were incorporated. Thirdly, geometric nonlinearlities were included allowing for large displacements. The resulting formulation is general enough that extensions to the code can be easily added. The completed model can handle either plane stress or plane strain analysis, and the capabilities of thermal strains, body forces, user-specified forces, initial displacements, material nonlinearities, and internal dampings are allowed.

Solid boundary conditions can be free, fixed, sliding, fluid solid interface, elemental, or imposed traction both locally and globally. The hinged wall, capable of simulating the pinned condition, was also incorporated. In POSTNEK (post-processor of NEKTON), a modification was made to show both x and y displacements in place of velocity components and one stress components (user-decided) instead of pressure. This allows for easier analysis and interpretation of the results.

2.3.8 Structure of the Solid Solver

The components of completed solid solver are described next in outline form (Table 2.1). The emphasis here is on coding flexibility so that extensions can easily be made. The key point to note here is the calculation of stresses. Since we are using the incremental formulation in displacements, updating the stresses (thus strains) incrementally is a natural extension and more consistent from the geometric perspective. This is similar to the hypoelastic model in which incremental stresses are calculated from the incremental strains. At every iteration, stresses are updated by:

$$\tau_{ij}^{(k)} = \tau_{ij}^{(k-1)} +_t C\Delta e_{ij}^{(k)} \tag{2.34}$$

instead of basing on the total displacements at every increment.

During the equilibrium iteration, there are several quantities that require special care. The F matrix of equation 2.32 must be based on the latest geometry since it represents the current internal forces resulting from the displacements. Without the proper geometry update, F does not change, and therefore new equilibrium cannot be approached. Only when the right-hand-side of equation 2.32 approaches zero, convergence is achieved. For proper geometry update, all the geometric quantities (local derivatives, Jacobian matrix) must be updated consistently with the current geometry.

1) Introduce all user-specified and body forces in the original geometry configuration.

§ If dynamic, include inertia effects as part of body forces.

2) Introduce all displacement boundary conditions.

3) Calculate boundary traction forces by:

§ Identify the fluid-solid interface.

§ Calculate surface traction forces from known stresses and pressure (see Appendix B).

§ Transfer over to solid face as a external force node-by-node fashion.

4) Solve for new equilibrium position subject to above external forces:

§ Gather components of stress-strain (C) matrix.

§ Compute thermal strains.

§ Calculate incremental strains based on incremental displacements.

§ Calculate the incremental stresses and update the overall stresses.

§ Create F vector and obtain effective right-hand-side force vector (see equation 2.32).

§ Create the stiffness matrices (both linear and nonlinear) elementally.

§ Calculate the new increment in displacement via conjugate gradient solver.

§ Update displacements and solid geometry.

§ Check for convergence using equation 2.33.

If not converged, return to 4)

5) If dynamic, calculate solid velocity and acceleration.

Table 2.1 Outline of the steps involved in the solid solver.

2.4 Segregated Approach

The last programming issue to consider is the actual coupling between two domains. There are basically two ways to solve the resulting fluid and solid equations. The first method requires solving both fluid and solid domain simultaneously, generating a coupled coefficient matrix with both solid and fluid parameters as unknowns while satisfying the interfacial quantifies such as displacements, velocities, and accelerations. There are several drawbacks to this approach. The resulting matrix is large, especially for the spectral element method which is higher-order and therefore contains much more coupling among collocation points. The resulting matrix has a large bandwidth and computational cost would be significant for its direct inversion. Theoretically, we can use indirect solvers utilizing methods like a conjugate gradient solver. Mathematically we know that indirect solvers work well for symmetric and positive-definite matrices. Since the resulting matrix will be denser and may no longer be symmetric and/or positive-definite, convergence may be slow or the solution may not converge at all. Furthermore, this step requires the total restructuring of NEKTON to accommodate solid parameters and will require significant coding effort.

For these reasons, we decided to pursue the segregated approach. In this case, the coupling occurs only at the interface; consequently, the solid solver is independent from the fluid solver. This means the solid only feels the resulting traction forces from the fluid domain. As for the fluid domain, the existence of the solid solver will result in a moving boundary problem since the no-slip condition at the interface is always enforced. The key to the segregated approach is the proper geometry update to ensure that the interface is always consistent for both domains. Otherwise, overlapping or gaps will inevitably result in convergence problems.

It is noted that the iterative approach employed here is often referred to as Picard iteration in the literature. This method is effectively used in solving for Navier-Stokes equations since iteration can be used to isolate the nonlinear (convective) term as a linear term based on previous value of velocities [17]. The term Picard iteration has been loosely used in recent years for all types of iteration approaches to the solution method. To our knowledge, no one has successfully used Picard iteration to solve both fluid and solid domains, and thus it is difficult to validate our code (see Chapter 3).

2.4.1 Geometry Update

The issue of geometric update is crucial during the geometrically nonlinear analysis. When the solid domain responds to the applied forces from the fluid, the geometry must readjust from the interface so that no gaps will form between domains. Note that all geometric quantities, including Jacobian matrix components and local derivatives, must be updated also. This will ensure that all geometric quantities are consistent respect to the new geometry.

NEKTON uses the Arbitrary-Lagrangian-Eulerian (ALE) Method to ensure that the moving fronts are tracked with minimum distortion. The solid is in Lagrangian form to begin with. For solid mechanics, the Lagrangian form is the description of choice since it represents a more natural and effective analysis approach. Only in special circumstances, such as analysis of rubber elasticity, do the elements become unacceptably distorted and require rezoning. For this reason, we will use the Lagrangian description for the solid. When significant distortion is encountered, the meshes are refined instead of rezoned during the calculation process.

2.5 Model Limitations

It is important to realize the foundation behind our solid solver and its limitations concerning the types of analysis possible. The resulting solver does allow for large displacements and large rotations, but only small strains. This does not impose any restriction on the stress-strain relation which maybe linear or nonlinear. Most of the results here employ linear elasticity, but material nonlinearity can be introduced using appropriate material descriptions. Elasticity implies that stress is a function of strain only and follows same stress path on loading and unloading [5]. This means only the actual straining of the material will yield an increase in the components of the stress tensor. Linearity implies that the material matrix C in equation 2.16 stays constant independent of strain locally. As long as the stresses are small, this is not a bad approximation for many physical materials. This is equivalent to using generalized Hooke's law for an isotropic material in a small strain analysis. The material matrix C is given by:

$$ {}_tC_{ijrs} = \lambda\delta_{ij}\delta_{rs} + \mu\left(\delta_{ir}\delta_{js} + \delta_{is}\delta_{jr}\right) \tag{2.35} $$

where λ and μ are Lamé constants and δ_{ij} are Kronecker delta. These constants are given by:

$$ \lambda = \frac{E\nu}{(1+\nu)(1-2\nu)} \tag{2.36a} $$

$$ \mu = \frac{E}{2(1+\nu)} \tag{2.36b} $$

Restricting ourselves to two dimensions only, the solid solver can solve two types of stress-strain relationships. The first type consists of plane stress elements which are employed to model membranes, the in-plane actions of beams and plates. This means τ_{zz}, τ_{xz}, and τ_{yz} are equal to zero. Plane strain elements are used to represent a slice of the structure in which ε_{zz}, γ_{xz}, and γ_{yz} are set to zero. The actual stress-strain matrices are given in APPENDIX B.

In practice, there are many other types of materials that can be modeled including hyperelastic model for rubbers and hypoelastic model for concretes. For hyperelastic materials, stresses are calculated from a strain energy function W which depends on strain tensor invariants and must be determined by experiment. More complex material descriptions exist for elastic-plastic behavior and creep. Again, experiments are required to properly describe the material behavior.

Chapter 3

Verification of Numerical Approach

3.1 Solid Only Comparison

Once the solid solver was completed, many simple test cases in solid analysis were performed for verification. As an ultimate check, the published results of Bathe, Ramm, and Wilson [3] were chosen to verify the completed solid solver. In their paper, they examined the nonlinear analysis for both Updated Lagrangian (U.L) and Total Lagrangian (T.L.) formulations for large deformations and emphasized the importance of equilibrium iterations within the solid solver. This analysis was comparable to our simulations since essentially the same nonlinear formulations were used. The test case - the large motion of cantilever beam subjected to the uniformly distributed load - is shown in Figure 3.1, while parameter values are shown in Table 3.1.

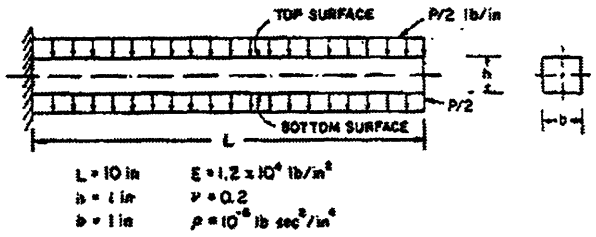

Figure 3.1 The large deformation of a cantilever beam subjected to a uniformly distributed load (from Bathe, Ramm, and Wilson [3]).

Length	L = 10 in
Thickness	h = 1 in
Width	b = 1 in
Poisson's Ratio	$\nu = 0.2$
Young's Modulus	$E = 1.2 \times 10^6$ lb/in^2
Density	$\rho = 10^{-6}$ lb*sec^2/in^4

Table 3.1 The parameter values used in cantilever analysis.

3.1.1 Load Step Increments

For large values of the applied force, the resulting displacements may be so large as to cause problems in the convergence of the solution. For this reason, the "ramping" or "restart" technique is very important in static analysis. This technique involves an incremental increase in loading. Intermediate converged solutions are obtained for each increment. Larger loading is "restarted" from the previously determined equilibrium and therefore requires far fewer steps to converge. In short, ramping makes it possible to obtain converged solutions even for large loading cases.

3.1.2 Static Comparison

Figures 3.2 and 3.3 show the comparison between static results. Bathe, Ramm, and Wilson [3] used five 8-node plane stress elements while we used five standard 25-node elements. The results are presented in terms of the deflection ratio (ratio of tip deflection to length) for different values of the load parameter K which is defined by:

$$K = \frac{PL^3}{EI} \tag{3.1}$$

where P is the applied distributed load. For the linear case, the maximum deflection of the beam is well documented for various boundary and loading conditions [65]. Here, it is given by:

$$\delta_{max} = \frac{PL^4}{8EI} = 1.25P = 1.25K \tag{3.2}$$

The results from both simulations indicate that linear solutions are reproduced according to equation 3.2. For nonlinear simulations, Figure 3.2 shows Bathe's result for four different formulations (explanation of Jaumann stress rate can be found in [3, 5]). The center curve of Figure 3.2 shows that nonlinearity cannot be correctly captured without the equilibrium iterations. We can see that the cantilever is stiffer for larger load parameters due to nonlinearities in the stiffness matrix associated with large deformations. The stiffening behavior of the cantilever is well captured in both simulations and agrees well with the analytical result reported by Holden [42].

The ramping technique was very important in obtaining solutions for large K. Without it, convergence difficulties started around K = 4; solutions for larger K were not possible. Twenty appeared to be an optimal number of increment steps, and only required about 3 equilibrium iterations. The importance of "restarting" will be emphasized again in the context of other static simulations. Note that if the number of increment steps approaches infinity, the nonlinear curve should be reproduced without any equilibrium iterations. This is possible since the linearization about small increments is done along the loading path. Table 3.2 shows the effect of increasing the load increment. With the load

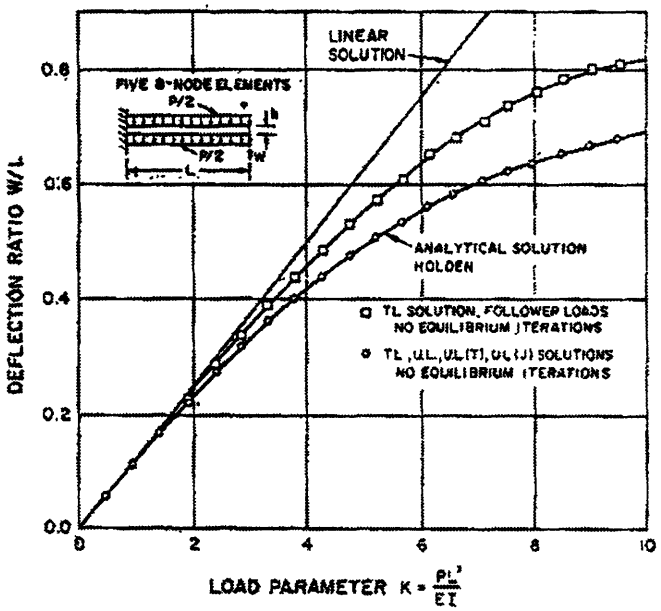

Figure 3.2 The large deflection analysis of a cantilever beam under a uniformly distributed load (from Bathe, Ramm, and Wilson [3])

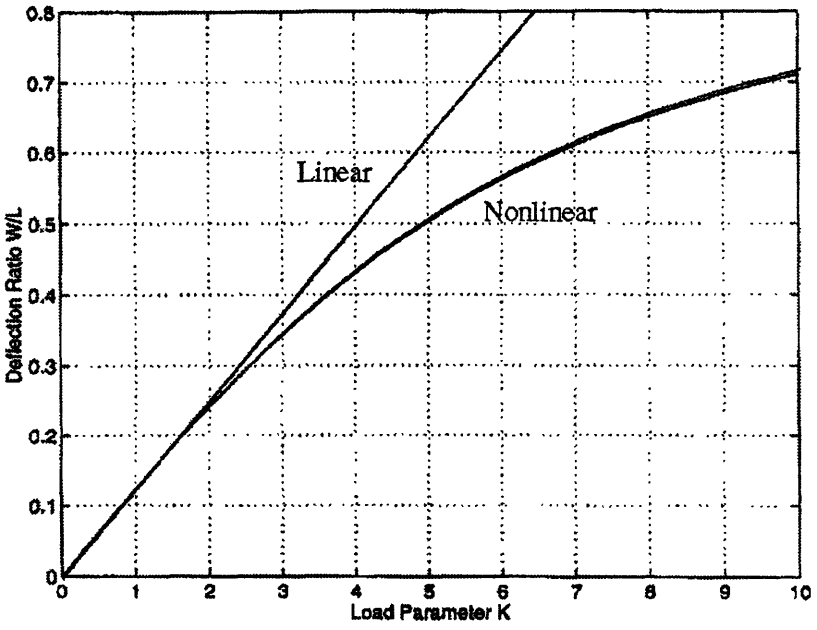

Figure 3.3 The corresponding cantilever simulations using the solid solver.

increment of twenty without equilibrium iterations, the solution overshoots the actual nonlinear solution by as much as 7%. As the number of load increment increases, the error in deflection is quickly controlled and approaches the correct value. The correct trend of behavior further shows the accuracy of the code and also the importance behind the load incrementing procedure.

Load Increment	Deflection Ratio (W/L)
20	0.76555
100	0.74184
250	0.73847
500	0.73735
1000	0.73680
Actual	0.714067

Table 3.2 The effect of increasing the load increment without performing the equilibrium iterations.

3.1.3 Dynamic Comparison

The dynamic results are shown in Figures 3.4 and 3.5. To study the dynamic behavior, an impulse load was applied at t = 0 with a magnitude of 2.85 lb/in. For lateral forcing, the period can be easily determined [13, 66]. The fundamental modes are given by:

$$f_i = \frac{\lambda_i^2}{2\pi L^2}\left(\frac{EI}{m}\right)^{1/2} \tag{3.3}$$

where λ_i is a dimensionless parameter which is a function of the boundary conditions applied to the beam, L is the length of the beam, m is the mass per unit length of the beam, E is the Young's modulus, and I is the moment of inertia. For the fundamental mode, λ_1 = 1.875104 for one fixed end and one free end. The parameter values give the period (T_f) to be about 57.3 x 10^{-4} sec; this is witnessed in the actual simulation. Knowing the period of the beam, it is important to have small enough Δt to resolve the oscillation accurately. Two time steps: Δt_1 = 0.45 x 10^{-4} sec which is roughly $T_f/126$ and $\Delta t_2 = 3 \times \Delta t_1$ are examined. In both cases, the Newmark Method is employed with $\alpha = 1/4$ and $\delta = 1/2$. Since this method is an unconditionally stable, the time step must only be small enough to ensure accuracy.

Figure 3.4 indicates that the correct amplitude is not captured in the linear analysis since the additional stiffness due to nonlinearity is not taken into account. For the nonlinear case, Bathe, Ramm, and Wilson again showed the importance of equilibrium iterations by showing the over-reduction in the amplitude (see dashed curve in Figure 3.4). With equilibrium iterations, the use of two different time steps did not seem to affect the solution. Note that they used the T.L. formulation in generating these solutions.

For linear solution, the results obtained with our spectral element method are essentially identical to the result of Figure 3.4, but for nonlinear analysis, this was not quite true. For our simulation, the smaller time step (Δt_1) reproduces their result, but our result from the larger time step (Δt_2) suffered from a slight reduction in amplitude and period. When we used smaller time steps than Δt_1, the results are indistinguishable from the results with Δt_1 suggesting that accuracy requirement is met. The source of the difference in behavior between Bathe et al. and our results is not clear beyond the fact that different formulations (T.L. vs U.L.) are used. In the limit in which the time step approaches zero,

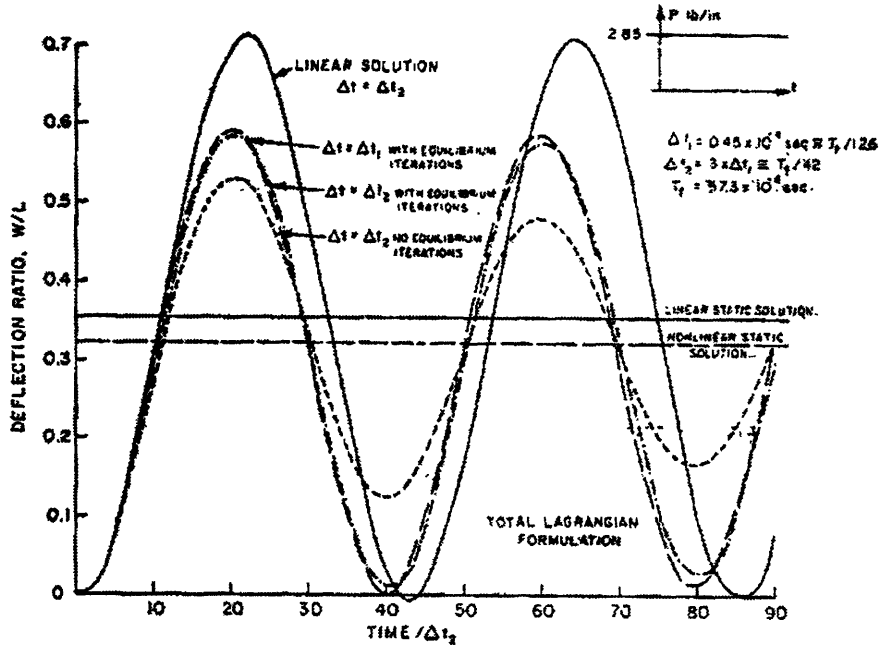

Figure 3.4 Large displacement dynamic response of a cantilever under a uniformly distributed load (from Bathe, Ramm, and Wilson [3]).

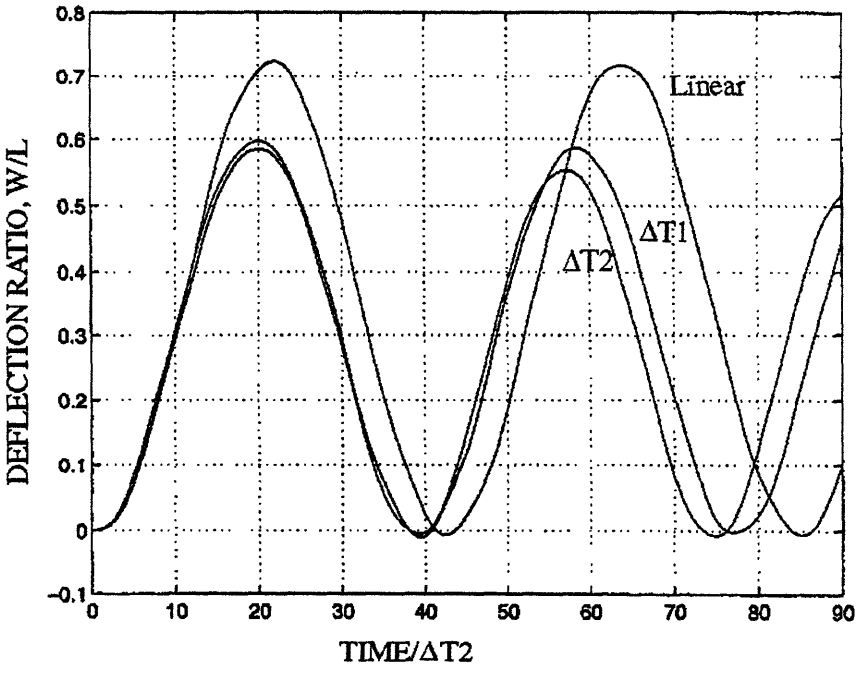

Figure 3.5 The corresponding dynamic simulations using the solid solver.

the correct results are obtained. This, along with the accuracy in simulation obtained from other simple analysis, confirmed that our completed solid solver is correct. As a final check, the solid density was set to zero. This means the inertia effects would disappear in the analysis. As expected, the displacement quickly rose to the corresponding static deflection ratio and maintained its value thereafter.

In summary, this section shows that the newly created solid solver can effectively handle large displacements of a solid, both steady and unsteady, by properly taking into account geometric nonlinearities associated with large deformation. Now, the task is to properly link the solid solver with the fluid solver and consider fluid-structure interactions.

3.2 Steady Fluid-Structure Interaction

Experimental results exist from our laboratory which examine the effect of the tapered wall thickness on flutter phenomena [1, 62]. The tapering localizes the oscillation to the center of the tube and therefore succeeds in minimizing the end-effects and perhaps is a better representation of the real physiological situations. It would be ideal to compare computational results with experimental observations. But , as will be shown, direct comparison to these results is difficult since the experiments typically lie in the fully turbulent regime. Furthermore, these experiments have been performed with tubes, not a 2-D configuration. However, Grotberg[33, 34] has shown that flow oscillation can be generated without the presence of turbulence and in the 2-D configuration. Our objective is to study the oscillation mechanism rather than reproducing the experimental results so we consider, as did Grotberg, 2-D laminar flows.

3.2.1 Numerical Technique

In order to reduce the problem setup time, all the runs are performed with the minimum number of elements to describe the geometry (with proper boundary and initial conditions). Once the solution of the initial coarse mesh is available, further refinement is added to provide sufficient resolution. For example, high resolution is required for the region of flow separation and of high Re simulations. Otherwise, divergence of the solution can occur in the fluid domain due to lack of resolution.

For moving geometry problems, the physics of the problem may result in large mesh distortion and runs may terminate prematurely. High resolution of the mesh, in the region of expected large distortion, is required to keep the aspect ratio of each element reasonable. Note that for spectral elements, the accuracy can be improved by increasing the order of interpolants (NORDER) instead. For most of the runs, mesh refinement was used instead of increasing NORDER varying NORDER does not reduce the extent of distortion. Unless specified, simulations were performed with NORDER of five (i.e. 25 collocation points) and NORDER was increased to seven for a check for accuracy only. It appears that the advantage of using spectral method might be lost, but, the number of required elements is much less compared to the traditional finite elements (see [69] for more detail).

3.2.2 Convergence of the Two Domains

Figure 3.6 shows the actual steps involved in simulating steady fluid-structure interactions. Note again that the two domains are independent of each other. First, the Navier-Stokes equations are solved in the fluid domain. Once the components of velocity and pressure are known, the traction forces are calculated (see Appendix A). Then the solid solver determines the new equilibrium condition corresponding to these "external" forces. The

transfer of the traction forces are done in a node-by-node manner. This is possible since the same collocation points are used and therefore no ambiguity exists during the transfer process. The convergence requirement is chosen such that ratio of maximum displacement (since last iteration) to a characteristic length (usually chosen to be the thickness) falls within a required tolerance. This is similar to the convergence criterion used in free surface analysis [40]. If the convergence condition is not met, then the whole process repeats after the new mesh locations are determined to ensure compatibility of two domains. In practice, tolerance of 0.001 was enough to have a converged solution. the first iteration is where the most displacement would occur. Subsequent iterations are minor modifications to the final configuration and this means that the rate of convergence rapidly slows as the iteration counter increases. The required iteration was often less than 10. Cases that require more than 100 iterations never converged. Thus maximum iteration counter (MXGEOM) was set at this value; when reached the run stops.

Note that the direct solver is used for the fluid solver. This is because the Navier-Stokes equations result in an asymmetric global matrix due to the nonlinear convection term. The convergence difficulties expected for an iterative solver, and NEKTON's direct solver, which involves Newton-like iterations, was used to solve the fluid domain. Since we limited the simulations to two dimensions, the memory requirement was manageable, and the runs proceeded without any difficulties from the fluid solver.

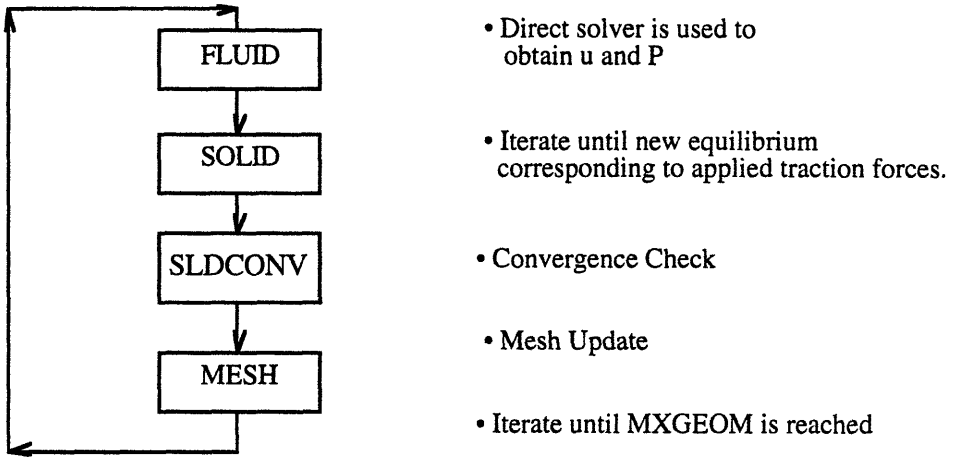

Figure 3.6 The computational path showing the steps involved in steady fluid-structure interactions.

3.2.3 Membrane Simulations

The results of Luo and Pedley [55] are chosen for comparison with the steady fluid-structure interaction simulations. Luo and Pedley used the Navier-Stokes Solver FIDAP for their fluid domain but their wall was limited to the membrane assumptions. Their study examined the required initial tension to obtain converged solution for Reynolds numbers (Re) between 1 and 600.

Figure 3.7 shows the computational domain used by Luo and Pedley. Boundary conditions on velocity are those of no-slip at the side walls (segments ED, CB, and OFA) and a parabolic velocity profile at the entrance (EO). Parallel outflow is assumed (BA), implying that the vertical component of velocity is zero and normal stress is constant at the outflow boundary. This condition is referred to as "outflow normal" (ON) in NEKTON, and it is a fair approximation if the downstream length is long enough to ensure that the parallel flow condition prevails at the flow exit.

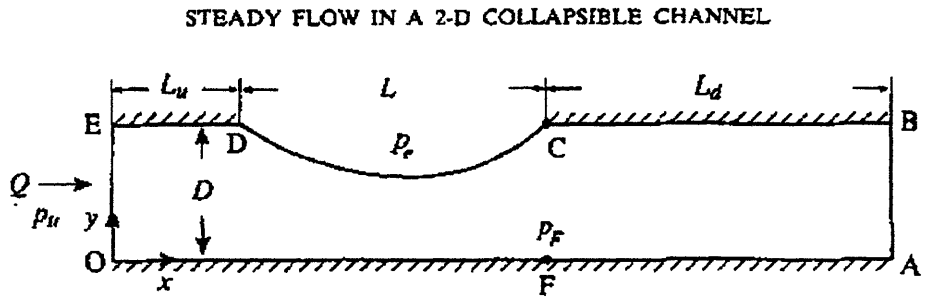

Figure 3.7 The computational domain used by Luo and Pedley [55].

The parameter values used in Luo and Pedley simulation are shown in Table 3.3. The working fluid is water and the parameter values correspond to the previous work [53] for comparison purposes. We adopted identical values; additional required parameters were set to be: E = 10 Pa, $\nu = 0.2$, and the thickness of the wall (h) is chosen to be 10% of the channel width. This means the aspect ratio of the wall is 50:1 and approximates the thin wall reasonably well.

Note that membrane simulations of Luo and Pedley and others [53, 55, 56, 67] faced difficulty in identifying the location of mesh points. For the membrane (elastic boundary), the location of mesh points is not known since a membrane equation is used to describe the wall mechanics and individual mesh points are not tracked as in our simulation. They make an assumption that mesh points always move in the direction normal to its surface. Furthermore, the fluid mesh points that lie under the elastic boundary are not precisely tracked since the ALE method is not used. They assumed that mesh points lie along a splines which emanate from a fixed origin outside of the elastic boundary. The solid solver presented here does not suffer from these limitations and bypasses the arbitrary procedures for allocating mesh points of Luo and Pedley.

Luo and Pedley used a parameter β, which can be thought of the scaling factor from the original tension specified in the wall. This means that if $\beta = 35$, $T = T_O/35$ acts on the

wall. Higher β implies lower initial tension in the wall and that the wall will be subject to greater deformation.

Fluid Density	$\rho = 1000\ kg/m^3$
Fluid Viscosity	$\mu = 0.001\ Pa*s$
Channel Width	$D = 0.01\ m$
Collapsible Length	$L = 0.05\ m$
Upstream Length	$L_u = 0.02\ m$
Downstream Length	$L_d = 0.07\ m$
Initial Tension	$T_o = 1.610245\ N/m$
External Pressure	$P_e = 0.93\ Pa$

Table 3.3 The parameter values used by Luo and Pedley [55].

3.2.4 Criteria for Comparison

The membrane assumption implies that the wall is a thin, uniformly elastic sheet which can support only tensile loads in its own plane. Hence bending rigidity does not exist. Membranes deflect purely due to the pressure difference across the membrane. Since our treatment of the wall is different, the exact one-to-one comparison is not possible. Specifically, E, ν, and h must be adjusted to have a valid comparison. Fair comparison is still possible if we can satisfy the condition derived below.

We must ensure that the tension contribution is dominant over the bending contribution that exists due to the finite thickness of the wall. Estimating from the Von Karman plate equation [52], we know that:

Bending Stiffness: $DW_{xxxx} = \frac{Eh^3}{12(1-\nu^2)} W_{xxxx}$

Longitudinal Tension: $TW_{xx} = \sigma h W_{xx}$

where σ indicates the tensile stress existing in the wall. The implicit assumption is that initial tension dominates over the additional tension resulting from the deformation. Requiring tension to be much greater than bending effects, we obtain the following relationship for required initial stress:

$$\sigma >> \frac{E}{12(1-\nu^2)}\left(\frac{h}{L}\right)^2 \tag{3.4}$$

As long as h is small with respect to L, the requirement can be easily satisfied. The above condition must be satisfied at all times for our validation to be meaningful. For the Luo and Pedley geometry, this requirement is easy to satisfy for large tensions (i.e. small β) but becomes difficult when the tension is low (i.e. large β).

3.2.5 Initial Tension Effect

The initial tension, which contributes to the stiffness, is required to sustain the lateral forcing for membranes. Numerically, the stiffness matrix is singular without initial tension, and therefore finite initial tension must be employed. For a real solid, the bending stiffness effects can allow the solid to limit the deflection so that stiffness in lateral forcing

is present even without the initial tension contribution. The initial tension increases the stiffness via K_{NL} (nonlinear stiffness component), which scales as P/L, where P stands for the total force acting within, including the initial tension. This is the only mechanism to resist lateral forcing for membrane walls. Note that the specified thickness of the wall is the post-stretched thickness. The clarification is required since a real solid cannot maintain the same thickness if the initial tension is removed. Both strains and stresses are defined respect to this thickness.

Since the applied initial tension is always axial in the local coordinate system, transformation to the global coordinate system is required to properly take it into account. The coordinate transformation (in 2-D about the z-axis) is described in Appendix C. The initial tension capability was incorporated into the solid solver and verified with ABAQUS in two stages. The first case is the cantilever is subjected to uniform pull with initial tension applied. The second test was the lateral forcing to ensure that angle calculation is properly taken into account. Figure 3.8 shows the first test case and Table 3.4 shows the parameter values used for the simulations. The external forcing (R) is varied and the corresponding tip displacement and internal axial stress were monitored. Note that standard eight-node elements were used in ABAQUS and standard five-by-five spectral elements were used for our solid solver. Total of five elements were used in both cases.

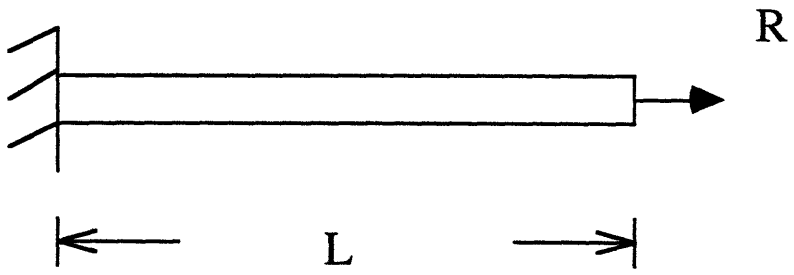

Figure 3.8 The test case: a solid subjected to uni-axial pull with initial tension specified.

Young's Modulus	10 Pa
Poisson's Ratio	0.0
Thickness	1.0 m
Length	10 m
Initial Stress	10 Pa

Table 3.4 The parameter values used for uni-axial test case for the initial tension effect.

Table 3.5 shows the comparison between the solid solver and ABAQUS for three different values of axial pull. The first thing to note is that when the pulling load equals the initial tension, no displacement occurs. This means R must be greater than R_I (initial tension) to have a positive displacement. Since the precise formulation used in ABAQUS is not known, identical magnitudes are not expected. Nevertheless the solid solver is capable of reproducing the simple hand-calculated solution, and the comparison to ABAQUS is yet another check to ensure that initial tension effect is properly taken into account.

The next testing case is shown in Figure 3.9. This time, lateral forcing was introduced to ensure that the angle transformation is correctly performed. R = -1 Pa was used in the simulations and the comparisons are shown for a variety of values of Young's modulus in Table 3.6. Note that there exists a cross-over value of E at which ABAQUS solution gives larger deflection than the solid solver. Again, the precise formulation behind ABAQUS is not known, and therefore exact comparison was not possible. Nevertheless, ABAQUS solutions were useful comparison beyond what could be done by simple hand calculation.

R (Pa)		Tip Displacement (m)	Axial Stress (Pa)
8	A)	-0.2154	7.829
	B)	-0.1963	8.001
10	A)	0.0	10.0
	B)	0.0	10.0
12	A)	0.2293	12.270
	B)	0.2037	12.000

Table 3.5 The uni-axial comparisons for tip displacement and the axial stress between A) ABAQUS and B) the solid solver for R = 8, 10, 12 Pa.

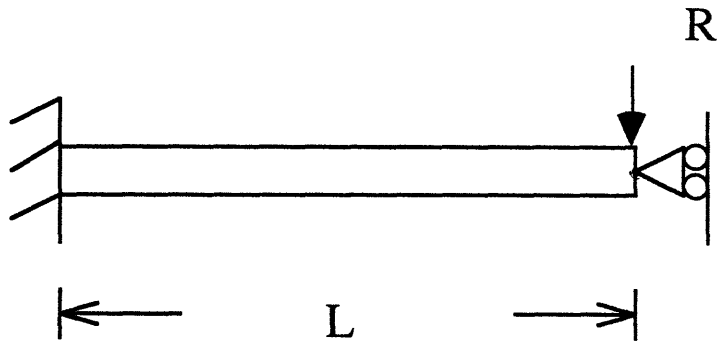

Figure 3.9 The test case: a solid subject to lateral forcing with initial tension specified.

E (Pa)	ABAQUS (m)	Solid Solver(m)
75	-1.616	-1.700
100	-1.600	-1.639
150	-1.576	-1.564
200	-1.556	-1.515
300	-1.522	-1.448

Table 3.6 The comparison between ABAQUS and the solid solver for a solid subject to lateral forcing. The results are for various values of Young's modulus.

Another numerical modification was the under-relaxation technique to ensure that collapsed wall does not touch the other side of wall prematurely. The overshoot is minimized by ensuring that if the new displacement is greater than the channel width, only a small fraction of the total displacement is taken to be the actual displacement. A similar technique was used by Luo and Pedley [55]. Note that as the equilibrium configuration is approached, the modification on displacement is small and under-relaxation is no longer invoked. Hence, it was most crucial for the first update when the largest change in displacement is seen. Mathematically, this means that coordinate updates are done by:

$$X^{n+1} = X^n + \psi \sum \Delta U \tag{3.5}$$

where ψ is the coefficient to ensure that wall deformation is less than the channel width. This ensures that distortion of geometry is minimized. Note that the implicit assumption is that the converged solution exists and that it is less than the channel width. If these

conditions do not hold, the solution will fail with or without under-relaxation. Care must be taken in calculating the quantities that are based on geometry such as geometric derivatives and the F vector. They must be based on the under-relaxed geometry, not the actual geometry.

3.2.6 Results and Discussion

For steady simulations, the runs were performed using the "restart" technique. This means that higher Re runs were started with the result of the lower Re solution as the initial condition of the simulation. This speeds up the convergence of the solution and also makes convergence possible for runs that would otherwise be unstable; this is analogous to the "ramping" done in the solid verification stage (see section 3.1). In steady simulation, this is a perfectly acceptable procedure since the path through which the convergence is achieved is irrelevant to the final converged solution.

Figures 3.10 and 3.11 show the result for Re = 1. The results of Luo and Pedley are well-reproduced by this simulation. To ensure the tension-dominant inequality of equation 3.4, E = 10 Pa was used in the simulation. Note that if E is increased, the wall is stiffer, and therefore, the solution can be obtained for larger β than Luo and Pedley solutions.

For the solid boundary condition, both fixed and hinged wall cases were attempted. A hinged wall is more similar to the membrane since bending effects at the ends of the membrane are minimized. Computationally, the hinged wall ran into difficulties since the collapse was always too severe. Even with under-relaxation technique in deflection, the difficulties persisted. For this reason, the runs were simulated using the fixed wall while ensuring that the criterion given by equation 3.4 is satisfied always. Bending effects are inevitable near the boundary ends but these effects were localized and did not seem to affect the overall solution.

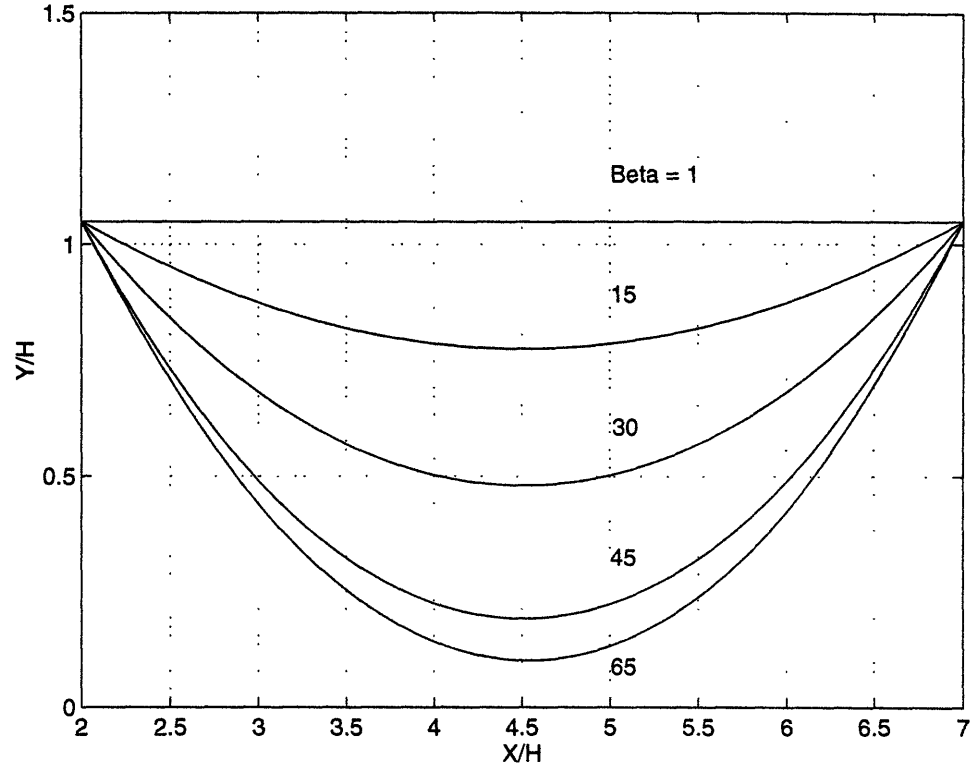

Figure 3.10 The wall shapes obtained from the solid solver for Re = 1 and β = 1,15, 30, 45, 65.

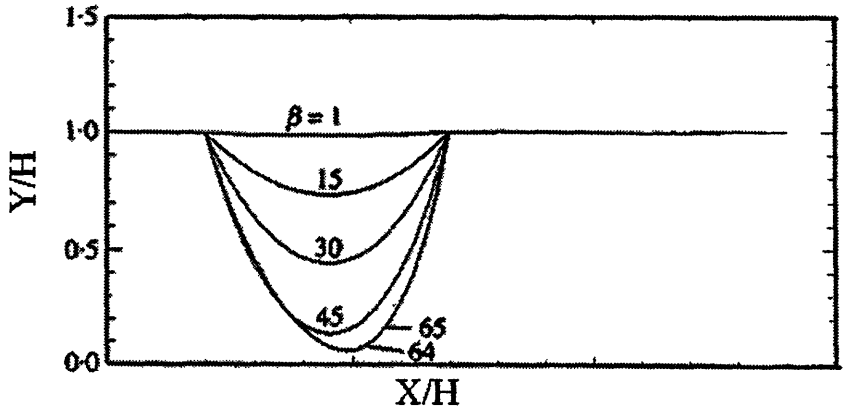

Figure 3.11 The wall shapes obtained from the numerical calculations for Re = 1 and $T = T_O/\beta$ where β = 1,15, 30, 45, 64, 65 (from Luo and Pedley [55]).

Note that Luo and Pedley assumed constant tension during the deflection process. This is not true, of course, during collapse, when deformation of the wall and the viscous force that acts on it result in variation of the tension in the wall. Our calculations show that tension can vary up to about 6% for $\beta = 65$ and $Re = 1$. Furthermore, the elastic membrane model used for the compliant wall neglects the effects of bending stiffness since it assumes that the wall is thin. Although this is reasonable when the wall tension is large, bending stiffness becomes increasingly important as the tension becomes very low, providing an additional mechanism for the wall force balance. Thus their results cannot capture the importance of the bending effects.

Our limitation lies in the fact that the small strain assumption is maintained during the deformation process (see section 2.5). Since both ends are fixed, this is inevitably not true during the large collapsing process. Our estimation shows about 4% straining for half-channel collapse and as much as 7% during the full collapse. As a check, initially-deformed geometry with longer initial length was tried. These results indicated that converged wall shapes do not change much whether starting from the undeformed or deformed geometry. Both models have limitations but this should not hinder our validation process.

Figures 3.12 and 3.13 show the corresponding result for $Re = 100$. Note that at $\beta = 75$, collapse is seen to be asymmetric. Further increase in β results in greater asymmetry; also, convergence difficulties are seen due to the formation of a steep slope in the wall at the downstream end. Increasing E helps compensate for this effect, but causes the solution to deviate from the tension-dominant limit, and diminishes the asymmetric collapse. The membrane bulging, observed at the upstream end in the membrane simulations for large Re [55, 67], was not seen in our simulation. This is consistent with the experiments of Bertram [8, 9, 10] in which bulging was never witnessed. Since Bertram used thick walls,

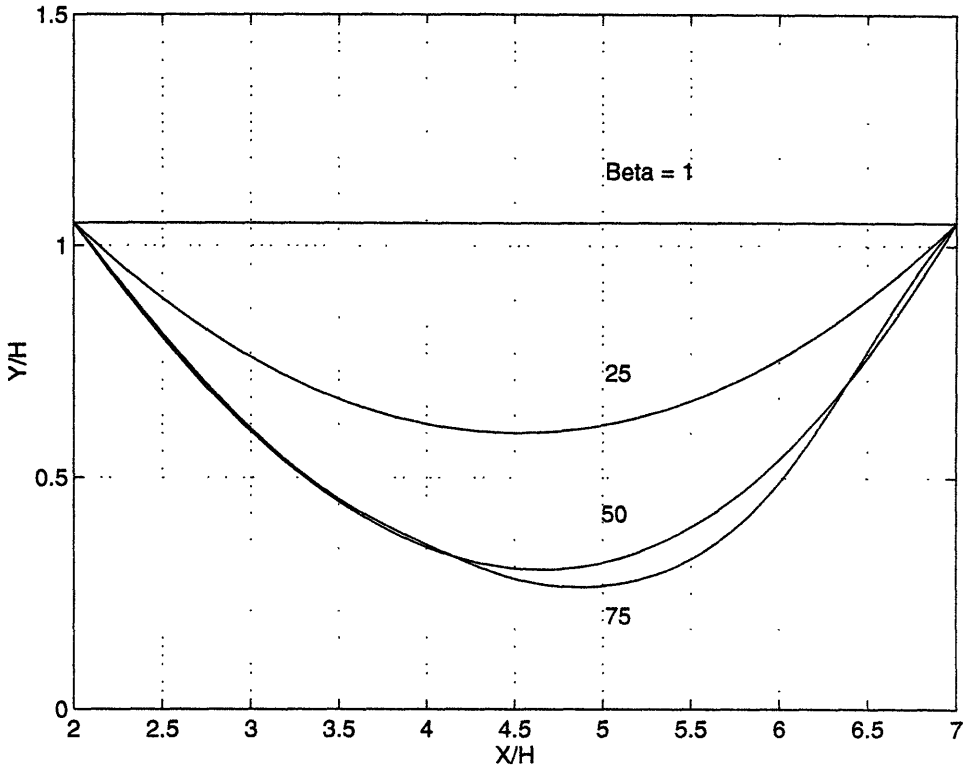

Figure 3.12 The wall shapes obtained from the solid solver for Re = 100 with β = 1, 25, 50, 75.

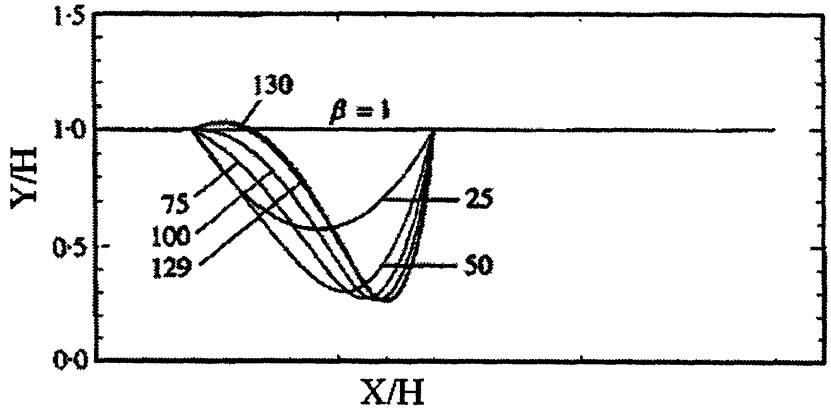

Figure 3.13 The wall shapes obtained from the numerical calculations of Re = 100 and T = T_O/β, where β = 1, 25, 50, 75, 100, 129, 130 (from Luo and Pedley [55]).

the inertia and bending effects may have prevented the tube from bulging out. This suggests that our wall may not be thin enough to capture the bulging effect.

Figures 3.14 and 3.15 shows the converged fluid solution of the case with Re = 100 and $\beta = 75$. The flow speeds up significantly under the region of minimum cross-sectional area and flow separation occurs behind the region of the collapsible segment. The flow appears to be well-developed at the downstream end. Similar behavior was reported by Luo and Pedley [55].

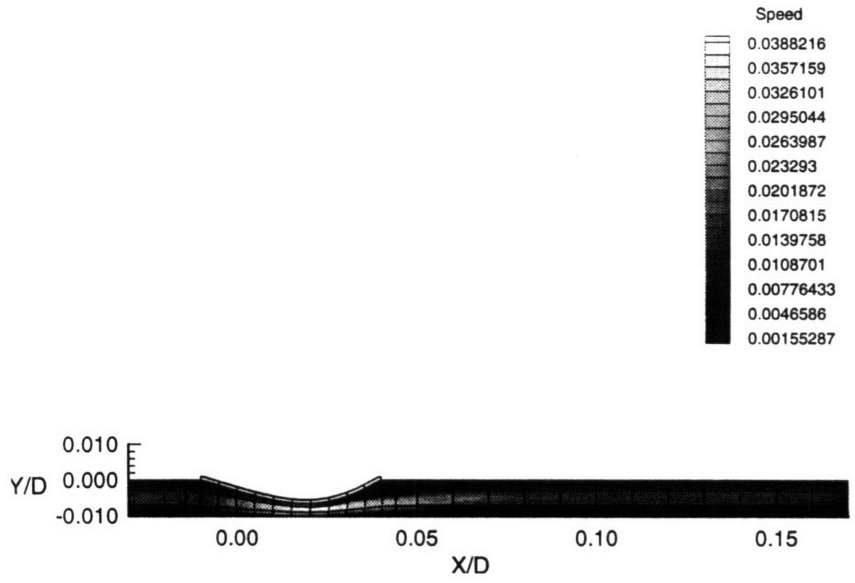

Figure 3.14 The speed contours and the wall shape for Re = 100 and $\beta = 75$.

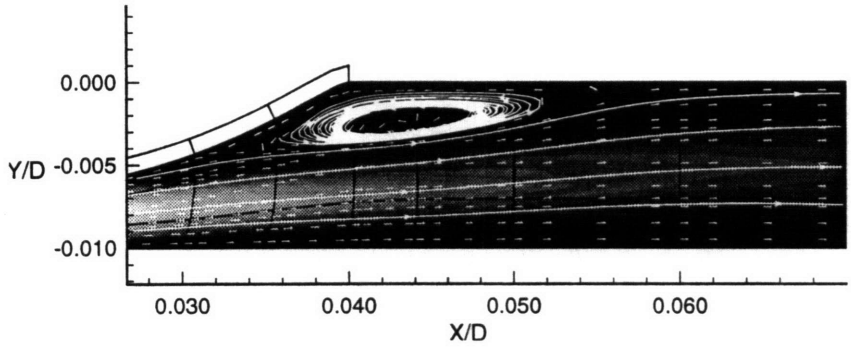

Figure 3.15 The speed contours with velocity vectors and streamlines for Re = 100 and $\beta = 75$.

3.2.7 Tensioned Web Boundary Condition

It is worth noting here that Ho [41] incorporated new tensioned web boundary conditions into NEKTON to simulate the membrane solutions of Luo and Pedley [55]. The modification was made to the free surface analysis by satisfying the no-slip condition at the interface with initial tension capability. He was able to reproduce all the cases of Re = 1 presented in Figure 3.11. At Re = 100, he obtained stable solutions for cases that Luo and Pedley were not able to run. Figure 3.16 shows the result obtained with tensioned web option in NEKTON. $\beta = 300$ was used for the simulation, and it appears lowering the membrane tension cannot completely shut down the collapsible channel. The singularity associated with the upstream end was not encountered, and two distinct recirculating zones were formed. These results suggest that the convergence limitations that Luo and Pedley

observed are maybe numerical limitations rather than physical ones. More cases must be examined to solidify this claim.

Figure 3.16 The tensioned web simulation using NEKTON with Re = 100 and $\beta = 300$ (from Ho [41]).

3.2.8 The Effect of Young's Modulus and Reynolds Number

Numerical experimentation has shown that increasing E or Re result in stabilization of the wall deflection. Figure 3.17 shows the effect of raising Re while other conditions remained fixed. We can see that the point of maximum collapse does shift as Re increases and more asymmetric collapse occurs. This is also observed in the results of Luo and Pedley. Figure 3.18 shows the effect of increasing E while other parameters remain fixed. Since higher E implies a stiffer wall, we expect to see less collapse as E is increased. For higher E, more symmetric collapse was witnessed.

In conclusion, the completed solver was successfully interfaced with the existing fluid solver and validation was accomplished by examining solid simulations alone and then verifying the steady fluid-structure interactions problems of Luo and Pedley. We decided to stay with a 2-D channel with a collapsible segment for computational efficiency. With the foundation complete, we can now explore our original goal of understanding flow limitation and flutter.

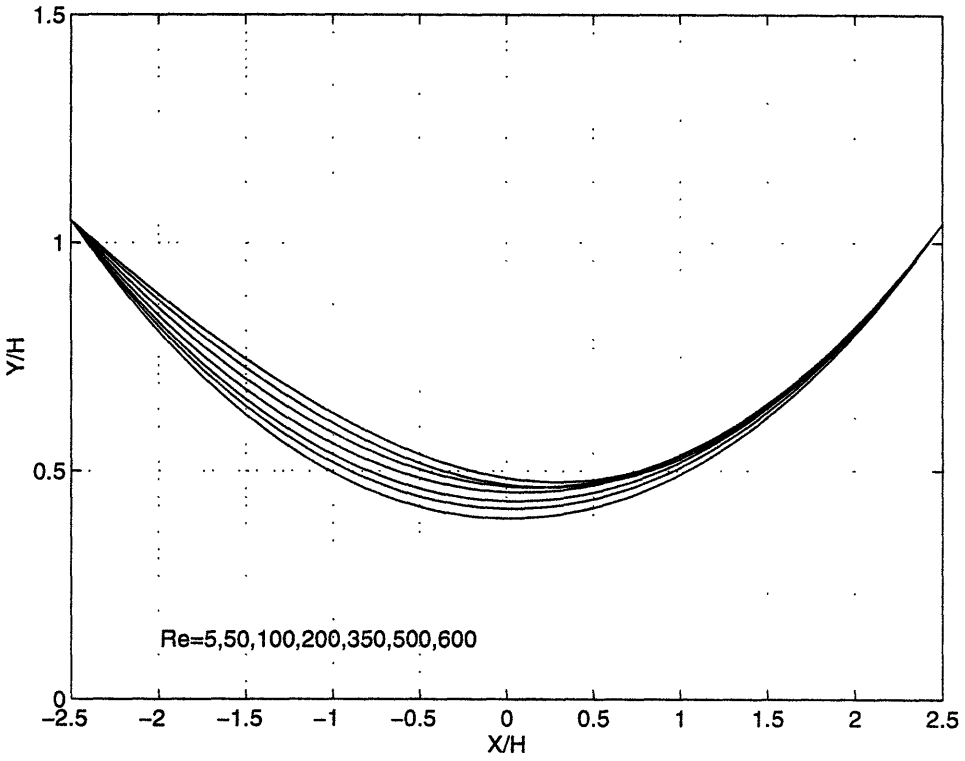

Figure 3.17 The effect of Reynolds number with E = 10, ν = 0.2, and β = 30. The deflection decreases as Re increases.

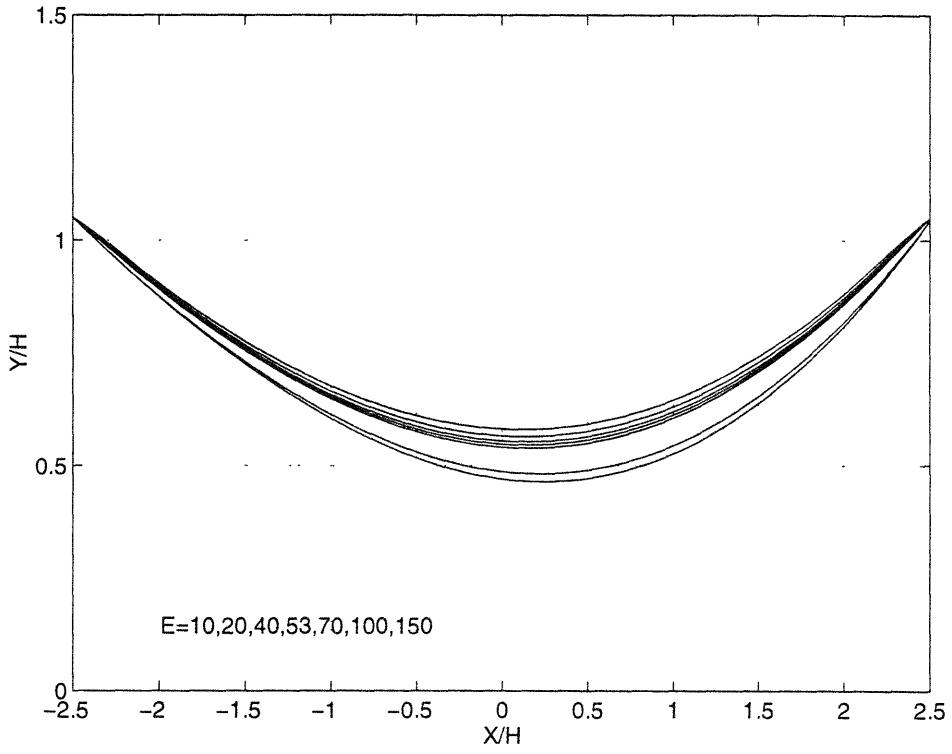

Figure 3.18 The effect of Young's modulus with Re = 500, ν = 0.2, and β = 30. The wall deflection decreases as E increases.

Chapter 4

Steady Simulations

4.1 Flow Limitation

Many laboratory experiments have been conducted to investigate the properties of fluid flow through partially collapsed tubes. A typical setup includes a section of compliant tubing, mounted horizontally between two rigid tubes and sealed within a pressurized chamber. This configuration called, a Starling Resistor, allows for variation of the longitudinal tension, external pressure (P_e), flow rate (Q), and upstream and downstream pressures (P_1, P_2 respectively) to mimic particular physiological situations. In all cases, the behavior shown in Figure 4.1 is witnessed. When the difference between P_e and P_1 (upstream transmural pressure) is held constant, almost a linear increase in Q is witnessed with a increase in the pressure drop (P_1-P_2). Eventually Q becomes limited (reaches a plateau) as the pressure drop P_1-P_2 continues to rise. Clinically, this situation is relevant to forced expiration or venous return [49, 80]. The initial objective of this chapter was to examine flow limitation in the same geometry used by Luo and Pedley with tension-dominant. Later, the case in which bending stiffness dominates will also be considered.

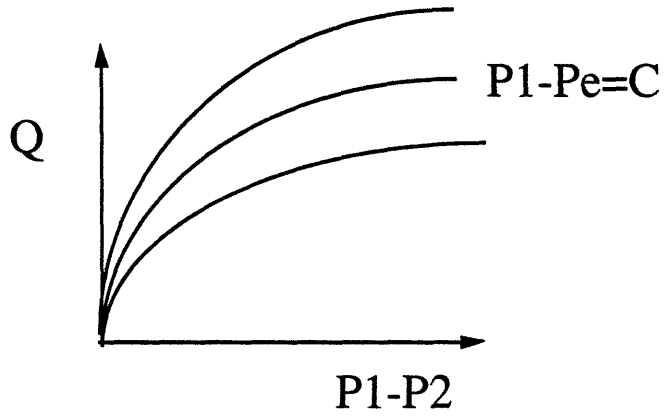

Figure 4.1 The experimental behavior of flow limitation. The flow rate and the pressure drop are monitored while upstream transmural pressure is fixed at a constant value.

4.2 Theoretical Formulation

Because of the complex coupling between fluid and solid, rigorous theoretical solutions are no longer available. For this reason, we will make simplifications to ensure a manageable analysis and also to gain insights into the dominant physical features of the problem. Note that if we analyze the actual elasticity equation instead of the tube law, the wave speed becomes dispersive. This means equation 1.1, the validity of which was already questioned in section 1.1, is no longer valid. Wave speed now depends on the wavelength, and therefore precise wave speed for flow limitation cannot be determined. In this section, the dispersive relation based on the plate equation will be analyzed to examine flow limitation in the 2-D collapsible channel. The assumptions and limitations are detailed below.

4.2.1 Wave Speed Limitation:

The dispersion relation for area waves due to longitudinal bending and tension is developed for 2-D channel flow. Establishing the theoretical foundation of flow limitation, we can make quantitative comparisons with the observed numerical solutions. We will follow an analysis similar to that of McClurken et al. [59]. The major difference is that we are not dealing with the tube law; instead, the coupling of the two domains is represented by the simple plate equation, which takes into account the effects of both axial bending and tension.

We start from the simple equations that govern the actual fluid-structure interactions. The simplified plate equation is:

$$P - P_e \equiv -T\frac{\partial^2 y}{\partial x^2} + EI\frac{\partial^4 y}{\partial x^4} \tag{4.1}$$

where $I = \frac{h^3}{12(1-\nu^2)}$ is the moment of inertia. With the small displacement assumption, we can assume that tension T is given by $T = T_{initial} + \varepsilon_{xx} Eh$. In reality, T varies along the wall because of skin friction. Since the variation is small, we assume that T is constant in the analysis. Note that nonlinear components of tension and bending are ignored. Furthermore, the assumption is that the two effects act independently. This equation shows that the transmural pressures are opposed by the above two components. Equation 4.1 is a good representation of the wall for small deformations.

The 1-D continuity and inviscid momentum equations are given by:

$$\frac{\partial y}{\partial t} + \frac{\partial}{\partial x}(uy) = 0 \tag{4.2}$$

$$\frac{\partial u}{\partial t}+u\frac{\partial u}{\partial x}+\frac{1}{\rho}\frac{\partial P}{\partial x}=0 \tag{4.3}$$

First we nondimensionalize above equations with following parameters.

$$\eta=\frac{y}{y_o},\quad \xi=\frac{x}{y_o},\quad \tau=\frac{tC_o}{y_o},\quad C_o=\sqrt{\frac{E}{\rho}},\quad S=\frac{u}{C_o},\quad \psi=\frac{P-P_e}{E}$$

where y_o represents the channel height in the original undeformed geometry.

Equations 4.1-4.3 can be rewritten as:

$$\psi=-\frac{T}{Ey_o}\frac{\partial^2\eta}{\partial\xi^2}+\frac{I}{y_o^3}\frac{\partial^4\eta}{\partial\xi^4} \tag{4.4}$$

$$\frac{\partial\eta}{\partial\tau}+S\frac{\partial\eta}{\partial\xi}+\eta\frac{\partial S}{\partial\xi}=0 \tag{4.5}$$

$$\frac{\partial S}{\partial\tau}+S\frac{\partial S}{\partial\xi}+\frac{E}{\rho C_o^2}\frac{\partial\psi}{\partial\xi}=0 \tag{4.6}$$

Combining equations 4.4 and 4.6 gives:

$$\frac{\partial S}{\partial\tau}+S\frac{\partial S}{\partial\xi}+\frac{EI}{\rho C_o^2 y_o^3}\frac{\partial^5\eta}{\partial\xi^5}-\frac{T}{\rho C_o^2 y_o}\frac{\partial^3\eta}{\partial\xi^3}=0 \tag{4.7}$$

With the assumption that all dependent variable can be represented by a constant term and a small disturbance term, we can perform linearized analysis. The result gives information concerning wave propagation in the system.

Letting $\eta=\overline{\eta}+\eta'(\xi,\tau)$ *and* $S=\overline{S}+S'(\xi,\tau)$ into equations 4.5 and 4.7, we have

$$\frac{\partial S'}{\partial \tau}+\bar{S}\frac{\partial S'}{\partial \xi}+\frac{EI}{\rho C_o^2 y_o^3}\frac{\partial^5 \eta'}{\partial \xi^5}-\frac{T}{\rho C_o^2 y_o}\frac{\partial^3 \eta'}{\partial \xi^3}=0 \tag{4.8}$$

$$\frac{\partial \eta'}{\partial \tau}+\bar{S}\frac{\partial \eta'}{\partial \xi}+\bar{\eta}\frac{\partial S'}{\partial \xi}=0 \tag{4.9}$$

Note that only terms of first order in the primed quantities and their derivatives are retained; higher-order terms are discarded. Differentiating and combining above two equations gives:

$$\eta'_{\tau\tau}+2\bar{S}\eta'_{\xi\tau}+\bar{S}^2\eta'_{\xi\xi}+\frac{T}{\rho C_o^2 y_o}\bar{\eta}\eta'_{\xi\xi\xi\xi}-\frac{EI}{\rho C_o^2 y_o^3}\bar{\eta}\eta'_{\xi\xi\xi\xi\xi\xi}=0 \tag{4.10}$$

In order to investigate wavelike behavior, consider the elementary wavelike solutions given by setting $\eta'=\hat{\eta}e^{[i(wt-kx)]}=\hat{\eta}e^{\left[i\left(\frac{wy_o}{C_o}\tau-ky_o\xi\right)\right]}$ where $\hat{\eta}$ is a real amplitude; w is real and equal to the circular frequency; k is the complex wave number. For inviscid flow, we know that k should be purely real. Note that $k=\frac{2\pi}{\lambda}$, $c=\frac{w}{k}$ (λ is the wavelength and c is the phase speed). The inviscid dispersion relation can be obtained by setting $S=0$ and relating phase velocity to wavelength. The resulting equation is:

$$\begin{aligned} c^2 &= \frac{4Eh^3 y_o \pi^4}{3(1-\nu^2)\rho\lambda^4}\bar{\eta}+\frac{4\pi^2 T y_o}{\rho\lambda^2}\bar{\eta} \\ &= c_B^2+c_T^2 \end{aligned} \tag{4.11}$$

Above equation shows that the phase speed is composed of two parts: one is due to axial tension and the second results from the axial bending stiffness. Letting γ represent the relative importance of the two terms, we obtain

$$\gamma = \left(\frac{c_T}{c_B}\right)^2 = \frac{3T(1-\nu^2)\lambda^2}{Eh^3\pi^2} \tag{4.12}$$

Now consider the potential for flow limitation. Based on the wave speed flow limitation theory, for non-dispersive systems, we might expect flow in this dispersive system to behave similarly. In that case, two limits can be considered based on γ. If tension dominates ($\gamma >> 1$) the maximal flow rate is determined by:

$$Q_{\max} \cong yc_T \cong \frac{2\pi}{\lambda} y^{\frac{3}{2}} \left(\frac{T}{\rho}\right)^{\frac{1}{2}} \tag{4.13}$$

If bending dominates, ($\gamma << 1$) holds, and

$$Q_{\max} \cong yc_B \cong \frac{2\pi^2}{\lambda^2} y^{\frac{3}{2}} \left(\frac{Eh^3}{3(1-\nu^2)\rho}\right)^{\frac{1}{2}} \tag{4.14}$$

With the above analysis, we now can determine whether flow limitation can be established in a two-dimensional channel with a compliant segment.

4.3 Results and Discussion

With the above theoretical foundation, an attempt was made to examine whether flow limitation in a 2-D channel or any system dominated by axial bending or tension, is indeed due to wave speed limitation. Two extreme scenarios were examined to isolate each contribution.

4.3.1 Tension-Dominant Case

Figure 4.2 shows the computational domain used for the simulation. Total of 91 elements and 5th order interpolants were used for these simulations The parameters are essentially the same as those of Luo and Pedley with some modifications.

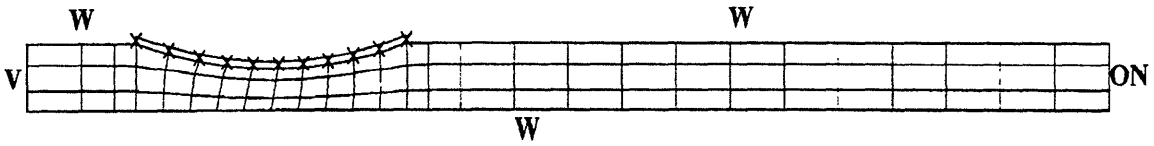

Figure 4.2 The computational domain used for tension-dominant simulations.

Compared to the original Luo and Pedley geometry, the downstream length is increased further to ensure that outflow normal (ON) condition will not contaminate the solution in the vicinity of the complaint segment. The key parameter to be controlled is P_1 (actually $P_1 - P_e$), which can be difficult to control if the velocity profile is specified at the inlet. One way to overcome this dilemma is by noting that for variational methods, pressure is determined up to the constant value. Numerically, this means that pressure is the Lagrange multiplier of the resulting equilibrium equation. Furthermore, the final steady solution is irrelevant to the solution path taken. With these facts, we can simulate a parabolic profile at the inlet and ON at the exit. Once P_1 is obtained, we can scale the whole fluid domain by ΔP to keep P_1-P_e at the constant value as desired. Hence we are effectively adjusting the downstream pressure P_2 to maintain upstream transmural pressure constant while the simulations are carried out. As a consequence, different transmural

pressure acts on the solid and further iterations are required between the two domains to determine the equilibrium solution. Note that P_1 is the average pressure in the fluid domain at the beginning of the collapsible region and P_2 is similarly at the downstream of the collapsible region. These locations are monitored in accordance with the actual experimental setting.

In addition to parameters listed in Table 3.3, solid parameters used in the tension-dominant simulations are listed in Table 4.1. The thickness of the solid again is the post-stretched length. The tension-dominant requirement (see equation 4.12) is easily satisfied with these parameter values . Figure 4.3 shows the typical flow limitation simulations (referred to as standard cases). The results are shown for three different values of $P_1 - P_e$ (ΔP). In all cases, restart was done from the solution of lower Re and continued until it was no longer possible to obtain a converged solution. Typically 7 to 10 runs were obtained before convergence failed The task is to examine the theoretically predicted flow rates from the dispersive analysis above with what is observed in the numerical simulations.

Initial Tension	T = 50 N/m
Young's Modulus	E = 20 Pa
Poisson's Ratio	ν = 0.2

Table 4.1 The additional solid parameters in conjunction with Table 3.3 used in the tension-dominant simulations.

Note that in equation 4.13, the wavelength (λ) must be specified. The exact value of λ cannot be exactly known and as a first approximation, we assumed that it is roughly same as L, which is the total length of the collapsible region. Note that by setting $\lambda = L$,

the longest wave that can exist in this channel, we are insuring that waves of all possible lengths can propagate upstream since shorter waves travel faster. Table 4.2 shows the theoretical predictions compared with the numerical results. Note that last four cases were performed with $\Delta P = 0$ Pa and one variable in the equation 4.13 was varied while other parameters remained the same compared to standard cases.

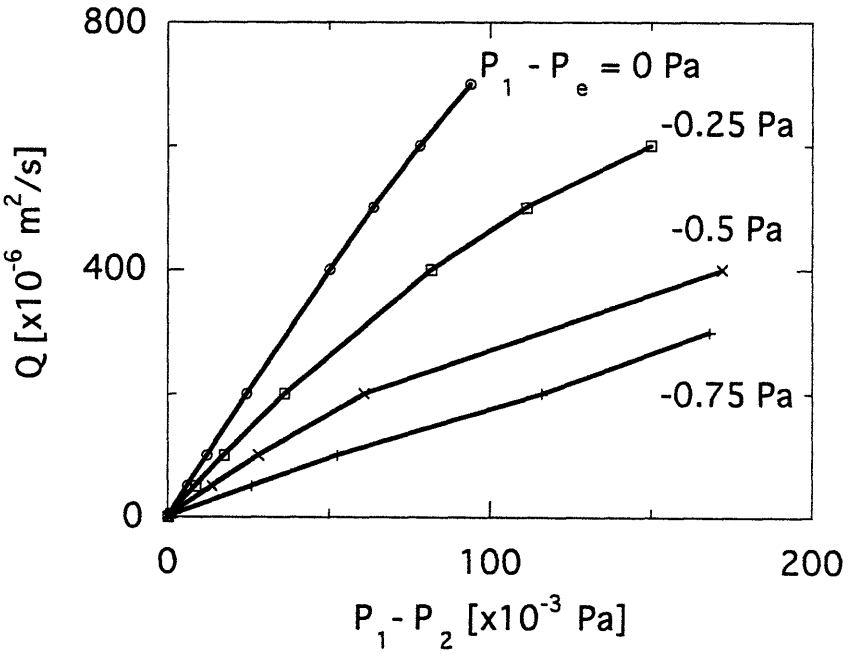

Figure 4.3. The flow limitation simulations for the standard cases.

	Qnum (x 10^{-4} m^3/s)	Qtheor (x 10^{-4} m^3/s)
Standard Δp = 0.0 Pa	7.0	8.5
Δp = -0.25 Pa	6.0	5.5
Δp = -0.50 Pa	4.0	4.1
Δp = -0.75 Pa	3.0	2.7
ρ x 2 = 2000 kg/m^3	6.5	6.0
T/2 = 0.025 N/m	6.0	5.4
L x 2 = 0.05 m	3.5	4.4
μ x 30 = 0.03 kg/m*s	2.0	2.7

Table 4.2 The comparison between predicted and observed flow rates.

Figure 4.4 shows the wall shapes for the case with ΔP = -0.5 Pa. A continuous decrease in channel height was seen as Re was increased. The point of maximal collapse moved downstream creating an increase in the degree of asymmetry during this process. This result is similar in nature to Figure 3.17. Note that there exists a difference in boundary conditions applied that accounts for the difference in behavior. Figure 4.5 shows the pressure contours in the collapsed region. Note that the legend indicates the pressure values before the actual adjustments. In the actual simulation, the pressure at the beginning of the collapsible region is adjusted to maintain a constant ΔP with respect to the external pressure. This means that all pressures must be scaled by this amount. Figure 4.5 also indicates that at each cross-section, pressure maintains almost a constant value. Figure 4.6

shows the corresponding speed contours. The flow increases significantly under the collapse region; flow separation was not present for this particular case.

In conclusion, the comparison of Table 4.2 suggests that the Q computed from the numerical analysis is in good agreement with the Q predicted from the dispersion analysis for $\lambda = L$. We expected to see an order of magnitude match, but the agreement was much better than this. This suggests that flow is indeed wave speed limited. The other extreme (bending-dominant case) must now be examined.

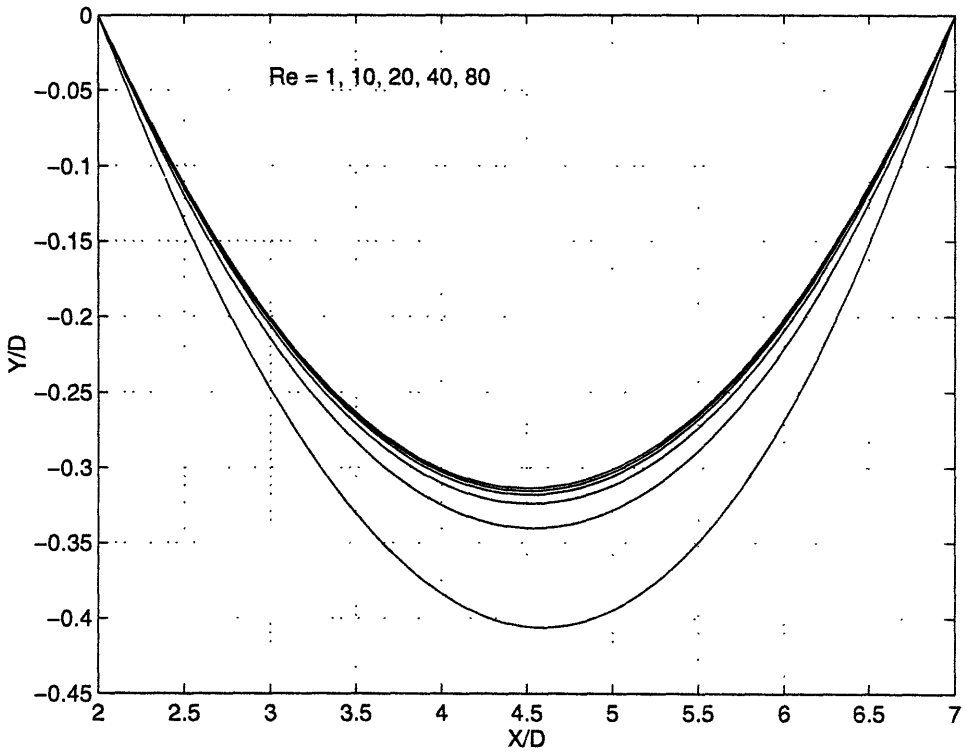

Figure 4.4 The wall shapes of the tension-dominant simulations for ΔP = -0.50 Pa with Re = 5, 50, 100, 200, and 400.

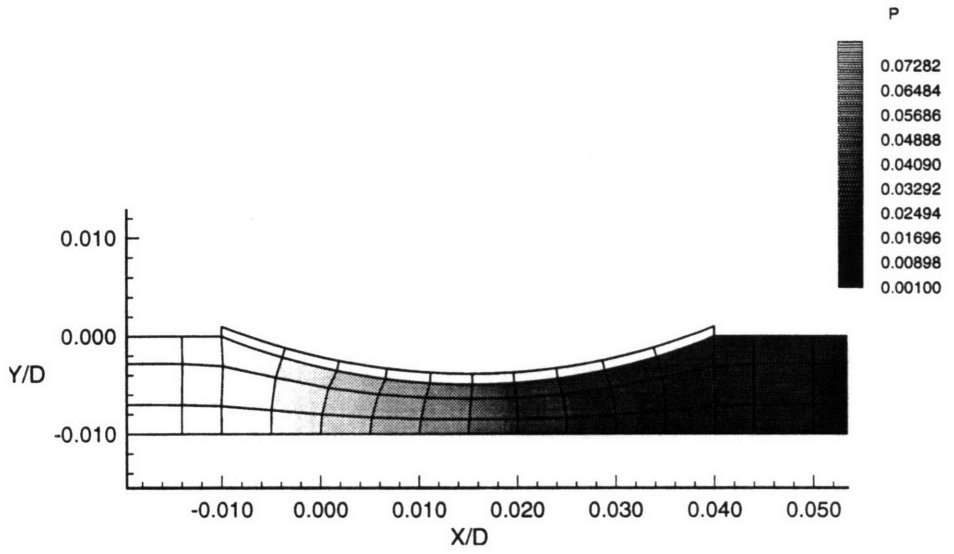

Figure 4.5 The pressure contours for the tension-dominant simulation case with Re = 100 and ΔP = -0.50 Pa.

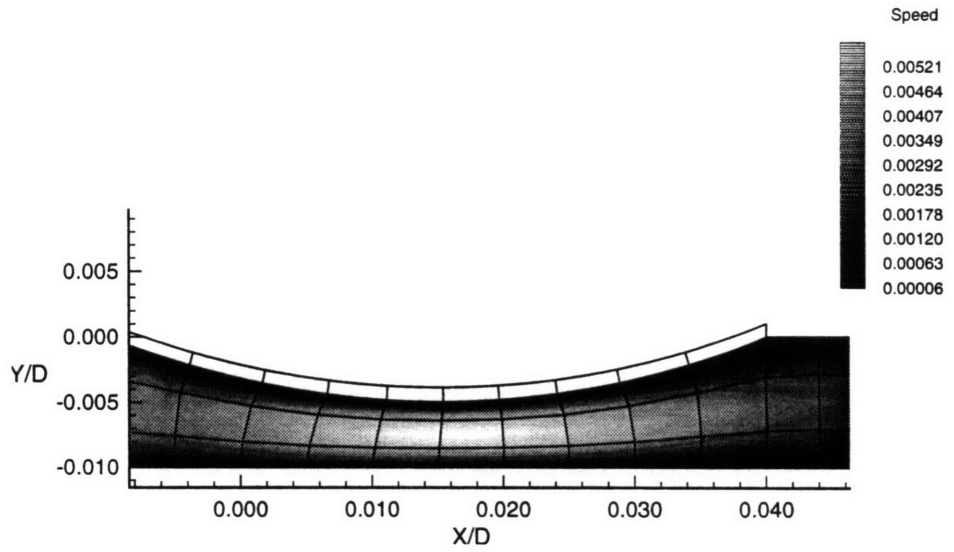

Figure 4.6 The speed contours for the tension-dominant simulation case with Re = 100 and ΔP = -0.50 Pa.

4.3.2 Bending-Dominant Case

For the bending-dominant case, the computational domain was modified (as shown in Figure 4.4) by the addition of solid elements downstream. Additional elements increased the number of elements to 97. These elements were allowed to slide horizontally to minimize the axial tension buildup during the deflection process. This modification therefore ensured that deflection is resisted purely by bending effects alone. For left end, the boundary condition remained to be fixed. In order to satisfy bending dominance (equation 4.12), the initial tension was set to zero for these simulations. Boundary conditions were otherwise unchanged from the tension-dominant case (Figure 4.2).

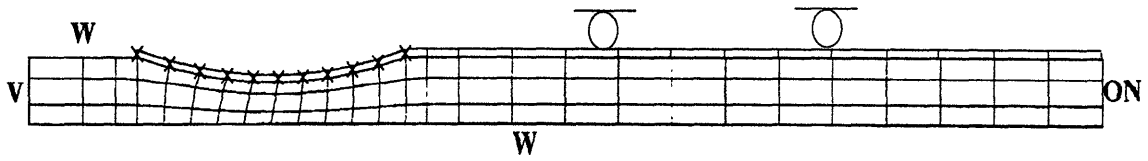

Figure 4.7 The computational domain used for bending-dominant simulations.

Figure 4.8 shows the results of flow rate (Q) plotted against the pressure drop (P_1 - P_2) for four different values of E. The solid lines on the figure indicate the predicted Q based on equation 4.14. Note that these predictions were calculated with the undeformed width (y_0). Interesting phenomena were witnessed as Q was increased in the system. For low values of Q, the deflections were minimal and a linear relationship between Q and P_1 - P_2 was witnessed irrespective of the values of E. This is why all four curves lie on top of one another initially. Once predicted Qs were reached, the walls started to deflect

noticeably from the undeformed geometry-causing additional pressure drop while Q increased only slightly. This occurrence was witnessed for all four values of Young's modulus and is shown in Figure 4.9. Note the slopes at the ends are different compared to the tension-dominant cases (see Figure 4.4). Since the wall is allowed to slide, the collapse is dominated by bending effects, not axial tension. Therefore, symmetric collapse was maintained. Speed contours with velocity vectors are shown for a typical case in Figure 4.10. Since Re = 1750, the velocity profile is very blunt characterized by a sharp drop in velocity magnitude from the core to the wall. Flow separation was not seen in these cases even though the Re is relatively high. This finding suggests that sharp corners present in the tension-dominated cases but not when bending dominates, is responsible for flow separation.

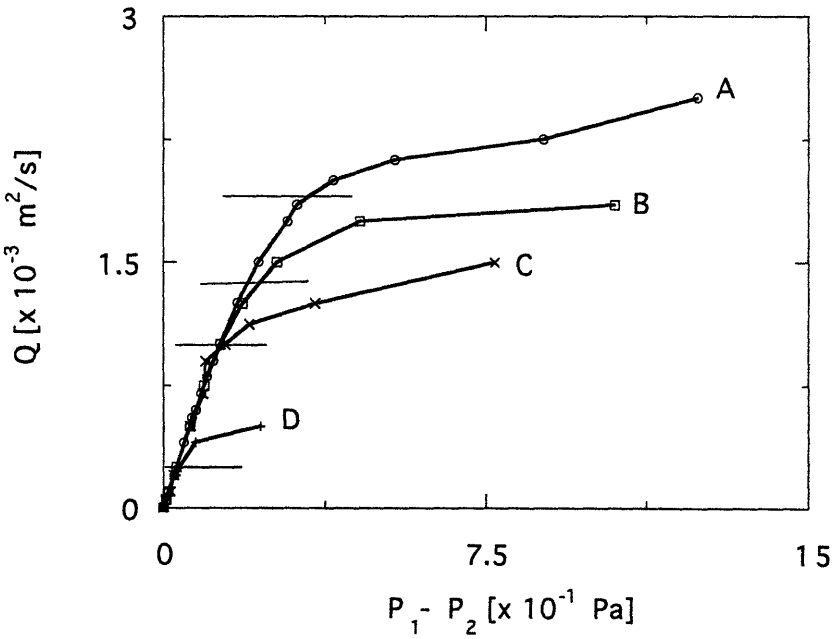

Figure 4.8 The bending-dominant results for A) E = 2 x 10^5 Pa, B) 1 x 10^5 Pa, C) 5 x 10^4 Pa, and D) 5 x 10^3 Pa with $P_1 - P_e = 0$ Pa.

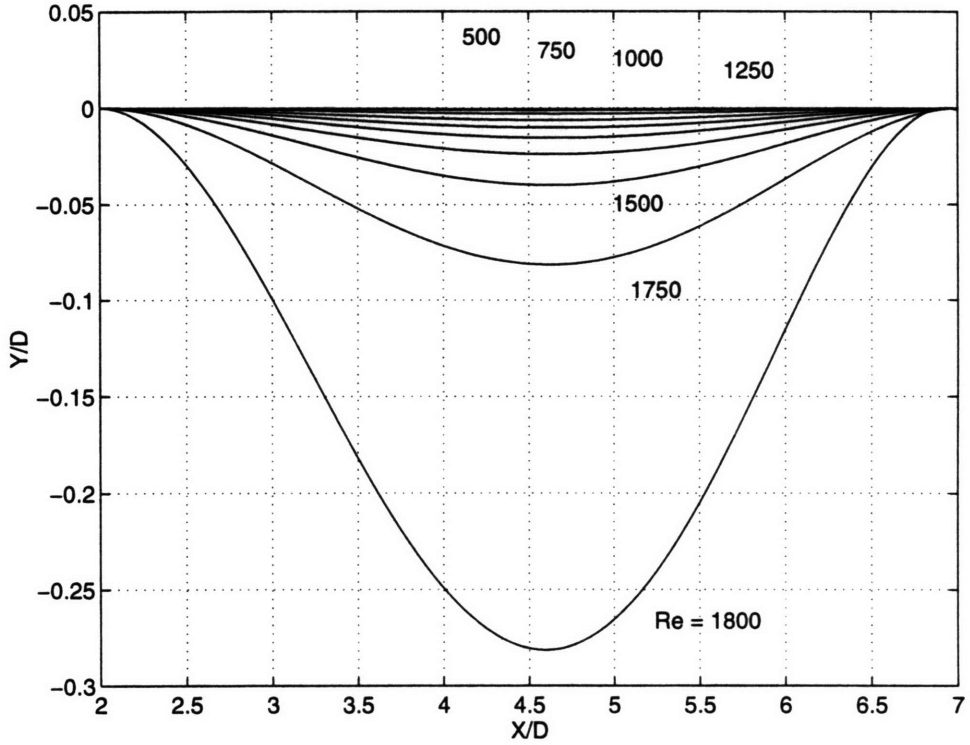

Figure 4.9 The wall shapes of bending-dominant simulations with E = 1 x 10^5 Pa and P_1 - P_e = 0 Pa .

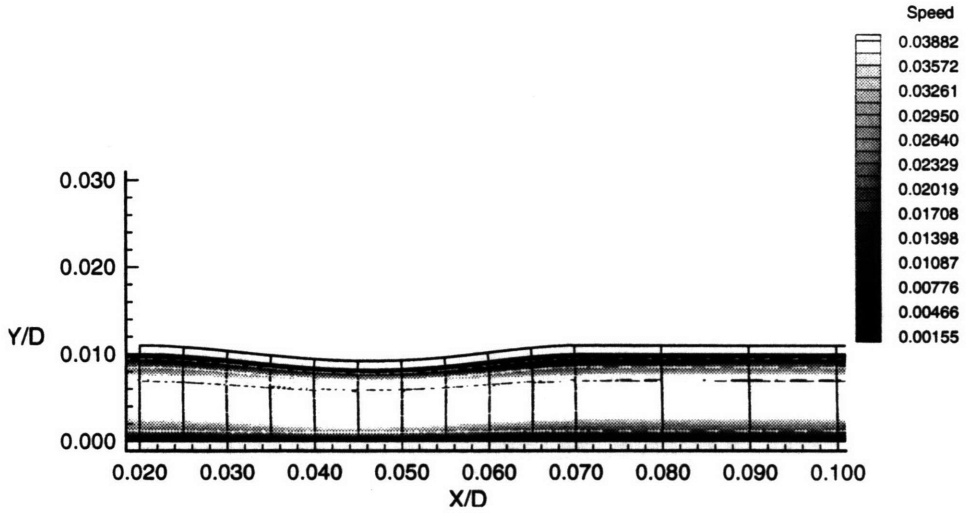

Figure 4.10 The speed contours with velocity vectors for the bending-dominant simulation with Re = 1750, E = 1 x 10^5 Pa and P_1 - P_e = 0 Pa .

As in tension-dominant cases, the theoretically predicted flow limiting values matched the computational simulation reasonably well. This further supports the fact that our prediction, which is still highly simplified, works well once we take the wavelength to be the length of the collapsible region for 2D collapsible channels.

4.3.3 Breakdown of the Numerical Solution

During these simulations, three types of solution breakdown were witnessed. The first type was characterized by a gradually increasing wall deflection that never satisfied the convergence criterion. Eventually, the deflection was no longer numerically feasible (due to extreme distortion of solid meshes or because it caused extreme distortion of the fluid meshes) and the run terminated. The second type of breakdown was characterized by significant convergence with the first few steps followed by a period in which the error remained nearly constant so that the tolerance criterion was never reached. The third type was similar to the second case, but a distinct "jump" to new deflection shape was witnessed. Often times, this jump involved "touching" the other side of the wall, causing incompatibility of the two domains.

In all of the steady runs, the simulations were carried out until no converged solutions were found. This procedure required much fine-tuning as the convergence difficulties became more prevalent at higher Q. At this point, it is difficult to conclude whether solution breakdowns are physical or numerical. It is naive to infer physical breakdown from the failure of a converged solution. Furthermore, the existence of the converged solutions does not imply that they can be observed in reality (i.e. the solutions may be dynamically unstable). In all cases, unsteady (time-dependent) runs are required to examine the instability associated with the flow through collapsible channels. Only by allowing for this capability, can we examine instabilities and possibly understand flutter. This is the subject of the next chapter.

Chapter 5

Unsteady Simulations

Figure 5.1 shows the steps involved in unsteady fluid-structure simulations. The key difference, compared to steady simulations, is the presence of two distinct loops: (1) An inner loop that ensures the convergence between two domains at every particular time step; (2) An outer loop that exists to march in time. As stated before, the dynamic analysis is basically a static analysis with inertia at each particular time step (see section 2.3). For the inner loop, the same convergence criterion was used as in the steady simulations.

In reality, the effect of the inner loop was minimal. This is because of the fact that if the time step is small enough, the corresponding displacements are small and the inner loop is exited without further alternating between two domains (see section 3.2.2). It only affects the cases that are unstable. In these cases, the inner loop minimizes the incompatibility between two domains. If successful, solutions of questionable accuracy maybe obtained (by reaching the maximum iteration counter), but often the loop cannot overcome inherent instabilities.

The solid velocity components, instead of displacements, must be extracted at the interface to ensure no-slip boundary conditions of the fluid domain. This is a crucial difference compared to the steady simulations. Once extracted, the velocity components must be integrated using the ALE method to give the proper mesh update for the fluid

domain . This step ensures that no gaps or overlapping of the two domains occur at the interface. The fluid domain is solved just as in any other moving boundary problem.

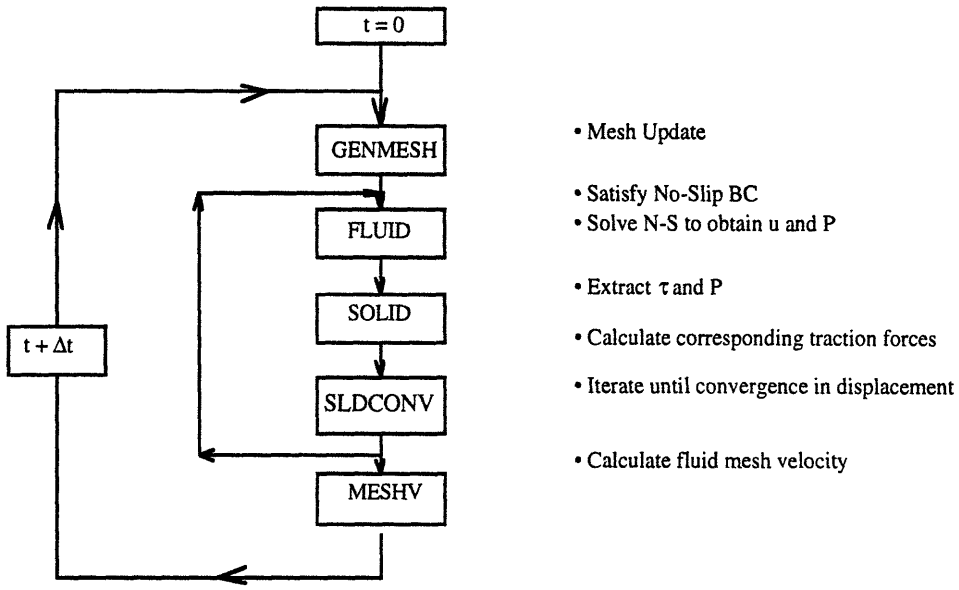

Figure 5.1 The computational steps involved in unsteady fluid-structure interaction simulations. An inner loop ensures the compatibility of two domains at a particular time, and an outer loop exists to march in time.

Verification was difficult due to the fact that no similar comparison cases can be found either from experiment or numerical analysis. Luo and Pedley [56] were able to run unsteady cases with their membrane under tension, but the wall inertia was completely absent from their simulations. Wall inertia plays an important role during unsteady motion, and therefore direct comparison was not possible. Furthermore, Luo and Pedley abandoned the segregated approach for the unsteady simulations and constructed a coupled coefficient matrix instead. This made comparison practically impossible. Unlike the steady simulations, their results did not lend any insight to our numerical strategy.

During the initial stage of numerical experimentation, great difficulties were encountered in any feasible fluid-structure interaction situations. The instability was characterized by the buildup of pressure forces (i.e. vertical traction force) that eventually caused the solid solver to crash. A reduction in time step alone did not stabilize the system. The instability was more dependent on the number of iterations between the two domains than on time step size. In an effort to minimize the sudden increase in the traction forces, the ramping technique was tried for velocity inlet condition. This method only delayed the inevitable instability. Without a clear verification case, a more systematic approach to unsteady runs was required.

5.1 Passive Fluid

We turned our attention to the simplest case possible with known behavior. Figure 5.2 shows the test case which consists of the solid domain with given initial velocity interacting with the fluid domain that is at rest initially. We refer to this situation as a "passive fluid" since the solid motion gives rise to the fluid motion. This can be distinguished from an "active fluid" in which the fluid motion excites the wall motion. The test case is equivalent to a vibrating solid submerged in a fluid. We expect a decay of solid displacements since the fluid is "passive", implying that the fluid acts to damp the solid motion. This means that developed shear stresses from the fluid domain oppose the motion of the solid and eventually cause it to die out completely.

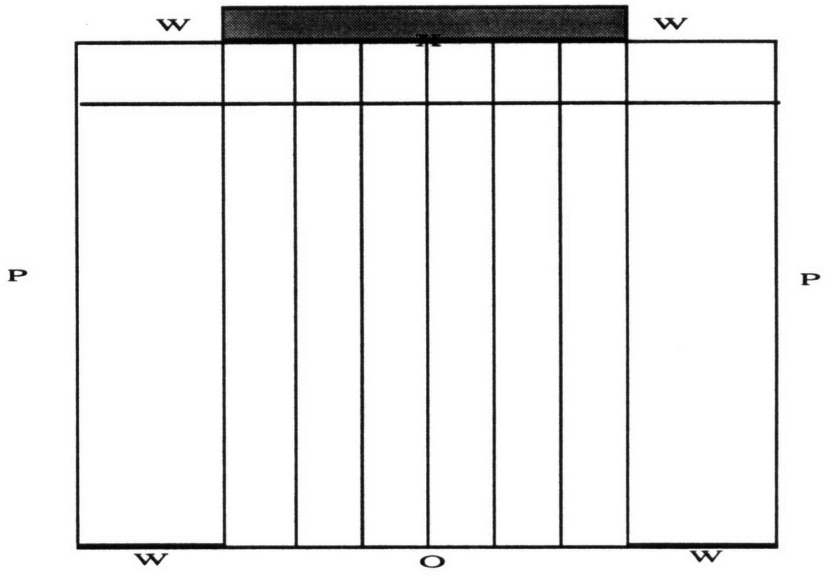

Figure 5.2 The computational domain used to simulate passive fluid simulations. This case is equivalent to a vibrating solid submerged in a fluid that is at rest initially.

For the solid, fixed boundary conditions were used at both ends. The initial solid velocity is defined with a maximum amplitude of one at the center of the solid that falls parabolically to zero at both ends. For the fluid domain, periodic boundary conditions at the two sides were specified, while the bottom center allowed outflow. This was required to overcome the incompressibility requirement of the fluid. The parameter values used in the simulation are listed in Table 5.1. Note that no units were specified for the values since this was a generic test case. Any consistent set of units can be used to represent these parameters.

Fluid domain height	H = 12
Fluid domain width	W = 10
Solid length	L = 8
Solid thickness	h = 1
Fluid viscosity	$\mu = 5$
Fluid density	$\rho_f = 0.01$
Solid Density	$\rho_s = 10.0$
Young's Modulus	E = 200,000
Poisson's ratio	$\nu = 0.2$
Time step	$\Delta t = 0.005$

Table 5.1 The parameter values used to simulate fluid-structure interactions with a passive fluid.

The results are shown in Figure 5.3. The location monitored is the center line interface point of the two domains; results are presented for the deflection of the solid and the vertical velocity component of the fluid. The plot clearly shows that the motion of the solid decays due to fluid damping. Typically, only one or two equilibrium iterations were required for the solid, and the results were the same with or without the inner loop. For fluid velocity, a slight instability was witnessed but quickly disappeared due to the damping effect. When the fluid viscosity was increased, the decay rate was much faster since the damping effect is greater in this situation.

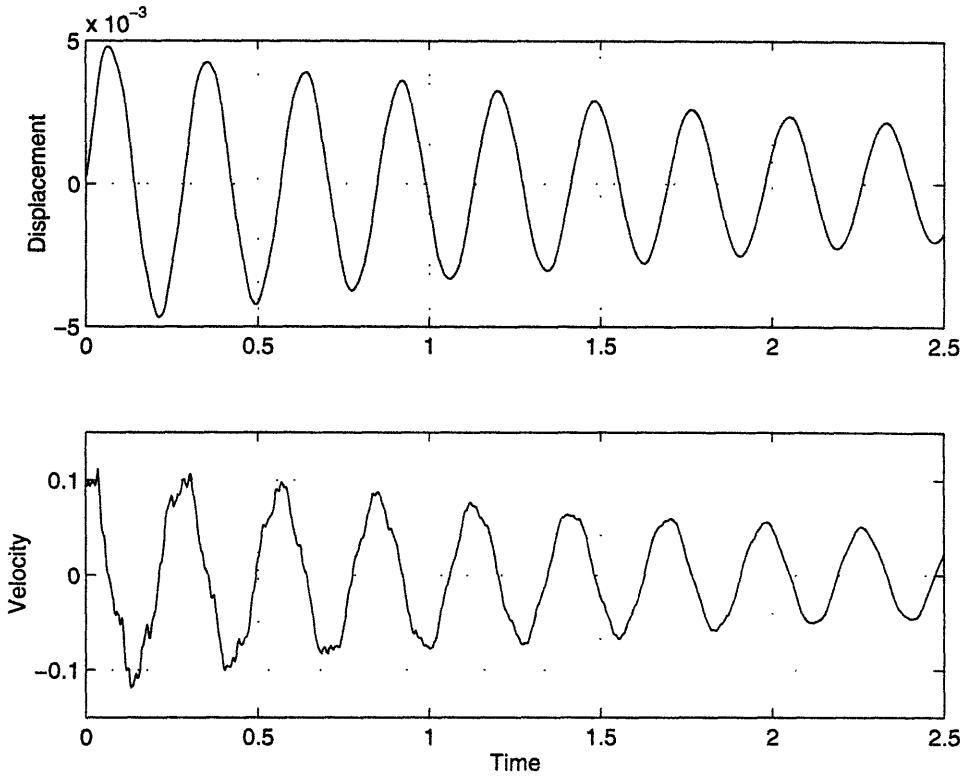

Figure 5.3 The simulation of a solid with a passive fluid. a) The vertical deflection of the solid at the centerline interface. b) The vertical component of the fluid velocity at the centerline interface.

As explained in section 1.3, many passive fluid type (Category (C)) simulations exist in the literature. Despite this, our attempts to locate a comparable case were unsuccessful since most simulations were limited to acoustic or mode analysis. Among the actual flow simulations, solutions were available for axisymmetric or 3-D cases only. Furthermore, the theoretical prediction of the decay rate was not obtainable. This left us with the empirical approach to the problem at hand.

The effect of the time step was examined. For time steps smaller than the time step used here ($\Delta t = 0.005$), all the runs were stable (but costly) and essentially reproduced the curves shown in Figure 5.3. When $\Delta t = 0.5$ is used, although the solution was stable, a decay in amplitude was not witnessed, indicating that the time step was too large for an

accurate solution. The effect of Young's modulus (E) was examined next. Figure 5.4 shows the wall deflection for three values of E. We know that the vibration frequency of a solid varies as the square root of E. Furthermore, a stiffer wall should result in a smaller deflection. The results show both expected behaviors, providing some degree of confidence in the simulations.

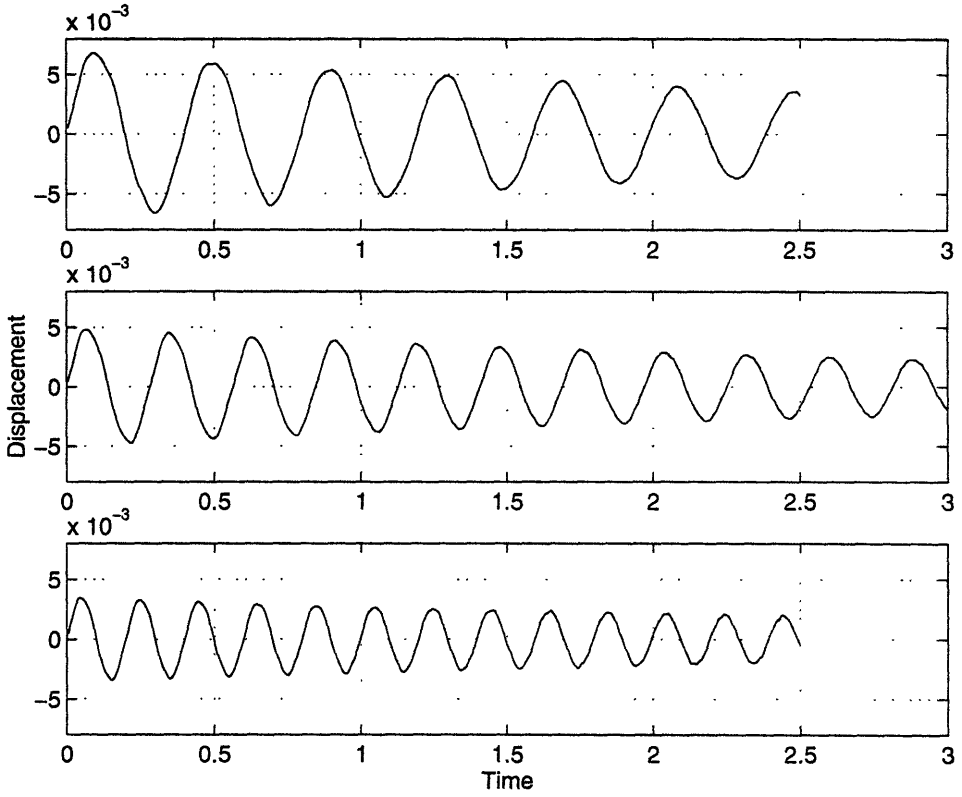

Figure 5.4 The effect of changing Young's modulus on passive fluid simulations. a) $E = 1 \times 10^5$, b) $E = 2 \times 10^5$, c) $E = 4 \times 10^5$.

Defining DR as the ratio between the solid density and the fluid density, note that the above simulations are performed with DR = 1000. This was found to be a critical factor in the ability to perform stable simulations. For this particular situation, DR > 100 was required to run stably. If DR is lowered further, the solution was found to be

unstable. This phenomenon is independent of the time step taken and is discussed further later in this chapter.

Before going further, we want to establish some type of verification for the code before actually examining the unsteady fluid-structure interactions. As stated before, no clear verification can be found in the literature. For this reason, we chose to examine the "added mass" effect that is relevant to the passive fluid situations.

5.2 Added Mass Effect

It is well known both theoretically and experimentally that if the fluid density is much less than the solid density, the effect of a surrounding fluid on the natural frequencies and mode shapes of a structure is not ordinally significant. However, this is no longer true when the densities are comparable. The natural frequency of vibrations in the presence of added fluid mass is lower than that which would be observed in a vacuum; this is an important consideration for marine structures such as ships and pipes which are surrounded by water.

Simple analysis shows that the additional mass of fluid, entrained by a moving structure as it vibrates in a fluid, must be taken into account. The magnitude of this "added mass" is well documented for many simple one- and two-dimensional structures [13]. Using a potential flow analysis, it can be shown that the added mass affects the natural frequency according to:

$$\gamma_{theo} = \frac{f_{fluid}}{f_{vacuum}} = \frac{1}{\left(1+\frac{A}{M}\right)^{\frac{1}{2}}} = \frac{1}{\left(1+\Omega\right)^{\frac{1}{2}}} \tag{5.1}$$

where A is the added mass and M is the mass of the structure. It is important to realize that added mass always decreases the natural frequency of the structure, more so if the densities of two mediums are comparable.

For slender beams, "Strip theory" gives an accurate approximation of added mass [13]. The basic assumptions are: (1) The flow is two-dimensional and inviscid over the beam and (2) the interaction between adjacent strips is negligible. For our test case, this means

$$\Omega = \frac{\rho_f \pi L^2}{4\rho_s Lh} = 2\pi \frac{\rho_f}{\rho_s} \tag{5.2}$$

where ρ_f and ρ_s are fluid density and solid density, respectively.

Figure 5.5 shows the effect of density ratio (DR) on the wall deflection. As DR is reduced, a decrease in both the amplitude and the frequency is clearly seen. Note that for DR = 50, the numerical instability starts to affect the solution as time progresses. Table 5.2 shows a comparison between the numerical result and the theoretical prediction given by equation 5.1. For the vacuum case, the fluid densities were lowered such that DR was about 100,000. Since the fluid viscosity remained the same, a decay in wall deflection was seen. From theoretical prediction, a decrease of about 3% (for DR = 100) and 5% (for DR = 50) are expected. The numerical results indicate that this is well predicted. It is unfortunate that lower density ratio cases, for which we expect to see significant reduction in the natural frequency, were not obtainable. For example, if the densities were identical, we would expect to see 63% reduction in the natural frequency according to equation 5.1. Numerically, lowering DR resulted in a quick failure of the code that was not even able to reproduce a one full period. Nevertheless, this was the useful check to show that the simulation is capable of showing the expected results. Without any verification cases, this test raises the confidence in the accuracy of the unsteady fluid-structure interactions.

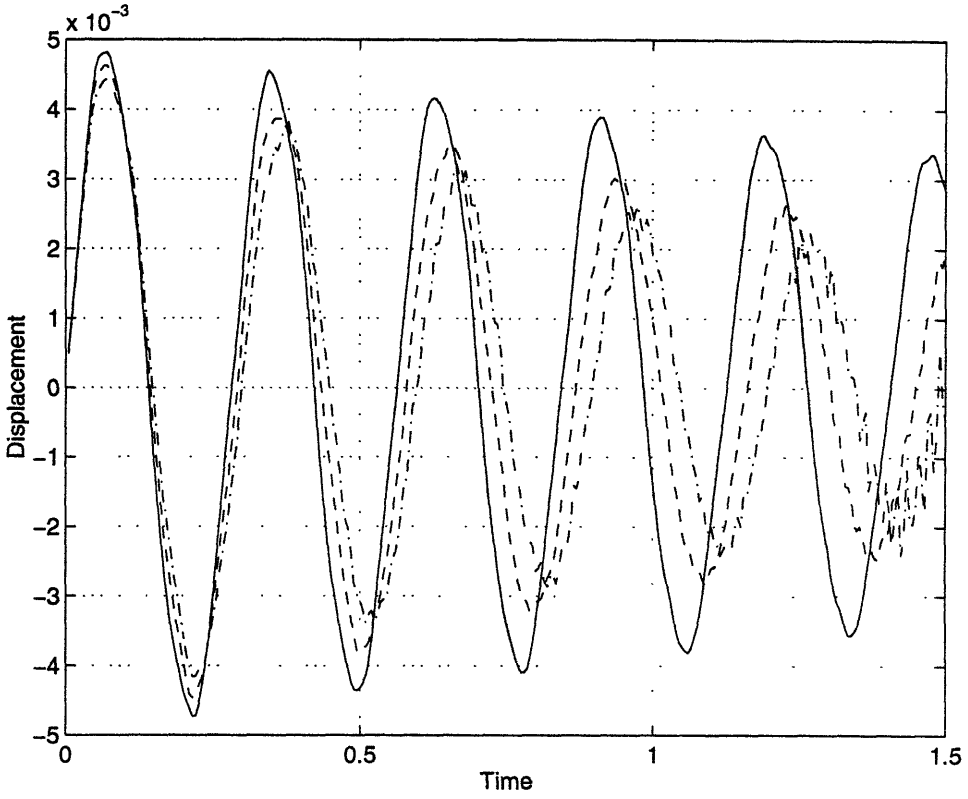

Figure 5.5 The effect of changing DR on wall deflection for passive fluid simulations. a) DR = 1000 (solid), b) DR = 100 (dash), c) DR = 50 (dash-dot).

	f_{num} (Hz)	γ_{num}	γ_{theor}
DR--->Vac	3.534	1.000	1.000
DR = 100	3.42	0.969	0.970
DR = 50	3.33	0.942	0.942

Table 5.2 The effect of added mass on the frequency of passive fluid simulations.

5.3 Rayleigh Damping

Damping is the ability of a structure to absorb vibrational energy. Damping can be generated within the material of the structure (material damping), by the fluid surrounding the structure (fluid damping), or by the impact and scraping at joints (structural damping) [13]. So far in the analysis, damping mechanisms other than fluid damping are completely absent from the analysis. Damping was included in the solid solver to: (1) possibly eliminate the instability that grows at the interface; (2) remove high frequency noise that may contaminate the physical solution.

The existing equilibrium equation can be easily extended to incorporate damping effects, but the problem lies in the determination of the damping matrix. This is because damping properties are frequency dependent. Therefore, it is difficult, if not impossible, to find a general damping matrix. For this reason, the damping matrix C is often constructed using the mass matrix and stiffness matrix:

$$C = \alpha_R M + \beta_R k \tag{5.3}$$

and referred to as Rayleigh damping, where α_R and β_R are constants to be determined from two given damping ratios that correspond to two unequal frequencies of vibration. They represent the energy dissipation characteristic of the materials of interest; experimental results are typically used to determine the amount of damping. In practice, Rayleigh damping will result in considerably more damping out of higher modes than of lower modes. Note that the β_R is equivalent to creating visco-elastic behavior in which the viscosity is proportional to the elasticity. As an initial trial only, the component related to the mass (the first term in equation 5.3) is incorporated into the solid solver.

5.3.1 New Equilibrium Equation

Incorporating Rayleigh damping results in an additional term to the left-hand-side of equilibrium equation given by equation 2.27 such that we are now concerned with

$$M^{t+\Delta t}\ddot{U}^{(k)} + C^{t+\Delta t}\dot{U}^{(k)} + \left({}^{t+\Delta t}K_L + {}^{t+\Delta t}K_{NL}\right)\Delta U^{(k)} = {}^{t+\Delta t}R - {}^{t+\Delta t}F^{(k-1)} \tag{5.4}$$

Expanding this equation using equations 2.26 (for ${}^{t+\Delta t}\dot{U}$) and 5.3, we have

$$\begin{aligned}&\left(Ma_0 + {}^{t+\Delta t}K_L + {}^{t+\Delta t}K_{NL} + Ca_1\right)\Delta U^{(k)} = \\ &{}^{t+\Delta t}R + \left(Ma_2 + Ca_4\right){}^{t}\dot{U} + \left(Ma_3 + Ca_5\right){}^{t}\ddot{U} - \left({}^{t+\Delta t}F^{(k-1)} + \sum_{q=1}^{k-1}\left(Ma_0 + Ca_1\right)\Delta U^{(q)}\right)\end{aligned} \tag{5.5}$$

where $a_0 = \frac{1}{\alpha\Delta t^2}, a_1 = \frac{\delta}{\alpha\Delta t}, a_2 = \frac{1}{\alpha\Delta t}, a_3 = \frac{1}{2\alpha} - 1, a_4 = \frac{\delta}{\alpha} - 1,$ and $a_5 = \frac{\Delta t}{2}\left(\frac{\delta}{\alpha} - 1\right)$. These coefficients again result from the Newmark time marching scheme. The key point to realize is that both sides of equation 5.4 contain additional terms associated with the damping effect compared to equation 2.32. Note that for δ = 1/2 and α = 1/4 (see section 2.3.3) and given Δt, following condition holds: $a_0 >> a_1, a_2 >> a_4, a_3 >> a_5$. Since we are considering the mass contribution of damping only, this means that introducing damping is in some ways equivalent to adding inertia to the solid.

5.3.2 The Effect of Rayleigh Damping

The results are shown for the case of DR = 50 (shown in Figure 5.5) for which the instability sets in as we march in time. Figure 5.6 shows the effect of introducing Rayleigh damping into the simulation. With α_R = 2, the effect of damping is evident. The

amplitude is significantly reduced while the frequency stays the same. In all cases, however, high frequency oscillations grow and cause the solution to go unstable in each case at a time somewhat greater than 1.5 seconds. It appears that introducing α_R alone does not remove the high frequency noise that is present in the solution. With α_R = 10, damping overwhelms the physical solution and amplitude dies out completely. This is the typical case when the system is exposed to over-damping. Without the possibility of knowing exact values for Rayleigh damping coefficients, further pursuit of this issue appears to be inappropriate.

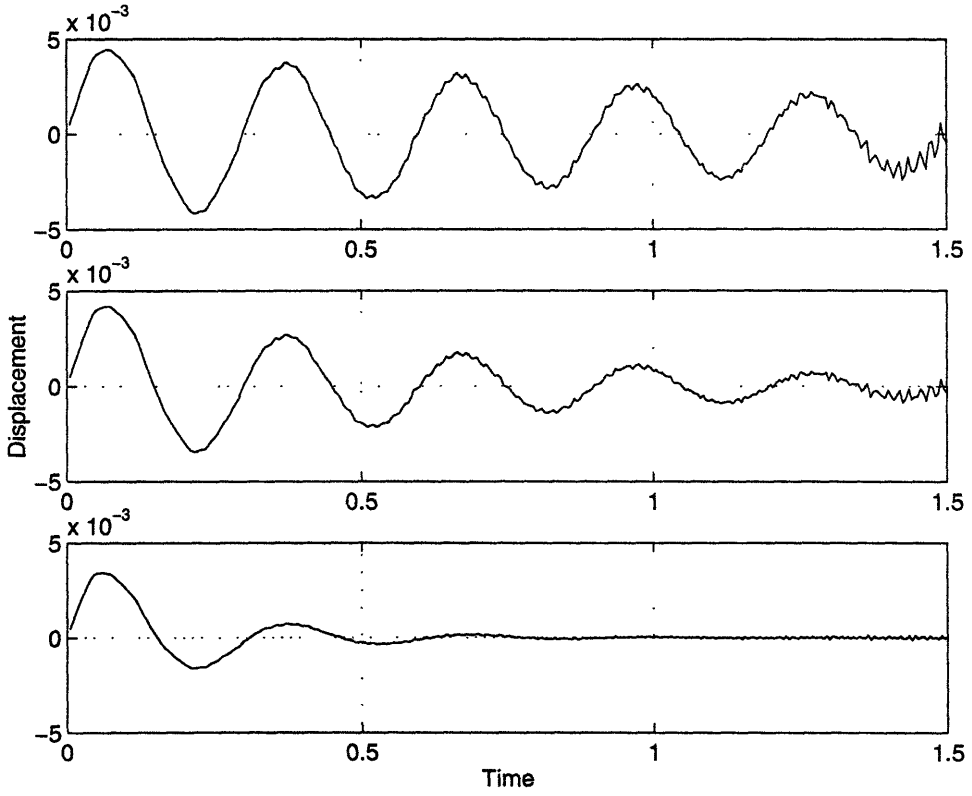

Figure 5.6 The effect of Rayleigh damping coefficient α_R. a) α_R = 0, b) α_R = 2, c) α_R = 10.

5.4 Parametric Study

Knowing that passive fluid situations work, general parametric studies were performed by adding complexities to the fluid-structure interactions one at a time to pinpoint the possible sources of the instability. Specifically, the effects of E, ν, and Δt were closely examined along with the DR limitation that was seen in passive fluid simulations.

5.4.1 Time Scales of the Two Domains

It was surprising to find that a reduction in Δt does not stabilize the system. In unsteady analysis, the consideration of time scales is very important to have a stable and accurate solution. The time scales associated with the fluid domain consist of convective and viscous time scales. These scales can be thought of as the time required for information to travel from one point to another in the fluid domain. For the fluid solver, the Courant (or CFL) condition associated with the convective time scale is satisfied always. For the solid domain, the associated time scales include different modes of vibration, both lateral and longitudinal, and the wave speed that propagates in the solid domain. This is the speed at which small pressure fluctuations propagate in an infinite solid. For slender elements, it is given by :

$$c = \left(\frac{E}{\rho_s} \right)^{\frac{1}{2}} \tag{5.4}$$

In practice, the time scale associated with the solid domain is much smaller than the fluid. For this reason, the implicit method is often employed in practice to avoid strict stability requirements [5]. Since the implicit Newmark method is used, there should be no critical time restriction associated with stability in the solid domain. Since the onset time of the

instability is independent of Δt and dependent on the number of time steps, the problem appears to be due to coupling at the interface, not the stability of the solid or fluid domains by themselves.

5.4.2 Density Ratio Limitation

The first case examined was the 2-D collapsible channel used in the steady fluid-structure simulations. The working fluid was air and wall motion was specified to be similar to that in the passive fluid simulations. In this case, a DR of about 500 was required to run stably. Again in this situation, the reduction of time step alone did not stabilize the system. The instability was more consistent with the number of iterations taken between the two domains.

Next, the Couette flow was simulated since with zero pressure gradient, this is probably is the simplest "active" fluid situation possible . Then we turned to the exact condition of the Luo and Pedley simulations [55] with parabolic velocity inflow such that both shear and pressure forces exist. It was discovered here that if water is used as a working fluid, the restriction on DR was even greater. A value of about DR = 1000 was needed to run stably. The change in critical DR indicates that it must be function of Re.

In reality, the densities of most rubbers are about same as the density of water. Most of the solid metals have densities about factor of ten greater than of water. This means that we cannot simulate any realistic density simulations using water as the fluid.

5.5 Air-Rubber Configuration

The next logical step to take is to compare with the experimental results that are currently available from our laboratory. Several sets of experiments have been performed with rubber and used air as a working fluid [1, 62]. The first check is to run cases that are stable equilibrium points in the parameter space. This means that the steady solver can be used to identify the stable solution and the unsteady runs should settle down to the new equilibrium configuration. For these simulations, runs were performed in the configuration that is used in steady flow limitation analysis. Table 5.3 shows the parameter values in these simulations for an air-rubber system. Note that solid properties imitate rubber-like material closely without being perfectly incompressible (i.e. $v = 0.45$). Figure 5.7 shows a typical simulation at $Re = 400$ with $P_e = -1.0$ Pa. Due to the high Young's modulus, the frequency is very high and rapidly approaches the steady equilibrium condition. The fluid velocity clearly shows that as new equilibrium is reached, the velocity settles to zero. Figure 5.8 shows the actual wall deflection comparing steady and unsteady simulations. Since both cases settle to the same equilibrium configuration, the wall deflection lies on top of each other. This is why it appears as a single curve. Figure 5.9 shows the actual time evolution of the same case illustrating that the wall deflection remains essentially symmetric throughout the stabilizing process.

Table 5.4 shows other representative cases, all with excellent agreement between the steady solver and steady solution obtained from the unsteady solver. In all cases, it is clear that unsteady simulations can effectively identify the stable equilibrium points as expected. The key question to ask at this point is at what velocity flutter is expected.

Time Step	0.001 sec
Solid Density	1000 kg/m^3
Young's Modulus	2 x 10^7 Pa
Poisson's Ratio	0.45
Fluid Density	1.2 kg/m^3
Fluid Viscosity	1.8 x 10^{-5} kg/m*sec

Table 5.3 The parameter values used in the air-rubber configuration.

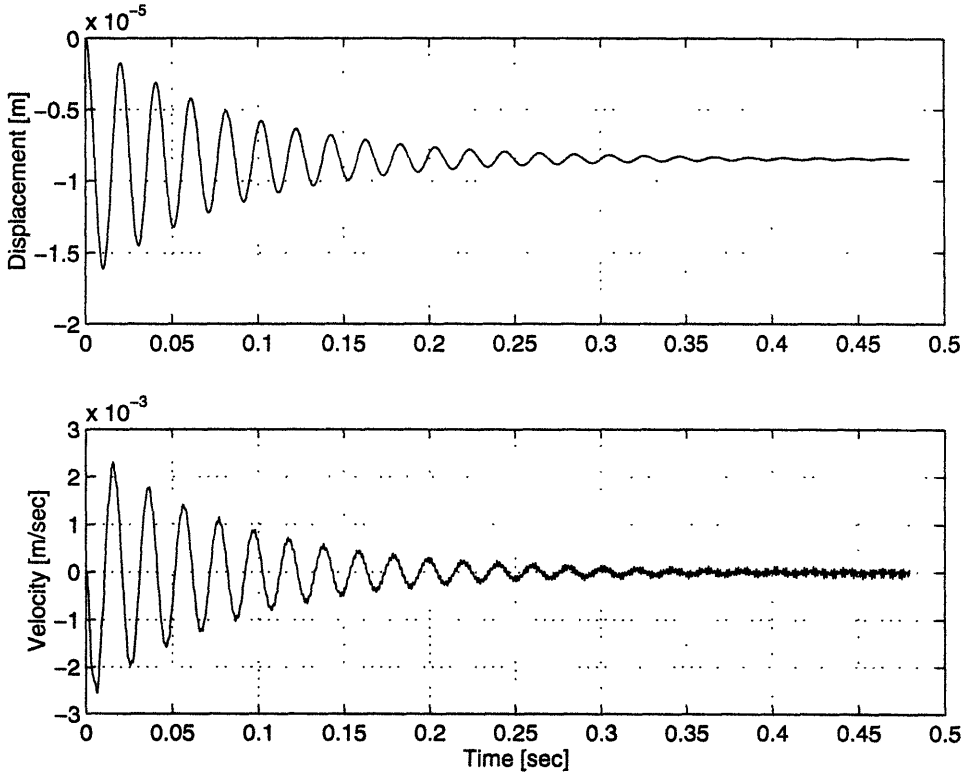

Figure 5.7 The behavior of the air-rubber configuration at Re = 400, P_e = -1.0 Pa. a) The vertical deflection of the solid at the centerline interface, b) The vertical component of fluid velocity at the centerline interface.

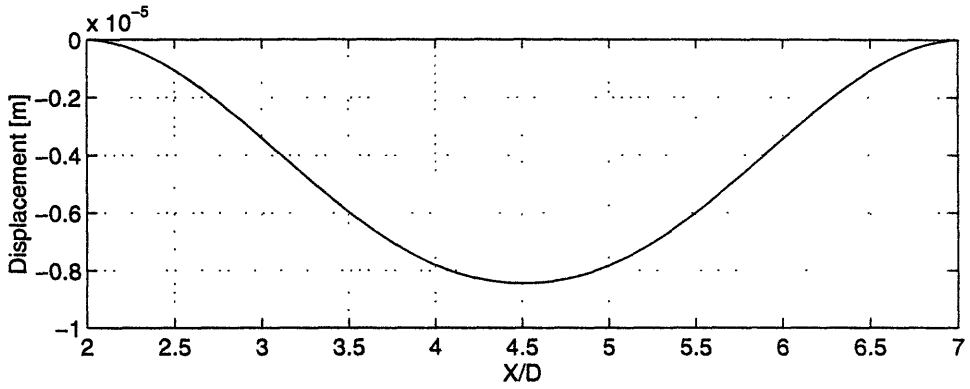

Figure 5.8 The converged wall deflection shape for both steady and unsteady simulations.

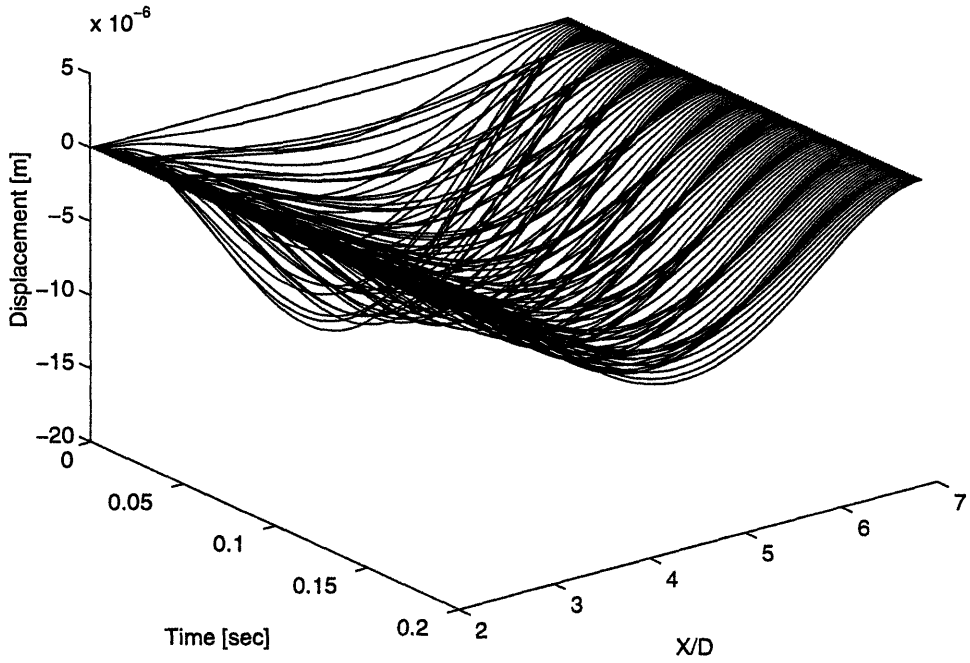

Figure 5.9 The time evolution of the wall deflection for the air-rubber configuration.

Re	P_e (Pa)	Disp (x 10^4 m)	Steady (x 10^4 m)
200	-9.3	-0.88843	-0.89093
400	-9.3	-0.87930	-0.87540
400	-1.0	-0.08433	-0.08456
200	-0.0	0.00596	0.00594
400	-0.0	0.01194	0.01187

Table 5.4 The comparison of midpoint wall deflection between unsteady simulations and the corresponding results from the steady solver.

5.5.1 Prediction of Flutter Speed

Grotberg and Reiss [34] predicted the critical velocity of flutter and it is useful tool to identify the Re range that we would expect to see flutter for the channel just analyzed. We can first simplify their analysis by recognizing that in our simulations, there is no solid damping (if Rayleigh damping is ignored) and their externally-imposed elastance is zero since we have no elastic springs that support the solid. In this situation, their equations 3.4b or 3.6 reduce to

$$u_{crit} = \frac{\pi h}{\lambda}\left[\frac{E}{3(1-\nu^2)\rho_s}\right]^{1/2} \tag{5.7}$$

Note that fluid density does not appear. For the air flowing through our rubber collapsible channel, u_{crit} = 5.745 m/s which corresponds to $(Re)_{crit}$ of about 3830. Note that this lies in the turbulent regime beyond the flow simulation capabilities.

This can also be examined from the perspective of the dispersion analysis of Chapter 4, but now including the effects of wall mass. In section 4.2, the wave speed limitation was predicted based on steady plate equation as shown in equation 4.1. This is appropriate only in the limit that the mass of the wall is negligible compared to the fluid mass. Including wall mass, the plate equation contains an additional acceleration term such that

$$P - P_e \cong M\frac{\partial^2 y}{\partial t^2} - T\frac{\partial^2 y}{\partial x^2} + EI\frac{\partial^4 y}{\partial x^4} \tag{5.8}$$

where M is the mass of the solid per unit width. We performed the same procedure as in section 4.2 and the reader is encouraged to review the procedure explained in that section. The result, equivalent to equation 4.11, is given by:

$$\begin{aligned} c^2 &= \frac{\frac{4Eh^3 y_o \pi^4}{3(1-\nu^2)\rho\lambda^4}\overline{\eta} + \frac{4\pi^2 T y_o}{\rho\lambda^2}\overline{\eta}}{1 + \frac{4\pi^2 \rho_s h y_0}{\rho_f \lambda^2}\overline{\eta}} \\ &= \frac{c_B^2 + c_T^2}{1 + \frac{4\pi^2 \rho_s h y_0}{\rho_f \lambda^2}\overline{\eta}} \end{aligned} \tag{5.9}$$

we now have a two component denominator which contains a term representing the effect of wall acceleration in the plate equation. Note that this equation reduces to equation 4.11 as $\rho_s/\rho_f \to 0$. For the 2-D collapsible channel of Figure 4.2, note that the key term is the density ratio of the two domains. If the densities are same, the magnitude of the second term is one order of magnitude smaller than one. The effect of the acceleration term is minimal and the analysis of section 4.2 pertains, and relationship given by equation 4.11

holds. If the solid density is much greater than the fluid, however, the second term cannot be neglected. For example, if DR = 1000 (approximately the case for the air-rubber system), then the second term in the denominator of equation 5.9 dominates and the wave speed is given by:

$$c^2 = \frac{Eh^2\pi^2}{3(1-\nu^2)\lambda^2\rho_s} + \frac{T}{\rho_s h} \tag{5.10}$$

Note that the critical velocity predicted by equation 5.5. is identical to the above expression if only the bending term is considered. Since Grotberg and Reiss did not include the initial tension effects in their analysis, and therefore these equations are, in fact, identical, indicating that the critical velocity for flutter is again simply the wave propagation speed. The ratio γ given by equation 4.12 does not change and therefore we can clearly identify the two extremes as before.

In summary, the theoretical prediction by Grotberg and Reiss [34] and dispersion analysis have shown that flutter can be seen only for the regime with Re > 3000 for a rubber channel (of the dimensions given here) conveying air. The experiments in our laboratory [1, 62] are consistent with this result. Consequently, some form of turbulent model (such as k-ε model) would be necessary to simulate the experimentally observed flutter. One alternative is to vary the solid parameters to examine "hypothetical" materials such that would ensure that the critical velocity for flutter lies in the Re region that can be effectively handled by the fluid solver. The simplest way to accomplish this is to lower the Young's modulus and thereby lowering the wave speed in the solid. Figure 5.10 shows the effect of varying Young's modulus beginning with the modulus of the air-rubber system. For Case B, Re < $(Re)_{crit}$, but for Case C, Re > $(Re)_{crit}$ = 383. In Cases A and B, it is clear that the initial perturbation is subsiding suggesting the absence of flutter. This

situation is not as clear in Case C. Another point to note is that run terminated abruptly for Case C (at later time for case B). This behavior is puzzling since no inherent instability was seen up to the last few steps where large fluctuation and rapid growth of fluid pressure cause the code to crash.

Examining equation 5.7, it can be seen that another way to lower $(Re)_{crit}$ is to increase the density of the solid. In these cases, similar results were encountered. Also, the combinations of varying both Young's modulus and solid density are tried. Again the same results are witnessed. In summary, analysis has shown that either: flutter is not witnessed or numerical instability was encountered when "hypothetical" materials are examined. Further study is needed to provide a definite result.

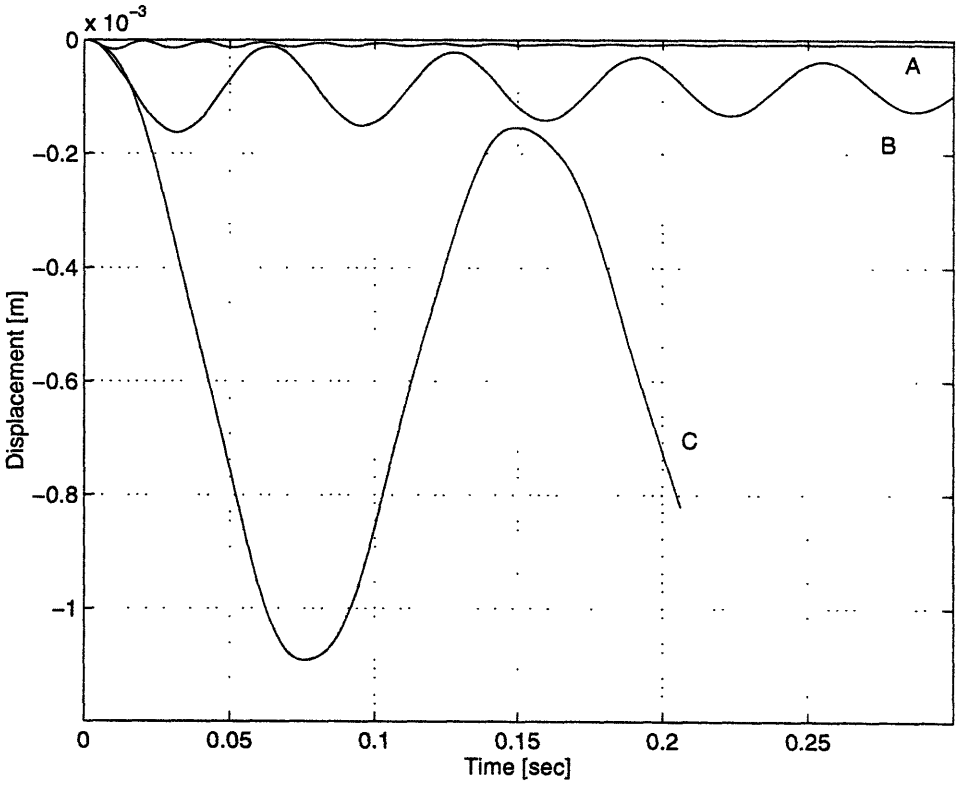

Figure 5.10 The effect of varying Young's modulus at Re = 400 and P_e = -1.0 Pa. A) E = 2 x 10^7 Pa [$(Re)_{crit}$ = 3830], B) E = 2 x 10^6 Pa [$(Re)_{crit}$ = 1211], C) E = 2 x 10^5 Pa [$(Re)_{crit}$ = 383].

In an attempt to delay or eliminate the numerical instability, the tolerance requirement of the inner loop in SLDCONV (see section 3.2.2) was varied. In most of simulations, note that a tolerance of 0.001 was adequate for steady simulations. This value was lowered to have a better compatibility between two domains, but lowering to 0.0001 cannot overcome the strong instability associated with these simulations. Maximum counter is reached (otherwise infinite inner looping would occur) and the time is marched even without fully converged between two domains. Up to the point of instability, the obvious difference in any of the parameter values were not witnessed. For other cases that are doomed to crash from the beginning, the tightening the tolerance often resulted in earlier crash and cannot overcome the inherent instabilities.

5.6 Assessment

The current status suggests that the segregated approach used in this study is unstable in most simulations in which the wall motion is strongly influenced by the fluid. In no situation was it possible to simulate the onset of flutter. The results have shown that the new model offers a limited parameter space that can be used for unsteady simulations. Specifically, the density ratio must be large to ensure that stable runs are possible. This limitation leaves the question of whether the segregated approach that we adopted is adequate to solve all types of unsteady fluid-structure interactions. In contrast, the steady solver seems quite robust, at least in the range of conditions for which a steady solution is anticipated.

In the previous chapter, we performed steady simulations and concluded with the remark that unsteady simulations were required to identify whether the breakdown of

steady solutions are numerical or physical. This in fact was the prime reason for the creation of the unsteady solver. As a first check, we ran the last stable solution using a unsteady code while reading in the latest geometry and stresses as initial conditions. This is equivalent to performing "self-consistency" test because no change in geometry (i.e. no displacements) should occur since we are already at an equilibrium. For tension-dominant case, no change in displacements was seen for first three seconds of simulation. Then, oscillation in displacements develops and start to deviate from the equilibrium in a static divergence fashion. Starting about at the same time, deviation from the equilibrium values are seen in fluid pressure and velocity components. It appears that once the numerical instability is triggered, no mechanism exists to stabilize the system and inevitable growth of numerical instability take place as we switch between two domains. This behavior was also true for other steady equilibrium points. The unsteady solver is then used to check the conditions that encountered numerical breakdown. In all cases, only the static divergence type of instability was witnessed. Since "self-consistency" is never established, these results are inconclusive.

The theoretical analysis of the coupled system may give us some insight into the inherent problems associated with the segregated approach, but this is beyond the scope of this thesis. This is why our approach was totally based on numerical experimentation. Alternatively, the coupled coefficient matrix can be used and may result in a stable solution (see section 2.4). This step requires a major coding effort, however, and may or may not remove the limitations encountered with the segregated approach.

Chapter 6

Conclusions

In this thesis, a new computational approach for the simulation of flows through compliant channels has been developed. Specifically, this model, for the first time, utilizes a spectral element method for both fluid and solid domains. Using a segregated approach, the scheme iterates between the fluid and solid solvers to simulate both steady and unsteady two-dimensional channel flows.

After going through verification stages for the solid alone and then for the steady fluid-structure analysis, the results have shown that the present approach can effectively handle these situations and compares well with a variety of published results. The code was then used to examine flow limitation in a collapsible channel. The results indicate that the limiting flow rate can be well predicted using the notion of wave speed flow limitation along with the dispersion relationship of the channel if the wavelength is taken to be the length of the collapsible region.

Further study is required to examine self-excited flow-induced oscillations. The preliminary results obtained here indicate that passive fluid situations can be handled effectively, but that numerical instabilities arise in attempting to simulate flutter, in which the flow excites oscillations in the wall. Nevertheless, the code is capable of simulating certain cases of unsteady channel flow corresponding to parameter values in the range of interest. Unless a turbulent model is introduced, actual comparison with experimental

results for flutter are not possible. This work sets the groundwork and points to new directions for simulations involving fluid-structure interactions.

6.1 Future Considerations

This work can be viewed as first step toward more realistic simulations of flutter since it goes beyond the limitations of other investigators. It produces, for the first time, a consistent spectral element approach that eliminates, at least for 2-D flow, most of the approximations of previous studies. Although realistic coupling can be simulated, our model is still subject to certain limitations. In this section, suggestions are made as to how these limitations might be overcome.

The completed code is general and, in principle, capable of simulating all fluid-structure situations including flutter in which the fluid moves a significant distance with respect to the wall. This thesis emphasized flow through the collapsible channel since it was the main motivation of the project. However, fluid-structure interactions arise in wide variety of engineering situations, and therefore this code can be used for other purposes. Specifically, the new code will provide a foundation for the simulation of many physiological flows due to the passive wall motion capability. Examples might include the movement of a deformable neutrophil through a distensible channel, or the deformation of the arterial endothelium resulting from fluid dynamic stress.

It is always possible to include further complexities so that the situation mimics the reality as much as possible. The extensions are numerous and main components of future considerations are discussed here.

6.1.1 Parameter Studies

There are several effects that can be explored with the current code. The first is the effect of tapered wall on flow limitation and flutter. This effect can be easily studied in the simulation by allowing wall to vary linearly in thickness. Experiments have shown that tapering minimizes the end effects, and it would be interesting how the wall deflection evolve in both steady and unsteady simulations. The second is the effect of variation in initial wall tension. So far, only the constant initial wall tension was explored. Other possibilities include the simulation of thinner channels, although that would require more elements to retain a reasonable aspect ratio. For flow limitation, the critical Reynolds numbers can be lowered simply by increasing fluid viscosity. This would also be a useful avenue to pursue.

6.1.2 Axisymmetric Simulation

Axisymmetric capabilities are already formulated for NEKTON and most of the modifications have already been implemented in the solid solver. The only reason that axisymmetric case was abandoned is the lack of comparable verification cases. Furthermore, the deformation seen in tube flutter are not axisymmetric and therefore it seems more logical sense to pursue three-dimensional extensions. This would mean significant increase in computational cost-even more so for unsteady simulations. The coding is designed, however, so that extension to other dimensions require minimal programming effort.

6.1.3 Material Nonlinearity

Material nonlinearities can enter through the stress-strain relations, and therefore they are separate from geometric nonlinearities. In this thesis, we did not explore the simulations related to variations in stress-strain matrices. We assumed solid elements to be both linear and elastic locally. Nonlinearity was solely due to the large displacement of the wall. Many structures of practical importance are linear for loads below a maximum linear limit and elastic for loads below the onset of yielding. In practice, though, there are many different material laws that are employed in numerical simulations. This possibility can be further explored to simulate a particular material behavior of interest if the material behavior is known and can be modeled effectively. Great flexibility is allowed for many different types of materials.

6.1.4 Incompressible Formulation

In this thesis, many tests were performed with solids that are fixed at both ends of the domain. For this type of boundary condition, large lateral deflection will inevitably lead to large strain in the solid. The current model is based on the assumption of large displacement but small strain. In order to deal with large strain deformation, nonlinear strain must be introduced to the program. In the regime of large strain, the linear elastic constitutive relationship will not be valid. We need specialized hyper-elastic model, such as the Mooney-Rivlin model required for rubber-like materials. In addition to more complicated constitutive laws, these models are based on the incompressibility of the solid. This means that we need a special formulation for the constraint parameter, which is pressure in the fluid solver. This requires a whole new approach to the problem at hand, and therefore this formulation was not pursued. It would be interesting to compare our

formulation against the incompressible formulation if it were available. The comparison would show the how much error is incurred by ignoring the large strain assumption.

Appendices

Appendix A: Surface Traction Forces

The surface forces that act on a solid are due to the viscous stresses and pressure forces at the interface. This is how the fluid and solid domains are coupled. Traction forces are given by:

$$f_i^s = \tau_{ij} n_j \tag{A.1}$$

where stresses are represented in tensor form as

$$\tau_{ij} = \begin{bmatrix} \tau_{xx} - P & \tau_{xy} & \tau_{xz} \\ \tau_{yx} & \tau_{yy} - P & \tau_{yz} \\ \tau_{zx} & \tau_{zy} & \tau_{zz} - P \end{bmatrix} \tag{A.2}$$

Thus, both pressure and viscous stresses are accounted for. Note that the body forces are ignored in Eq. (A.1). For a Newtonian fluid, the viscous stresses are proportional to the element strain rates and the coefficient of viscosity. This means that viscous stresses take the following simple forms

$$
\begin{aligned}
\tau_{xx} &= 2\mu\frac{\partial u}{\partial x} \\
\tau_{yy} &= 2\mu\frac{\partial v}{\partial y} \\
\tau_{zz} &= 2\mu\frac{\partial w}{\partial z} \\
\tau_{xy} = \tau_{yx} &= \mu\left(\frac{\partial u}{\partial y} + \frac{\partial v}{\partial x}\right) \\
\tau_{xz} = \tau_{zx} &= \mu\left(\frac{\partial w}{\partial x} + \frac{\partial u}{\partial z}\right) \\
\tau_{xy} = \tau_{yx} &= \mu\left(\frac{\partial v}{\partial z} + \frac{\partial w}{\partial y}\right)
\end{aligned}
\tag{A.3}
$$

This means that if velocity components u, v, w, and pressure P are known, we can easily calculate the components of traction forces that act on the solid surface.

Numerically, the calculation of surface traction forces is simple once the stresses and pressures are known. Care must be given to the fact that the pressures are calculated at the collocation points that are two orders smaller than the velocity field (i.e. N-2 instead of N to eliminate the spurious modes). Therefore, proper mapping must be performed to ensure summation with the stresses. Once these forces are known, they are introduced to the solid solver as external forces.

Appendix B: Stress-Strain Matrices

In 2-D analysis, two types of material modeling are used (see section 2.5). The differences lie in the assumptions made in the simulation and in the material matrix C given here. For plane stress,

$$C = \frac{E}{1-\nu^2}\begin{bmatrix} 1 & \nu & 0 \\ \nu & 1 & 0 \\ 0 & 0 & \frac{1-\nu}{2} \end{bmatrix} \tag{B.1}$$

The plane strain C is given by:

$$C = \frac{E(1-\nu)}{(1+\nu)(1-2\nu)}\begin{bmatrix} 1 & \frac{\nu}{1-\nu} & 0 \\ \frac{\nu}{1-\nu} & 1 & 0 \\ 0 & 0 & \frac{1-2\nu}{2(1-\nu)} \end{bmatrix} \tag{B.2}$$

where E is Young's modulus (modulus of elasticity) and represents the rate of change of normal stress for a unit normal strain in a given material, and ν is Poisson's ratio and is the ratio of lateral shrinkage (expansion) to longitudinal expansion (shrinkage) of a bar of a given material which has been placed under a uniform longitudinal tensile (compressive) load. A good estimate for most engineering materials is ν = 0.3. Poisson's ratio only occasionally varies more than 20% from this value. The maximum theoretical value for an isotropic material is ν = 0.5. The minimum theoretical value is ν = -1; however, in reality, materials with negative ν are unknown [13].

Appendix C: Coordinate Transformation

In a local coordinate system, we know that the longitudinal initial tension contribution is always axial. Since large displacement is involved, we need to ensure the transfer of stresses in the global coordinate system. In 2-D, this implies a rotation about z-axis as shown in Figure C.1.

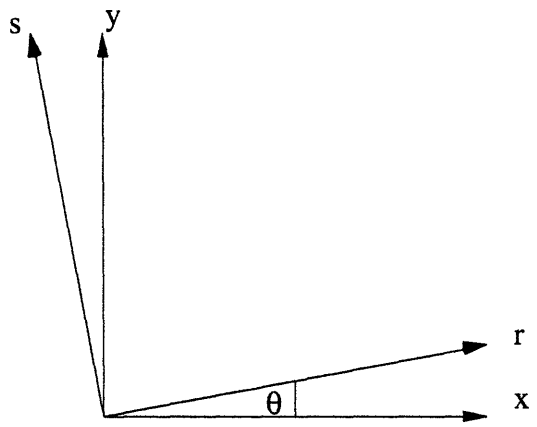

Figure C.1 The coordinate transform between different coordinate systems with respect to a common Z-axis.

Let (r, s) represent a local coordinate system and (x, y) the global. From Popov [65] the stress components are related by

$$\begin{aligned} \sigma_r &= \frac{\sigma_x + \sigma_y}{2} + \frac{\sigma_x - \sigma_y}{2}\cos 2\theta + \tau_{xy}\sin 2\theta \\ \tau_{rs} &= -\frac{\sigma_x - \sigma_y}{2}\sin 2\theta + \tau_{xy}\cos 2\theta \end{aligned} \qquad \text{(C.1)}$$

Furthermore, we know that the sum of the normal stresses on any two mutually perpendicular planes is invariant. Mathematically, this means:

$$\sigma_x + \sigma_y = \sigma_r + \sigma_s = K \tag{C.2}$$

Since we only have σ_r, the above analysis collapses to the following simple relationships in the global coordinates:

$$\begin{aligned} \sigma_x &= \sigma_r \cos^2\theta \\ \sigma_y &= \sigma_r \sin^2\theta \\ \tau_{xy} &= \sigma_r \sin\theta\cos\theta \end{aligned} \tag{C.3}$$

This means that at any equilibrium configuration, we can easily determine the stresses by knowing the angle between two coordinate systems. In NEKTON, the angle (θ) was calculated from the local geometric derivatives. This means:

$$\theta = \tan^{-1}\left(\frac{\partial y / \partial r}{\partial x / \partial r}\right) \tag{C.4}$$

Note that the same conclusion can be arrived with the tensor rotation. In this case,

$$\tau_{(x,y)} = P^T \tau_{(r,s)} P \quad ; \quad P = \begin{bmatrix} \cos\theta & \sin\theta \\ -\sin\theta & \cos\theta \end{bmatrix} \tag{C.5}$$

where P is the rotation matrix used to represent rotation about the z-axis.

References

[1] Agrawal, H., 1991, Flow Limitation and Flutter in a Collapsible Tube. A.B. thesis, Harvard College.

[2] Anderson, D.A., Tannehill, J.C., and Pletcher, R.H., 1984, *Computational Fluid Mechanics and Heat Transfer,* New York, Hemisphere Publishing Corporation.

[3] Bathe, K.J., Ramm, E., and Wilson, E.L., 1975, Finite Element Formulations for Large Deformation Dynamic Analysis. *International Journal for Numerical Methods in Engineering*, 9, 353-386.

[4] Bathe, K.J., and Hahn, W., 1979, On Transient Analysis of Fluid-Structure Systems. *Computers & Structures,* 10:383-391.

[5] Bathe, K.J., 1982, *Finite Element Procedures in Engineering Analysis,* Englewood Cliffs, NJ, Prentice-Hall, Inc.

[6] Belytschko, T.B., 1980, Fluid-Structure Interaction. *Computers & Structures,* 12:459-469.

[7] Benjamin, T.B., 1963, The Threefold Classification for Unstable Disturbances in Flexible Surfaces Bounding Invicid Flow. *Journal of Fluid Mechanics,* 16:436-450.

[8] Bertram, C.D., 1982, Two Modes of Instability in a Thick-Walled Collapsible Tube Conveying Flow. *Journal of Biomechanics,* 15:223-224.

[9] Bertram, C.D., and Pedley, T.J., 1982, A Mathematical Model of Unsteady Collapsible Tube Behavior. *Journal of Biomechanics,* 15:39-50.

[10] Bertram, C.D., 1986, Unstable Equilibrium Behavior in Collapsible Tubes. *Journal of Biomechanics*, 19, 61-69.

[11] Bertram, C.D., Raymond, C.J., and Pedley, T.J., 1990, Mapping of Instabilities for Flow Through Collapsed Tubes of Different Length. *Journal of Fluids and Structures,* 4, 125-154.

[12] Bertram, C.D., Raymond, C.J., and Pedley, T.J., 1991, Application of Nonlinear Dynamics Concepts to the Analysis of Self-Excited Oscillations of a Collapsible Tube Conveying a Fluid. *Journal of Fluids and Structures,* 5, 391-426.

[13] Blevins, R.D., 1979, *Formulas for Natural Frequency and Mode Shape*, New York, Van Nostrand Reinhold Co.

[14] Bonis, M., and Ribreau, C., 1978, Etude de Quelques Proprietés de L'écoulement Dans Une Conduite Collabable. *La Houille Blanche*, 3/4, 165-173.

[15] Cancelli, C., and Pedley, T.J., 1985, A Separated-Flow Model for Collapsible Tube Oscillations. *Journal of Fluid Mechanics,* 157, 375-404.

[16] Canuto, C., Hussaini, M.Y., Quarteroni, A., and Zang T.A., 1988, *Spectral Methods in Fluid Dynamics,* Berlin, Springer-Verlag.

[17] Carey, G.F., and Oden, J.T., 1986, *Finite Elements: Fluid Mechanics,* Vol. VI, Englewood Cliffs, NJ, Prentice-Hall Inc.

[18] Carpenter, P.W., and Garrad, A.D., 1985, The Hydrodynamic Stability of Flow Over Kramer-Type Compliant Surfaces. Part 1. Tollmien-Schlichting Instabilities. *Journal of Fluid Mechanics,* 155:465-510.

[19] Carpenter, P.W., and Garrad, A.D., 1986, The Hydrodynamic Stability of Flow Over Kramer-Type Compliant Surfaces. Part 2. Flow Induced Surface Instabilities. *Journal of Fluid Mechanics,* 170:199-232.

[20] Chen, T.S., and Sparrow, E.M., 1967, Stability of the Developing laminar Flow in a Parallel Plate Channel. *Journal of Fluid Mechanics,* 30:209-224.

[21] Conrad, W.A., 1969, Pressure-Flow Relationships in Collapsible Tubes. *IEEE Transactions in Biomedical Engineering,* BME-16, 284-295.

[22] Dawson, S.V., and Elliott, E.A., 1977, Wave-Speed Limitation on Expiratory Flow: A Unifying Concept. *Journal of Applied Physiology,* 43, 498-515.

[23] Elad, D., Kamm, R.D., and Shapiro, A.H., 1988, Mathematical Simulation of Forced Expiration. *Journal of Applied Physiology,* 65:14-25.

[24] Elad, D., and Kamm, R.D., 1989, Parametric Evaluation of Forced Expiration Using a Numerical Method. *ASME Journal of Biomechanical Engineering,* 111, 192-199.

[25] Elliott, E.A., and Dawson, S.V., 1977, Test of Wave Speed Theory of Flow Limitation in Elastic Tubes. *Journal of Applied Physiology,* 43:516-522.

[26] Fletcher, C.A., 1988, *Computational Techniques for Fluid Dynamics,* Vol. I, Berlin, Springer-Verlag.

[27] Fletcher, C.A., 1988, *Computational Techniques for Fluid Dynamics,* Vol. II, Berlin, Springer-Verlag.

[28] Fry, D.L., and Hyatt, R.E., 1960, Pulmonary Mechanics. A Unified Analysis of the Relationship Between Pressure, Volume and Gas Flow in the Lungs of Normal and Diseased Human Subjects. *American Journal of Medicine,* 29:672-689.

[29] Gavriely, N., and Grotberg, J.B., 1988, Flow Limitation and Wheezes in a Constant Flow and Volume Lung Preparation. *Journal of Applied Physiology,* 64:17-20.

[30] Gavriely, N., Shee, T.R., Cugell, D.W., and Grotberg, J.B., 1989, Flutter in Flow-Limited Collapsible Tubes: A Mechanism for Generation of Wheezes. *Journal of Applied Physiology,* 66(5), 2251-2261.

[31] Golub, G.H., and Van Loan, C.F., 1983, *Matrix Computations*, Baltimore, John Hopkins University Press.

[32] Grotberg, J.B., and Davis, S.H., 1980, Fluid-Dynamic Flapping of a Collapsible Channel: Sound Generation and Flow Limitation. *Journal of Biomechanics,* 13, 219-230.

[33] Grotberg, J.B., and Reiss E.L., 1982, A Subsonic Flutter Anomaly. *Journal of Sound and Vibration,* 80:444-446.

[34] Grotberg, J.B., and Reiss E.L., 1984, Subsonic Flapping Flutter. *Journal of Sound and Vibration*, 92(3), 349-361.

[35] Grotberg, J.B., and Shee T.R., 1985, Compressible-Flow Channel Flutter. *Journal of Fluid Mechanics,* 159, 175-193.

[36] Grotberg, J.B., and Gavriely, N., 1989, Flutter in Collapsible Tubes: A Theoretical Model of Wheezes. *Journal of Applied Physiology*, 66:2262-2273.

[37] Grotberg, J.B., 1994, Pulmonary Flow and Transport Phenomena. *Annual Review of Fluid Mechanics*, 26, 529-571.

[38] Heil, M., and Pedley, T.J., 1995, Large Axisymmetric Deformation of a Cylindrical Shell Conveying a Viscous Flow. *Journal of Fluids and Structures*, 9, 237-256.

[39] Heil, M., 1996, The Stability of Cylindrical Shells Conveying Viscous Flow. *Journal of Fluids and Structures*, 10, 173-196.

[40] Ho, L.W., 1989, A Legendre Spectral Element Method for Simulation of Incompressible Unsteady Viscous Free-Surface Flows. Ph.D. thesis, M.I.T.

[41] Ho, L.W., 1995, *private communications.*

[42] Holden, J.T., 1972, On the Finite Deflections of Thin Beams. *International Journal of Solids and Structures*, 8:1051-1055.

[43] Jaeckle, D., 1987, Critical Transitions Associated with Steady Flow in Collapsible Tubes with Varying Wall Stiffness. S.M. thesis, M.I.T.

[44] Jensen, O.E., and Pedley, T.J., 1989, The Existence of Steady Flow in a Collapsed Tube. *Journal of Fluid mechanics,* 206, 339-374.

[45] Jensen, O.E., 1990, Instabilities of Flow in a Collapsed Tube. *Journal of Fluid Mechanics,* 220, 623-659.

[46] Jensen, O.E., 1992, Chaotic Oscillations in a Simple Collapsible-Tube Model. *Journal of Biomechanical Engineering,* 114:55-59.

[47] Katz, A.I., Chen, Y., and Moreno, A.H., 1969, Flow Through a Collapsible Tube. *Biophysical Journal*, 9, 1261-1279.

[48] Kamm, R.D., and Shapiro, A.H., 1979, Unsteady Flow in a collapsible Tubes Subjected to External Pressure or Body Forces. *Journal of Fluid Mechanics,* 95, 1-78.

[49] Kamm, R.D., and Pedley, T.J., 1989, Flow in Collapsible Tubes: A Brief Review. *ASME Journal of Biomechanical Engineering,* 111, 177-179.

[50] Kececioglu, I., McClurken, M.E., Kamm, R.D., and Shapiro, A.H., 1981, Steady, Supercritical Flow in Collapsible Tubes. Part 1. Experimental Observations. *Journal of Fluid Mechanics,* 109, 367-389.

[51] Landahl, M.T., 1962, On the Stability of a Laminar Incompressible Boundary Layer Over a Flexible Surface. *Journal of Fluid Mechanics,* 13:607-632.

[52] Love, A.E.H., 1944, *A Treatise on the Mathematical Theory of Elasticity*, New York, Dover Publications.

[53] Lowe, T.W., and Pedley, T.J., 1995, Computation of Stokes Flow in a Channel with a Collapsible Segment. *Journal of Fluids and Structures,* 9, 885-905.

[54] Lucey, A.D., and Carpenter, P.W., 1992, A Numerical Simulation of the Interaction of a Compliant Wall and Invicid Flow. *Journal of Fluid Mechanics,* 234:147-170.

[55] Luo, X.Y., and Pedley, T.J., 1995, A Numerical Simulation of Steady Flow in a 2-D Collapsible Channel. *Journal of Fluids and Structures,* 9, 149-174.

[56] Luo, X.Y., and Pedley, T.J., 1996, A Numerical Simulation of Unsteady Flow in a two-dimensional Collapsible Channel. *Journal of Fluid Mechanics,* 314, 191-225.

[57] Matsuzaki, Y., and Fung, Y.C., 1979, Non-Linear Stability Analysis of a Two-Dimensional Model of an Elastic Tube Conveying a Compressible Flow. *ASME Journal of Applied Mechanics,* 46:31-36.

[58] Matsuzaki, Y., and Matsumoto, T., 1989, Flow in a Two-Dimensional Collapsible Channel with Rigid Inlet and Outlet. *Journal of Biomechanical Engineering,* 111:180-184.

[59] McClurken, M.E., Kececioglu, I, Kamm, R.D., and Shapiro, A.H., 1981, Steady, Supercritical Flow in Collapsible Tubes. Part 2. Theoretical Studies. *Journal of Fluid Mechanics,* 109, 391-415.

[60] Oates, G.C., 1975, Fluid Flow in Soft Walled Tubes. Part 1: Steady Flow. *Medical Biology Engineering,* 13, 773-778.

[61] Olson, L.G., and Bathe, K.J., 1985, Analysis of Fluid-Structure Interactions. A Direct Symmetric Coupled Formulation Based on the Fluid Velocity Potential. *Computers & Structures,* 21:1/2:21-32.

[62] Patel, N.R., 1993, A Study of Flow Limitation and Flow-Induced Oscillations During Airflow Through Collapsible Tubing. B.S. thesis, M.I.T.

[63] Pedley, T.J., 1980, *The Fluid Mechanics of Large Blood Vessels,* Cambridge, Cambridge University Press.

[64] Pedley, T.J., 1992, Longitudinal Tension Variation in Collapsible Channels: A New Mechanism for the Breakdown of Steady Flow. *ASME Journal of Biomechanical Engineering,* 114, 60-67.

[65] Popov, E.P., 1978, *Mechanics of Materials,* 2nd ed., Englewood Cliffs, NJ, Prentice-Hall, Inc.

[66] Rao, S.S., 1990, *Mechanical Vibrations,* 2nd ed., Reading, MA, Addison-Wesley Publishing Company.

[67] Rast, M.P., 1994, Simultaneous Solution of the Navier-Stokes and Elastic Membrane Equations by a Finite Element Method. *International Journal for Numerical Methods in Fluids,* 19, 1115-1135.

[68] Reddy, J.N., 1993, *An Introduction to the Finite Element Method,* 2nd ed., New York, McGraw-Hill, Inc.

[69] Ronquist, E.M., 1988, Optimal Spectral Element Methods for the Unsteady Three-dimensional Incompressible Navier-Stokes Equations. Ph.D. thesis, M.I.T.

[70] Shapiro, A.H., 1977, Steady Flow in Collapsible Tubes. *ASME Journal of Biomechanical Engineering,* 99, 126-147.

[71] Shin, J.J., 1992, Numerical Modeling of Forced Expiratory Flow in a Human Lung. S.M. thesis, M.I.T.

[72] Shin, J.J., Elad, D., and Kamm, R.D., 1995, *Simulation of Forced Breathing Maneuvers,* Biological Flows, chapter 15, New York, Plenum Press.

[73] Walsh C., 1995, Flutter in One-Dimensional Collapsible Tubes. *Journal of Fluids and Structures,* 9, 393-408.

[74] Weaver, D.S., and Paidoussis, M.P., 1977, On Collapse and Flutter Phenomena in Thin Tubes Conveying Fluid. *Journal of Sound and Vibration,* 50:117-132.

[75] Webster, P.M., Sawatzky, R.P., Hoffstein, V., Leblanc, R., Hinchey, M.J., and Sullivan, P.A., 1985, Wall Motion in Expiratory Flow Limitation: Choke and Flutter. *Journal of Applied Physiology,* 59:1304-1312.

[76] Zienkiewicz, O.C., and Bettess, P., 1978, Fluid-Structure Dynamic Interaction and Wave Forces. An Introduction to Numerical Treatment. *International Journal for Numerical Methods in Engineering,* 13:1-16.

[77] Zienkiewicz, O.C., and Taylor, R.L., 1989, *The Finite Element Method,* Vol. 1, London, McGraw-Hill Inc.

[78] Zienkiewicz, O.C., and Taylor, R.L., 1991, *The Finite Element Method,* Vol. 2, London, McGraw-Hill Inc.